A Measurement of the Cosmic Microwave Background Radiation (CMBR) Anisotropy at the Half Degree Angular Scale

by

Casey Ann Inman

B.A. Physics and Chemistry
University of California, Berkeley, 1989

Submitted to the Department of Physics
in partial fulfillment of the requirements for the degree of

Doctor of Philosophy

at the

MASSACHUSETTS INSTITUTE OF TECHNOLOGY

June 1996

Author . . . . . .
Department of Physics
17 April 1996

Certified by . . . . . .
Stephan S. Meyer
Associate Professor, University of Chicago
Thesis Supervisor

Accepted by . . . . . .
George F. Koster
Chairman, Departmental Committee on Graduate Students

A Measurement of the Cosmic Microwave Background Radiation (CMBR) Anisotropy at the Half Degree Angular Scale

by

Casey Ann Inman

Submitted to the Department of Physics
on 17 April 1996, in partial fulfillment of the
requirements for the degree of
Doctor of Philosophy

Abstract

The study of anisotropies in the cosmic microwave background radiation (CMBR) promises to be the best tool available to study the origin of our Universe. The Medium Scale Anisotropy Measurement (MSAM1) is balloon-borne telescope designed to measure anisotropies near the first Doppler peak in the CMBR power spectrum. The instrument chops a $28'$ beam in a 3 position pattern with a throw of $\pm 40'$, simultaneously measuring single and double differenced sky signals. These data in four spectral channels centered at 5.7, 9.3, 16.5, and 22.6 cm^{-1} are fit to a two component spectral model consisting of CMBR anisotropy and thermal emission from interstellar dust. The first flight of the MSAM1 instrument, made in June of 1992 (MSAM1-92), yielded detections of CMBR anisotropy. The second flight in June of 1994 (MSAM1-94) observed the same field as the first flight to confirm the earlier measurements. The MSAM1-94 flight yields both a double difference detection of CMBR fluctuations of $1.1 \times 10^{-5} \leq \Delta T/T \leq 3.1 \times 10^{-5}$ (90% confidence interval, including calibration uncertainty) for total rms Gaussian fluctuations with correlation angle $0.^{\circ}3$; and a single difference detection of $1.0 \times 10^{-5} \leq \Delta T/T \leq 3.2 \times 10^{-5}$ (90% confidence interval, including calibration uncertainty) for total rms Gaussian fluctuations with correlation angle $0.^{\circ}5$. In order to compare the CMBR and interstellar dust emission data at each celestial point measured, sum and difference of the MSAM1-92 and MSAM1-94 datasets are created. Resulting difference data are consistent with a null detection, while the summed data show significant signal. Therefore, the MSAM1-92 and MSAM1-94 measuring the same celestial signal, imply that the MSAM1 CMBR fluctuation measurements are uncontaminated by systematic effects at the quoted level of error.

Thesis Supervisor: Stephan S. Meyer
Title: Associate Professor, University of Chicago

A Measurement of the Cosmic Microwave Background Radiation (CMBR) Anisotropy at the Half Degree Angular Scale

by

Casey Ann Inman

Submitted to the Department of Physics
on 17 April 1996, in partial fulfillment of the
requirements for the degree of
Doctor of Philosophy

Abstract

The study of anisotropies in the cosmic microwave background radiation (CMBR) promises to be the best tool available to study the origin of our Universe. The Medium Scale Anisotropy Measurement (MSAM1) is balloon-borne telescope designed to measure anisotropies near the first Doppler peak in the CMBR power spectrum. The instrument chops a $28'$ beam in a 3 position pattern with a throw of $\pm 40'$, simultaneously measuring single and double differenced sky signals. These data in four spectral channels centered at 5.7, 9.3, 16.5, and 22.6 cm^{-1} are fit to a two component spectral model consisting of CMBR anisotropy and thermal emission from interstellar dust. The first flight of the MSAM1 instrument, made in June of 1992 (MSAM1-92), yielded detections of CMBR anisotropy. The second flight in June of 1994 (MSAM1-94) observed the same field as the first flight to confirm the earlier measurements. The MSAM1-94 flight yields both a double difference detection of CMBR fluctuations of $1.1 \times 10^{-5} \leq \Delta T/T \leq 3.1 \times 10^{-5}$ (90% confidence interval, including calibration uncertainty) for total rms Gaussian fluctuations with correlation angle $0.^{\circ}3$; and a single difference detection of $1.0 \times 10^{-5} \leq \Delta T/T \leq 3.2 \times 10^{-5}$ (90% confidence interval, including calibration uncertainty) for total rms Gaussian fluctuations with correlation angle $0.^{\circ}5$. In order to compare the CMBR and interstellar dust emission data at each celestial point measured, sum and difference of the MSAM1-92 and MSAM1-94 datasets are created. Resulting difference data are consistent with a null detection, while the summed data show significant signal. Therefore, the MSAM1-92 and MSAM1-94 measuring the same celestial signal, imply that the MSAM1 CMBR fluctuation measurements are uncontaminated by systematic effects at the quoted level of error.

Thesis Supervisor: Stephan S. Meyer
Title: Associate Professor, University of Chicago

Acknowledgments

There are numerous people without whom this work would not have been possible. I would like to thank MIT for the opportunity to meet and work with some excellent scientists. I would like to thank NASA for funding both myself and our project. I thank each and every person at the National Scientific Balloon facility for their tremendous support, providing for the successful balloon flights on which this thesis is based. I thank Steve Meyer for tremendous support, as well as Sharon, Samantha, and Neils. I thank all the people at Goddard Space Flight Center, who have made my work, and computing power so much better, especially Bob Silverberg and Walter Folz. I thank Ed Cheng for providing a roof and so much more. I thank Dave Cottingham and Dale Fixsen, without whose insight and assistance this analysis could not have gone forward. I thank Jason Puchalla for his exceptional patience and diligence.

I thank Bob Rutledge for getting me through the first year of graduate school. I thank "the Hawaii crowd" for feeding and entertaining me, Heidi O, Heidi Y and Chris, Sumilu and Ross, and Adam and Beth. I thank Lam Hui for always having something to teach, and the patience to teach me. I thank gene magnier for support above and beyond the call of friendship.

I thank my family, Diane, Les and Jill, who supported me throughout this adventure, and instilled in me the intellectual curiosity which drove me to physics. I thank my newer family Susan, Larry, Jennifer, and Stefanie, for their support and love. Finally, I thank my husband, Matthew Kowitt. I have no words to capture the wholeness he has brought to my life and work. All I will say is thank you ;-).

Contents

List of Figures

List of Tables

Chapter 1

Introduction

In 1964, working on the 20-foot horn-reflector from the Bell Telephone Laboratories (Crawford Hill, Holmdel, New Jersey), Penzias and Wilson first measured the Cosmic Microwave Background Radiation (CMBR) [Penzias and Wilson, 1965]. This momentous discovery began the use of what is arguably the best tool to study the history of the Universe.

Observationally, the CMBR is an astronomical background radiation. It has a blackbody spectrum in both spectral shape and absolute amplitude, as measured by the FIRAS (Far Infrared Absolute Spectrophotometer) on board the *COBE* (COsmic Background Explorer) satellite [Fixsen et al., 1996b], with a temperature of $2.728 \pm 0.004\,\mathrm{K}$ (95% CL) [Fixsen et al., 1996b]. It is nearly isotropic; the measurement of the anisotropy is the subject of this thesis.

Blackbody radiation is in thermodynamic equilibrium at some temperature, T. The Universe is now too optically thin (transparent) for radiation to come to thermal equilibrium. The standard explanation for the CMBR spectrum is that the Universe was once in a hot dense phase, when the radiation was in equilibrium with highly ionized matter. The expansion of the Universe, like an adiabatic expansion, cooled the radiation while preserving its thermal spectrum. When the Universe had cooled to $T \sim 10^7\,\mathrm{K}$ (at an age of ~ 1 year or redshift $z \sim 10^7$), radiative processes such as bremsstrahlung and inelastic Compton scattering ceased to be efficient, effectively freezing the number of photons in the Universe. The radiation remained tightly coupled to the matter through ordinary Compton scattering, forming a "photon baryon fluid" [Hu, 1995]. This state persisted until the expansion cooled the fluid to $T \sim 3000\,\mathrm{K}$ (at an age of $\sim 10^5$ year or redshift $z \sim 1100$), at which time neutral hydrogen formed, dropping the scattering cross-section for radiation sharply. Since this epoch, known as the "surface of last scattering," the Universe has remained transparent, allowing the radiation to free stream from this point to the present, where it is

observed as the 2.7 K CMBR. The extraordinary agreement of the CMBR spectrum with that of a Planck emitter places severe limits on the amount of energy that could have been absorbed by the radiation field at any time after the first year since the Big Bang. The temperature defines the number, entropy, and energy densities for the radiation, quantities which are critical to our understanding of cosmology.

The largest deviation from isotropy is the CMBR dipole ($\propto \cos(\theta)$), with a magnitude measured to be 3.372 ± 0.007 mK in the direction, $(l, b) = (264.^{\circ}14 \pm 0.30, 48.^{\circ}26 \pm 0.30)$(95% CL) [Fixsen et al., 1996b]. The standard interpretation of the dipole anisotropy is that it is due to the observer's proper motion with respect to the comoving rest frame of the expanding universe.

The traditional approach to quantifying CMBR anisotropies is with the two-point angular correlation function, $C(|\mathbf{x}_1 - \mathbf{x}_2|) = \langle \Delta T(\mathbf{x}_1)\, \Delta T(\mathbf{x}_2) \rangle$ where $\mathbf{x}_1$ and $\mathbf{x}_2$ are positions on the sky and θ is the angle between them ($\mathbf{x}_1 \cdot \mathbf{x}_2 = \cos\theta$), or its Legendre expansion coefficients, C_ℓ. Figure 1-1 shows several theoretical predictions for the C_ℓ's (also known as the angular power spectrum). Note that C_1, the primordial dipole, is not included in the angular power spectrum, since it is impossible to separate from the dipole induced from our proper motion. The power spectra plotted are all normalized to the large-scale anisotropy detection of the *COBE*/DMR experiment [Hinshaw et al., 1996]. The multipole moment ℓ corresponds to angular separation, $\theta \simeq \ell^{-1}$ radians, valid when $\ell \gg 1$. The series of features in the predicted power spectra, known as Doppler or acoustic peaks, are due to oscillations of the photon-baryon fluid about the initial perturbations in the gravitational potential, and are a robust prediction of a broad class of cosmological models. The ratios of the heights, locations and extent of the peaks contain a wealth of quantitative cosmological information [Hu and White, 1996]. In particular, the location in ℓ-space of the first Doppler peak is a sensitive probe of Ω_0, the density of the Universe.

Figure 1-1 also shows the results of the most recent observations of CMBR anisotropy, where the horizontal bars denote the range of ℓ over which the measurement is sensitive. One can see experiments need at least a factor of 10 improvement in signal to noise before measurements can distinguish among competing models. The large error bars are dominated by sample variance, due to the small number of independent patches of sky observed. As more sky is covered, the errors will go down appreciably, until the eventual "cosmic variance" limit is reached, due to the finite observable sky.

CMBR measurements are not, nor have they ever been, easy. The signal is small, typically tens of μK, compared to the 300 K Earth and ambient temperature optics. Thus, any telescope used to measure the signal must have extraordinary rejection of out of beam radiation ("sidelobes"), and must take care to minimize all in-beam

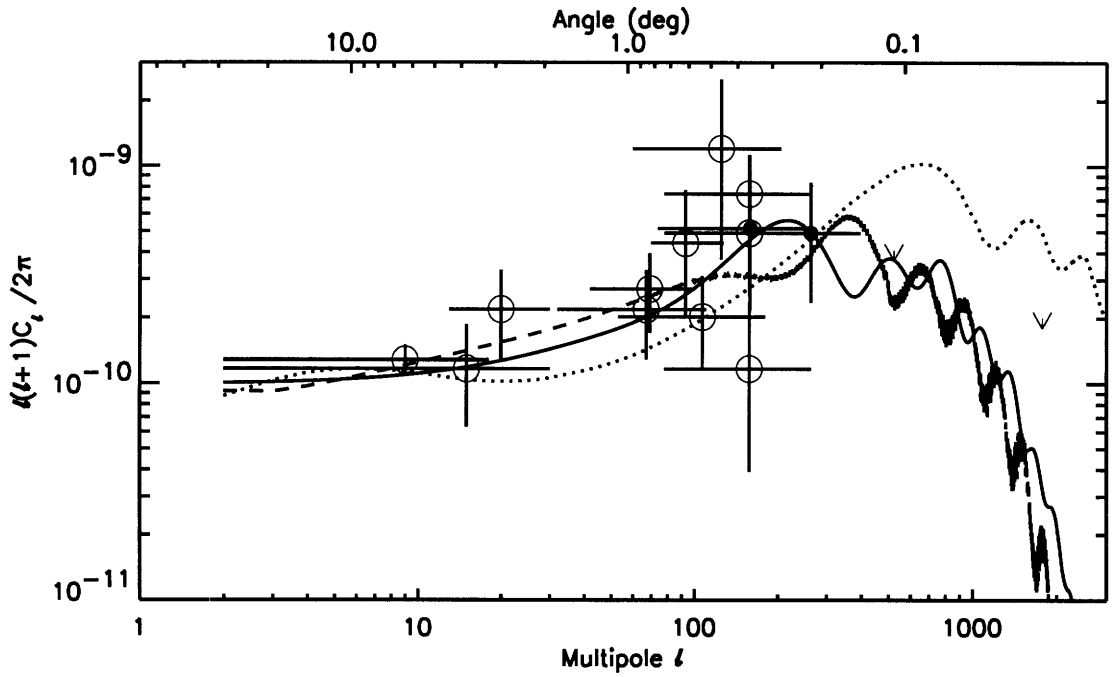

Figure 1-1: Power Spectrum of CMBR Anisotropy. The quantity $\ell(\ell+1)C_\ell/2\pi$ is approximately $(\Delta T/T_{\rm CMBR})^2$ at the angular scale ℓ. The three curves are theoretical predictions: the solid curve is a standard cold dark matter model with $\Omega_0 = 1$ [Sugiyama, 1995], the dotted curve is an open cold dark matter model with $\Omega_0 = 0.2$ [Kamionkowski et al., 1994], and the dashed curve is a texture model [Turok, 1996]. The data are tabulated in a recent review of the field [Scott et al., 1995]: from left to right, they are from DMR ($\ell = 9$), FIRS ($\ell = 15$), Tenerife ($\ell = 20$), SP94 ($\ell = 67$), Sask94 ($\ell = 68$), Python ($\ell = 93$), Argos ($\ell = 107$), IAB ($\ell = 125$), and MAX (3 points at $\ell = 158$). The two solid points are the results from MSAM1-92 ($\ell = 159$ and 263), while the two arrows are 95% CL upper bounds from WD ($\ell = 523$) and OVRO ($\ell = 1774$). The horizontal bars show the region in ℓ-space in which each experiment is sensitive.

emission from the telescope optics. As an added complication, in all but a few small windows in frequency, the Earth's atmosphere is optically thick (opaque) at the frequencies where the CMBR is brightest, making measurement from the ground very challenging. A few instruments fly on balloons, typically at altitudes of $27 - 39\,\mathrm{km}$. While above the bulk of the atmosphere, these experiments are currently limited to observe for only a fraction of the 10 or so hours of a typical balloon flight. The short observing time limits both the obtainable sky coverage and the in-flight systematics checks on the measurement. The most reliable CMBR measurements to date have been made from a satellite, *COBE*, which observed for 4 years through no atmosphere with good sidelobe rejection. Satellites have disadvantages: they are expensive and take considerable time to complete. Planning for *COBE* began in the early 1970's; it was finally launched in 1989. Planning is underway for a next generation CMBR anisotropy experiment in space, but until then the ground and balloon measurements continue to make significant progress.

In addition to the terrestrial complications to CMBR measurements, there are astrophysical complications as well. Emission from our own Galaxy, in the form of synchrotron radiation and bremsstrahlung (free-free emission) at low frequencies, and thermal emission from $\sim 20\,\mathrm{K}$ interstellar dust at higher frequencies, are sources of potential confusion for CMBR measurements. All three of these foregrounds have approximately power law frequency spectra, $I_\nu \propto \nu^\alpha$, where $\alpha \sim -0.7$ for synchrotron radiation, $\alpha \sim -0.1$ for free-free, and $\alpha \sim +3.5$ to $+4$ for dust [Bennett et al., 1992]. An experiment can use multiple frequency bands to distinguish these foregrounds from the CMBR signal. The spectra of these astrophysical foregrounds, as well as that of CMBR anisotropy are shown in Figure. 1-2. Extragalactic objects are another potential source of foreground confusion, but are only expected to be significant for arcminute-scale measurements or measurements at cm-wavelengths [Franceschini et al., 1989].

This thesis is based on measurements made with the Medium Scale Anisotropy Measurement (MSAM1) balloon-borne instrument[1]. MSAM1 has spectral sensitivity principally to CMBR anisotropy and Galactic dust, as shown in Figure 1-2. It is sensitive to anisotropy on two angular scales, corresponding to $\ell \sim 160$ and 260. It has flown three times; the first was on 1992 June 5 (hereafter, MSAM1-92), the second was on 1994 June 2 (hereafter, MSAM1-94), with the third flight being on 1995 June 2 (MSAM1-95). All three flights were extremely successful. MSAM1-92 produced one

[1]The notation MSAM1 refers to the configuration of the MSAM gondola with the Far Infra-Red Survey (FIRS) radiometer, and is the instrument on which this thesis is based. MSAM2, scheduled for its first flight in June 1996, is an upgraded version using a new radiometer built at Brown University.

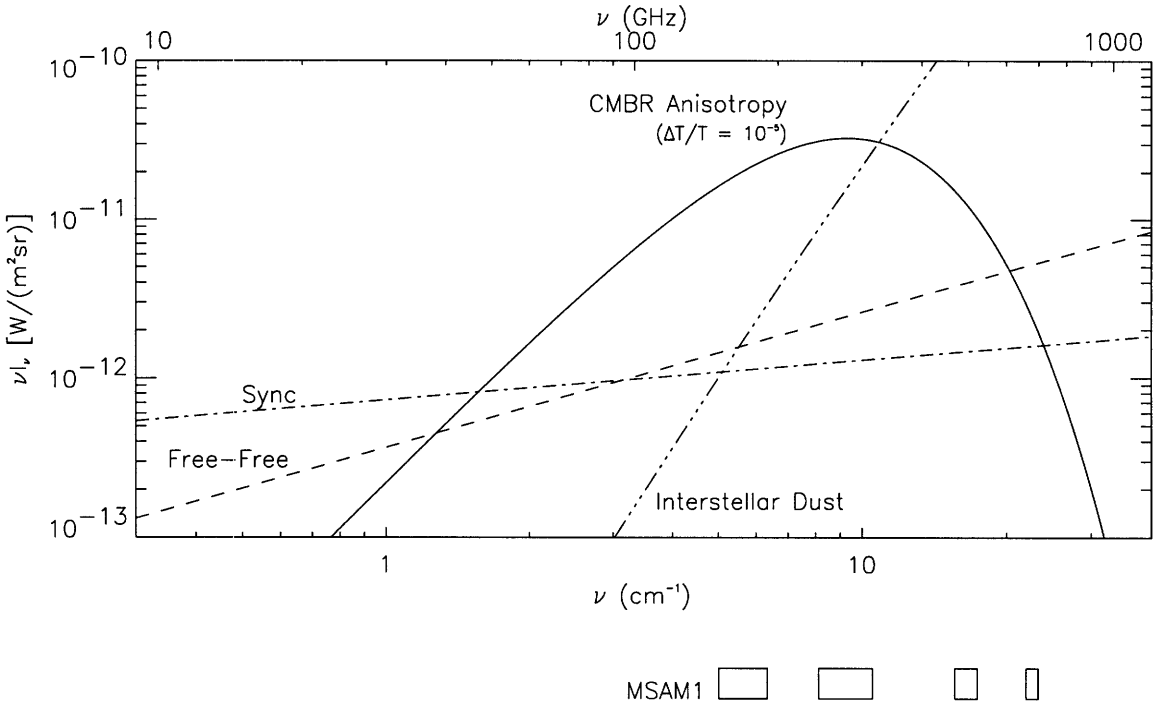

Figure 1-2: Frequency Spectra of Astrophysical Foregrounds

of the first measurements of CMBR anisotropy near the half-degree angular scale on the sky [Cheng, 1994]. The second flight observed the same region of sky as the first, confirming the earlier results, and produced the data on which this thesis is based. Preliminary results of the third flight will be published soon.

Chapter 2 covers the MSAM1 instrument. Chapter 3 describes the observations. Chapter 4 explains the data analysis. Chapter 5 contains the results for MSAM1-94 and its comparison to MSAM1-92, as well as the conclusions.

Chapter 2

Instrument

The MSAM1 instrument is designed to measure anisotropies in the CMBR. Its beam size, 28′ full width half maximum (FWHM), observing frequencies (5.7, 9.3, 16.5, and 22.6 cm^{-1}), and observing platform, on a balloon at $\sim$ 39 km, are its defining characteristics.

MSAM1 is designed to observe at the angular scale roughly corresponding to the first Doppler peak in the CMBR power spectrum. Its four channel radiometer provides good sensitivity to CMBR and thermal emission from Galactic dust. The balloon observation platform places the telescope above more than 99.5% of the atmosphere, greatly alleviating the persistent problem of atmospheric emission at all frequencies sensitive to the CMBR. A paper describing this instrument in detail [Fixsen et al., 1996a] has recently been published.

Both the gondola and the radiometer for MSAM1 flew separately on previous experiments. The term "gondola" here refers to the balloon-borne platform with its attached telescope. The gondola supported a different telescope and radiometer to map the Galactic plane in infrared emission [Hauser et al., 1984]. The radiometer had been flown three times for the Far Infra-Red Survey (FIRS) [Meyer et al., 1991], [Ganga et al., 1993], [Ganga et al., 1994], a project to map CMBR anisotropy with a 3°.8 beam, which confirmed the anisotropy detection from DMR experiment on the *COBE* satellite [Bennett et al., 1994]. The cryostat, bolometers and filter passbands are discussed in [Page, 1989], [Page et al., 1994], and [Page et al., 1990]. The MSAM1 experiment makes extensive use of balloon flight-tested hardware, which was incorporated into its design.

The instrument consists of a telescope, controlled in both elevation and azimuth, mounted to a balloon-borne platform, with a cryogenic radiometer at the secondary focus. The detected signal is the integral of the emitted sky brightness weighted by the infrared (IR) beam response of the telescope. The beam is switched to different

parts of the sky by means of a nutating secondary mirror. The main beam of the telescope has the following light path: primary mirror, secondary mirror, cryogenic input horn, filters, and finally detectors, all of which are described below. First the general features of the gondola – that is, all parts of the instrument which are not the radiometer – will be discussed. Then the radiometer-specific elements will be described. The focus will be on measured performance, pointing out along the way changes which were made for the 1994 flight.

2.1 Gondola

The main components of the instrument are shown in Figure 2-1, reproduced from [Fixsen et al., 1996a]. The instrument is carried to its $\sim$ 39 km observing altitude by a 40-million cubic foot helium filled balloon. The stainless steel cables at the top of the figure are the beginning of the flight train, and lead to a parachute, which in turn is connected to the bottom of this balloon. A titanium pin, with the cross-section of an upside down T, is the interface between the flight train and the gondola. The "jitter" mechanism (described below) sits on the wider base of the pin and suspends the gondola, allowing it to rotate with respect to the flight train. The figure shows the rigid tubular superstructure used for MSAM1-92, which was subsequently replaced with a cable suspension system for MSAM1-94 and later. This attaches to an aluminum frame which supports the telescope and support electronics.

The gondola pointing system moves the telescope in azimuth and elevation. The azimuth of the entire gondola is controlled. There is a large flywheel (the "azimuth wheel") mounted to the bottom of the gondola. Applying torque to this wheel causes the gondola to counter-rotate, thus maintaining constant angular momentum in the gondola system. The gondola azimuth servo system drives this wheel to control the gondola azimuth, using either the primary magnetometer or the gyroscope signal as a position reference, depending on the mode of operation. The primary magnetometer is mounted to the gondola outer frame, as far removed as possible from magnetic materials on the gondola. It is a two-axis device, which has an absolute accuracy of about 1° after correcting for a temperature dependent offset in flight. This reference sensor is used for coarse pointing. The main gyroscope is a two axis rate gyroscope mounted coaxially with the telescope beam. It is aligned such that one axis (Y-gyro) is in the direction of telescope elevation, and the other (X-gyro) is in the cross-elevation or local azimuth direction. The gyroscope is considerably stabler (discussed more in Section 2.1.4) than the magnetometer, and has the advantage that it defines an approximately inertial reference frame. Thus the gyroscope is the pointing reference

for all astronomical observations. There is also a secondary magnetometer which is not connected to the pointing system. This magnetometer could be used from the ground to determine where the telescope was pointed if the primary magnetometer failed.

The gondola is not completely free at the top of the superstructure; it is weakly coupled through the jitter mechanism to the flight train. This mechanism consists of a bearing which rests on a second bearing which rests on the base of the titanium pin, which is connected to the flight train. An axle between these two bearings is connected through a belt to a motor mounted to the gondola. This motor drives the belt applying a torque from the gondola to the flight train, transferring to the flight train angular momentum which builds up in the gondola due to electrical or mechanical biases. In the MSAM1-92 configuration the additional moment of inertia of a "jitter bar", attached to the bottom of the flight train, was required for the bearings to operate properly. New lower friction bearings in the MSAM1-94 configuration obviated the need for this bar.

Mounted to the metering structure (the "strongback"), are the following devices: the main telescope optics (the primary mirror, the secondary mirror, and the radiometer), the secondary "chopper mechanism", the star camera(s) (used for absolute telescope pointing determination), the gyroscope (used for short term, high precision pointing determination), and the support electronics for some of the above. The secondary chopper mechanism is used to move the secondary mirror. The strongback is controlled in elevation, supported by two elevation control motors mounted symmetrically to the sides of the gondola frame. The gondola elevation servo system drives either one or both of these torque motors, using either a digital elevation encoder or the Y-gyro signal from the main gyroscope as a position reference.

Not shown in Figure 2-1 are various sensors mounted throughout the instrument. There are numerous temperature sensors on the mirrors and ground screens,as well as in electronics boxes. Two pressure sensors measure ambient pressure. A Global Positioning System (GPS) unit measures the latitude, longitude, and altitude of the gondola. There are also voltage and current monitors for nearly all the motors and batteries. While useful for diagnosing problems, most of the sensors are not used in the analysis. Those used in the science analysis include primary mirror thermometers, the pressure sensor, and the secondary magnetometer. The average sensor readings for a typical period in the flight are given in Appendix H.

The elements not mounted to the strongback include the azimuth drive, the servo electronics, gondola data acquisition electronics, the balloon to ground communication electronics, the batteries, and the crush pads. The command up-link and

telemetry down-link between the ground and the balloon are done through the Consolidated Instrument Package (CIP) provided by the National Scientific Balloon Facility (NSBF) [National Scientific Balloon Facility, 1996].

The crush pads are made of stacks of corrugated cardboard, and are added just before flight to help cushion the instrument on landing. Not shown are the extensive ground shields: reflective aluminum surfaces added to the gondola to reduce unwanted radiation. The primary ground shield is mounted to the strongback, and extends from the sides of the primary, below the cryostat, to roughly 60 cm beyond the secondary mirror. This prevents emission from gondola elements and Earthshine from hitting the cryostat input horn, the secondary mirror, and most of the primary mirror. The CCD star camera is mounted just outside of this shield, below the secondary mirror.

In the MSAM1-92 configuration shown, additional ground shields were mounted to the upper horizontal bar of the gondola frame, angled away from the gondola center by about 30°, to prevent Earthshine from reflecting off the superstructure into the beam. There was also a conical ground shield mounted below the jitter bar to prevent the telescope from seeing emission or reflection from it. In the MSAM1-94 configuration the reflections off the superstructure were reduced such that the additional ground shields were deemed unnecessary.

2.1.1 Telescope Optics

The telescope is a 51° off axis Cassegrain design with a nutating secondary. The primary mirror is a section of an off-axis parabola, 1.37×1.52 meter with a focal length of 1.47 meter, machined from a single piece of aluminum. The mirror is designed to be larger than the beam with an unilluminated "guard ring". The guard ring is measured to be 10(5) cm from the edge of the mirror when the secondary is in the central (side) position at roughly the -15 dB level.

The secondary mirror is a convex hyperbola, with a 0.276×0.315 meter elliptical edge, also machined from a single piece of aluminum. It acts as the limiting optical stop. The mirror is rotated $\pm 1.^{\circ}79$ about its vertical axis by the chopper mechanism, moving the beam $\pm 40'$ on the sky. The beam is continuously switched in a square wave pattern between three positions on the sky, making two complete cycles (center, right, center, left, center, right, center, left) per second. Two signals, one proportional to the difference between left detected signal and right detected signal (the "single difference"), and the other proportional to the difference between the center detected signal and the average of side detected signals ("double difference") are formed from the signal time stream. The single difference has a two lobed beam pattern on the sky with $80'$ beam separation, while the double difference produces a three lobed beam

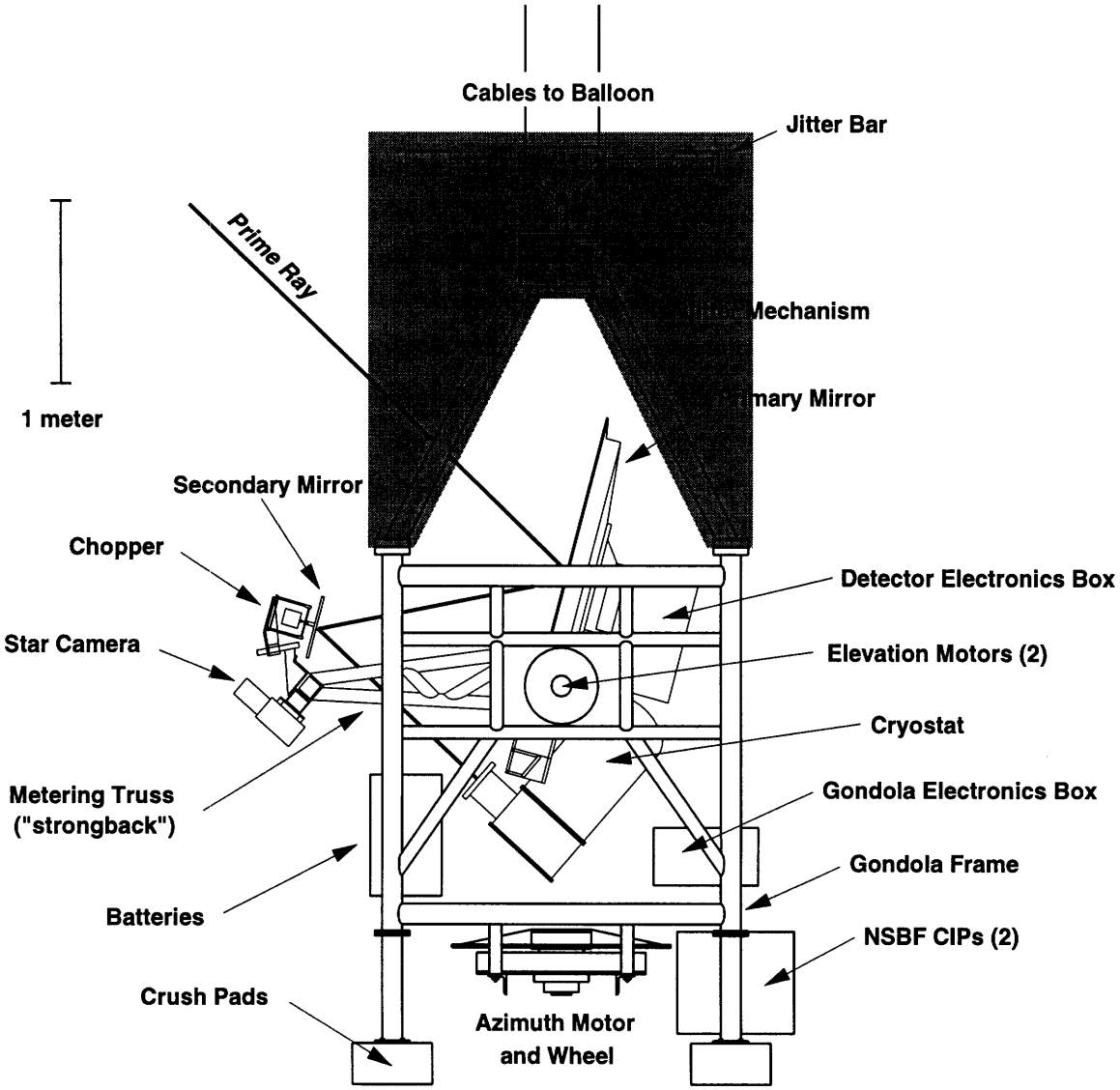

Figure 2-1: Schematic of MSAM1 Gondola (from [Fixsen et al., 1996a]). The configuration shown is for MSAM1-92. For MSAM1-94, the shaded region was replaced with a stainless steel cable superstructure.

pattern on the sky, with 40′ beam separation (both are shown in Figure 2-2). This beam-switching provides the first level of sky signal modulation, and will be discussed repeatedly throughout the thesis. The secondary position is stable to 4″ on the sky, as measured by the linear variable differential transformer (LVDT) position sensor.

2.1.2 Instrument Sidelobe Measurement

The amplitude of CMBR anisotropy is expected to be tens of μK. This amplitude is the "Earthshine", the 300 K the Earth presents through roughly 2π steradian. Thus, the instrument response at large angles from the main beam, or sidelobes, must be extremely small to avoid contaminating the expected signal. To measure the sidelobe response prior to flight, a 30 mW 150 GHz radiation source, mounted at the focus of a 1 meter on-axis Cassegrain transmitting telescope ($\sim$ 55 dB gain), was used. The transmitting telescope was placed on the top of the 25 m control tower at the NSBF in Palestine, TX, while the MSAM1 telescope was placed 740 m away in an open field (the "old launch pad"). The transmitting telescope was kept fixed, and the MSAM1 telescope was stepped in elevation for this test. When the MSAM1 main beam was pointed at the transmitter, the transmitted power was attenuated by inserting 2 layers of microwave absorbing material (Eccofoam) in the feed optics. The combination of the inserted Eccofoam and the commandable gain (1-1024) provided the dynamic range for the measurement. The uncertainty in this measurement is roughly 3 dB, dominated by uncertainty in calibrating the Eccofoam attenuation. The radiation source was modulated at $\sim$ 0.85 Hz, an incommensurate frequency with that of the secondary chopper (2 Hz). Both the full power response and "chopped" response, that modulated by the chopping secondary mirror, are obtained by measuring the $\sim$ 0.85 Hz signal and the $\pm$ 0.85 Hz sidebands around the 2 and 4 Hz signals.

Before the 1994 flight, the technique above was used to measure the far-field sidelobes of the MSAM1 instrument to roughly the -100 dB level. The measurements are shown in Fig. 2-3. The open symbols show the total power response, while the filled symbols show the chopped response. The modulated response is a factor of 10 to 20 dB lower than that of the full power. The chopped response is -80 dB to -90 dB for angles $\geq 20°$ from the main beam. In addition to the steps in elevation, the telescope was held at the 45° elevation, and rotated in azimuth in 10° steps. Those results are not shown, but were measured to be better than -90 dB everywhere except in the vicinity of the back lobe (180° from the main beam) where the response is -80 dB.

One might think that sidelobe rejection of greater than -120 dB is necessary to ensure that the measurement is not contaminated by Earthshine. However, this level is likely to be overly stringent, since it neglects the additional rejection gained

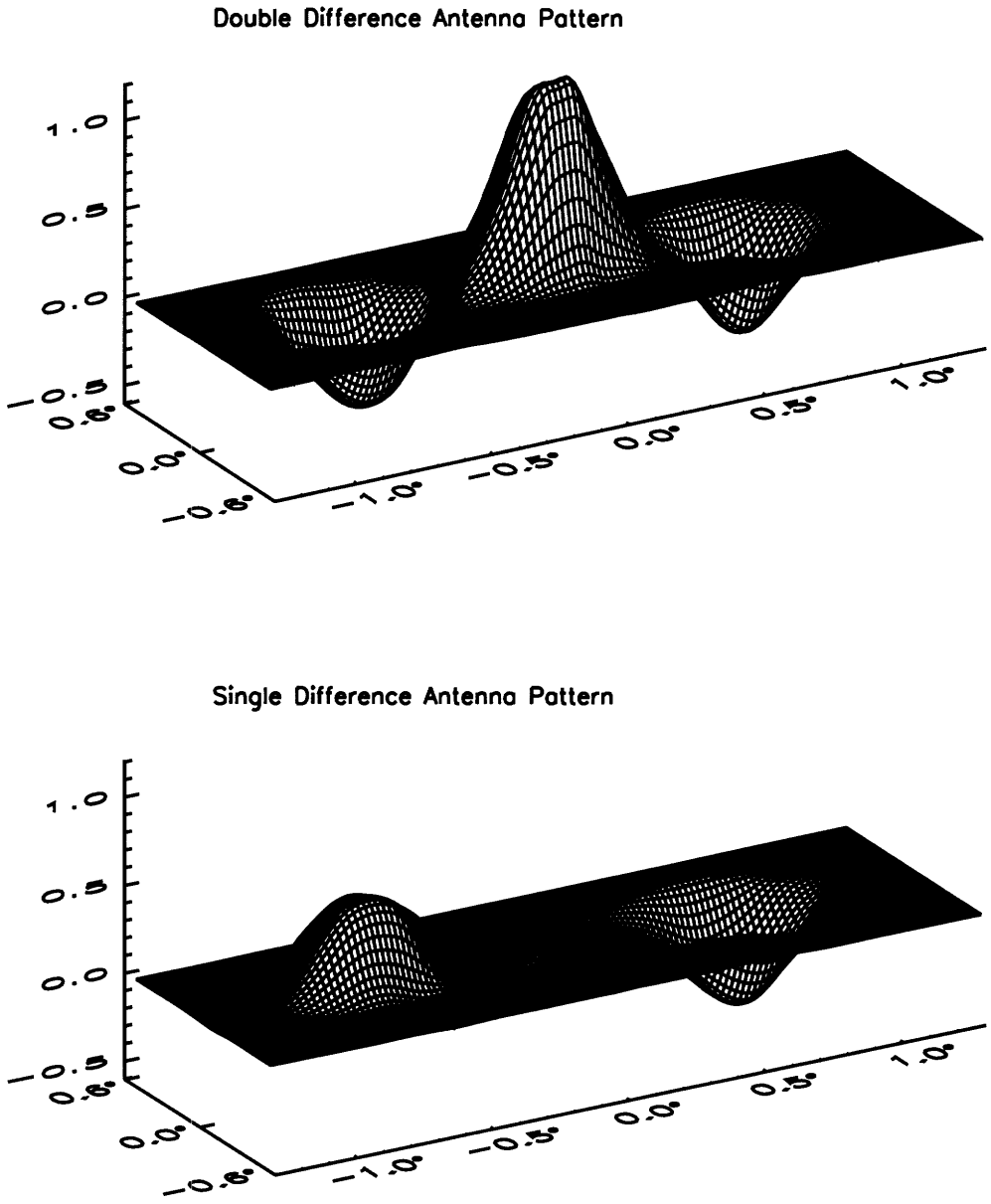

Figure 2-2: Single Difference and Double Difference antenna response for Channel 1. The other channels have similar antenna patterns.

from modulating the sky signal. The observing strategy, discussed in Chapter 3, implements this modulation. While sky modulation is likely to provide the several tens of dB additional rejection necessary, it is difficult to demonstrate this *a priori*. This is one of the main motivations for observing the same sky in MSAM1-94 as in MSAM1-92.

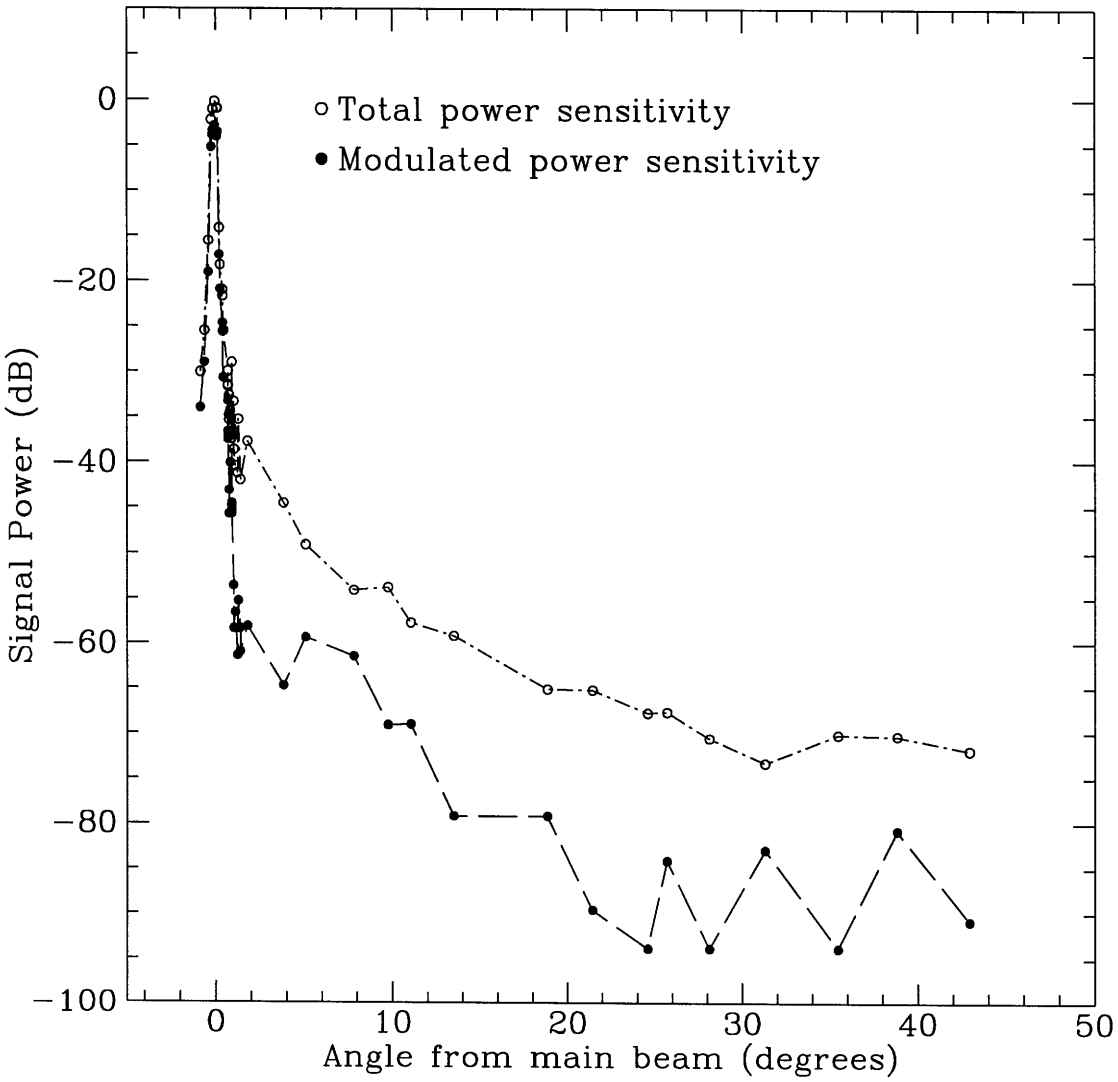

Figure 2-3: Measurement of Sidelobe Response of MSAM1

2.1.3 Flight Operation

Overlapping sky coverage in two CMBR balloon flights had not been accomplished before MSAM1-94 observed the same sky as MSAM1-92. Achieving this overlap, as well as executing the observing strategy (see Chapter 3) on the whole depends on being able to point the telescope at a specific place on the sky at a specific time. To accomplish this a number of things must be determined in flight. First, the IR beam center, must be determined relative to the star camera. This was done by moving the telescope toward Jupiter, which is bright in both visible and IR/submillimeter radiation. Once Jupiter was seen in the camera, a "raster" was performed over the planet and the detector data was analyzed to measure a main beam centroid. The raster is a series of horizontal scans uniformly spaced in elevation, intended to map a rectangular region on the sky, the parameters of which are given in Chapter 3. The telescope was moved so that the IR main beam pointed directly at Jupiter. The position of Jupiter in the star camera was then used for the remainder of the flight as the pointing reference. Because the observing strategy is time critical, the observation parameters were determined and uploaded in realtime.

The telescope is controlled remotely from the NSBF balloon base, via the radio command up-link system provided by the balloon facility. While the telemetry down-link is fairly reliable, the up-link is unreliable and slow. The gondola system has a flight sequence table composed of a series of addresses, or "slots," where once the operation in a given slot is finished, the gondola performs the operation in the next slot. For a list of the slots and what functions they execute see Appendix I.

2.1.4 Pointing Stability

The gondola must be able to point stably in elevation and azimuth to implement the observing strategy. Pointing stability is determined by looking at the power spectrum of the gyroscope signals when the gondola is tracking a celestial point. The average electronic noise, $0\farcm5 - 0\farcm6 / \sqrt{\text{Hz}}$, is determined by fitting the power spectrum above 0.1 Hz. The X-gyro readouts for an in-flight stationary period are shown in Figures 2-4 (the X-gyro readout has a similar power spectrum). The gondola position is stable to the limit of this readout noise at frequencies of $0.03 - 0.05$ Hz, below which some arcminute-scale wander is apparent. This slow wander is small compared to the beamsize, therefore not significant on the time scale of the observations.

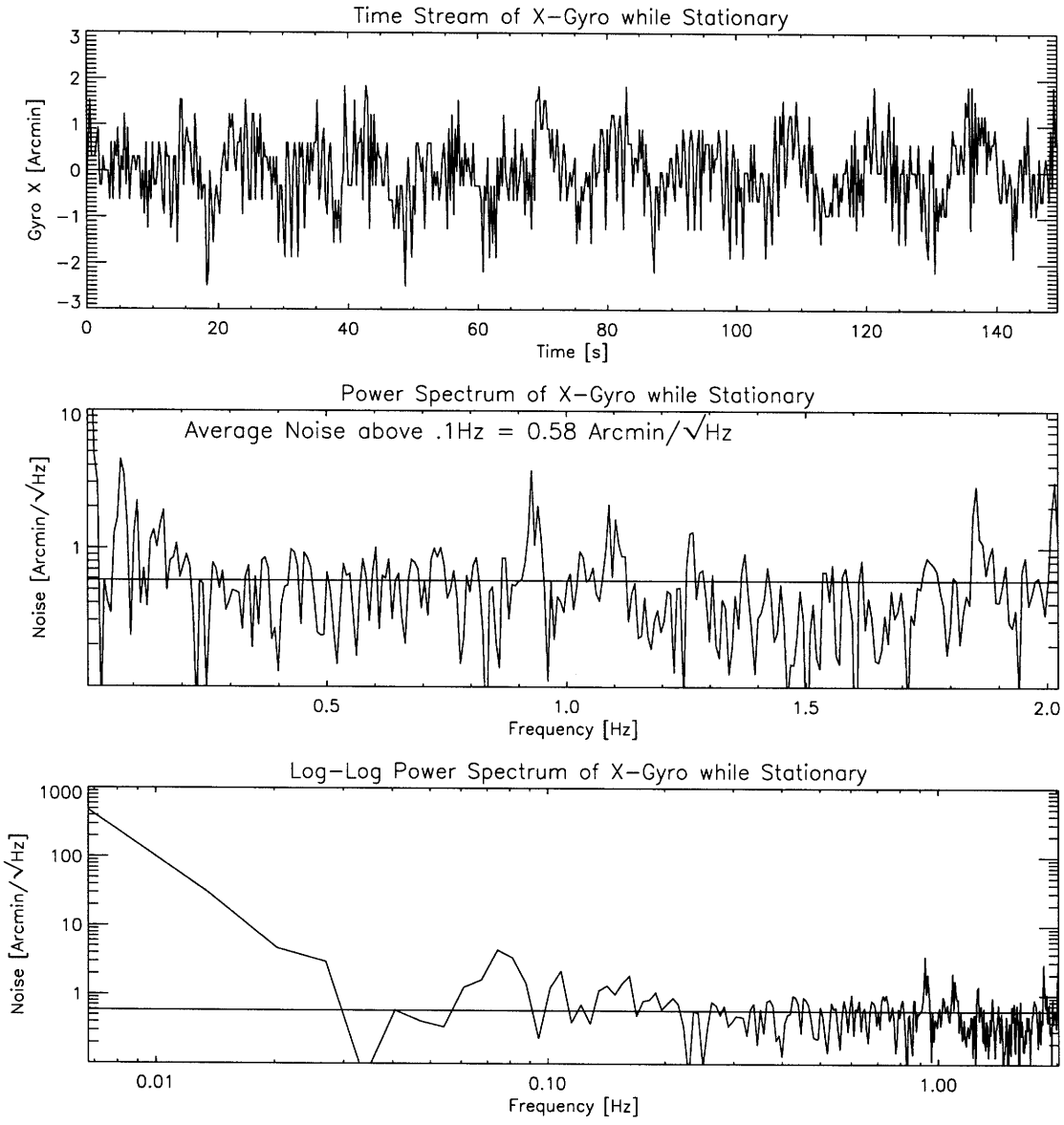

Figure 2-4: Position Readout Noise in Cross-Elevation

2.1.5 Pointing Accuracy

As discussed in Section 2.1.3, the observing strategy depends on an in-flight pointing determination, as well as a careful post-flight determination. For this, a CCD camera is used to determine the absolute pointing of the telescope. In 0.1 seconds of integration time, the camera has sensitivity to stars of $M_V \sim 7$ in a $9^\circ \times 6^\circ$ field of view. The CCD image allows for an absolute pointing solution to slightly better than $0'.9$. Alignment of the camera to the infrared beam is fixed by observing Jupiter and determining the camera coordinates of the IR beam. The time synchronization between the camera and the main data stream was insufficient to use the camera as a short time scale position reference. However, the package was inertially stationary, typically for 2 minutes every 20 minutes, at which times the camera pictures were used to determine the absolute position, and the drift of the gyroscope signals over this time (typically $< 2'$). Between these stationary periods the gyroscope signals are used to interpolate the gondola position. For the 1992 flight, an older and less sensitive CID camera was used in the same way for a pointing reference.

2.2 Radiometer

The radiometer receives incident light from the telescope, filters it, and measures the incident power. The radiometer consists of beam forming optics, band defining filters, a set of monolithic silicon bolometers, and readout electronics, all housed in a cryogenic environment.

2.2.1 Overview

Liquid nitrogen (LN_2), liquid ^{4}He (LHe) and pumped ^{3}He are used to cool the detectors, filters, and input optics. The ^{3}He system, described in [Page, 1989], consists of a ^{3}He reservoir connected through a 2.21 cm pump tube to a zeolite reservoir. Zeolite adsorbs ^{3}He very efficiently at temperatures below roughly 15 K. The system works by condensing all the ^{3}He into its reservoir while the zeolite is warm ($\sim$ 32 K). Then the zeolite is cooled to 4.2 K at which time it pumps on the ^{3}He reducing its temperature to 0.24 K. The outside of the ^{3}He reservoir is the 0.24 K cold plate. A gauge regulator maintains a pressure of 200 mbar over the LN_2 at float, giving it a temperature of roughly 67 K. The gauge pressure is selected to keep the LN_2 from freezing, avoiding problems with thermal conduction to the metal LN_2 enclosure. An absolute regulator maintains roughly atmospheric pressure over the LHe, so it maintains 4.2 K throughout the flight. Keeping the LHe at atmospheric pressure prevents oscillations

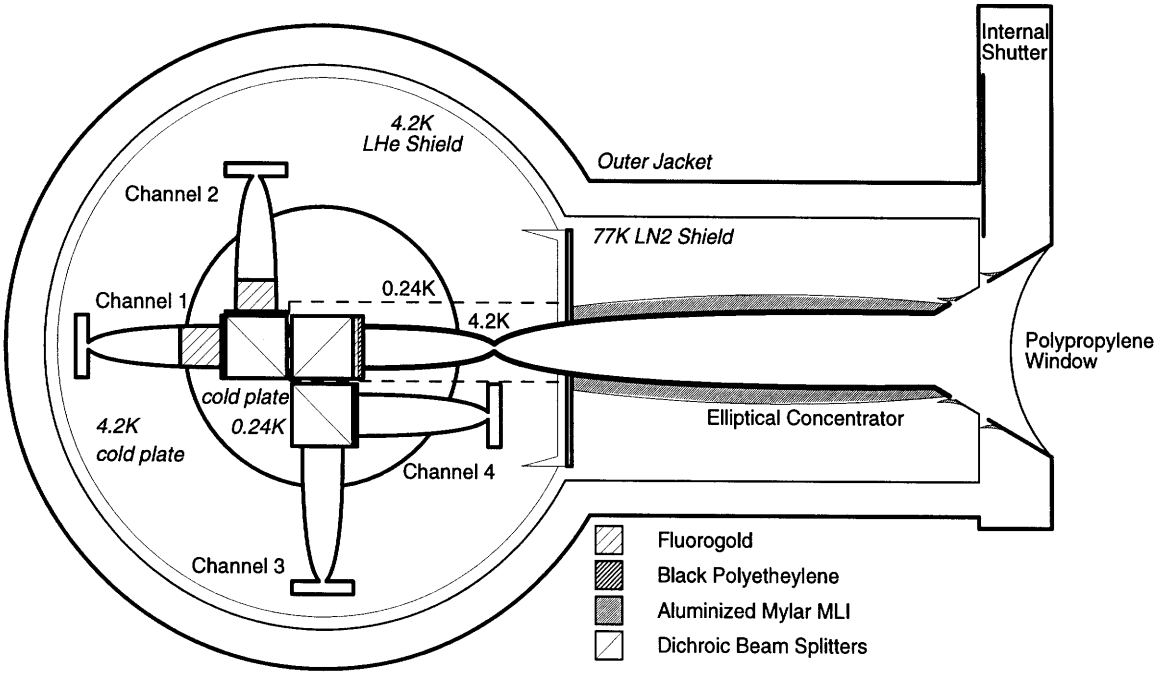

Figure 2-5: Schematic diagram of the cold optics in the radiometer. The polypropylene window and outer jacket are at ambient temperature ($\sim$ 235K). The internal shutter is near 77K. The elliptical concentrator, and first optics block, including first dichroic splitter, are 4K. The rest of the optics are maintained at 0.24K.

from developing during ascent which might deplete the LHe, as well as preventing a superfluid transition.

Radiation from the sky reflects off the telescope mirrors and passes through the window of the radiometer, where it is collected by the beam forming optics (Winston cones [Welford and Winston, 1978] and an elliptical concentrator. The elliptical horn is mounted to the 4.2 K stage (see Fig. 2-5), and has a design area $\times$ solid angle product, *étendu*, of 0.5 cm^2 steradian. The elliptical horn concentrates light from the secondary mirror onto the waist of the horn (4.5 mm diameter), and was designed assuming geometrical optics to have response of less than -40 dB at the edge of the secondary. Diffraction degrades this performance most in the lowest frequency channel. Measurement shows that 10% of the radiation falls off the side of the secondary mirror in the 5.7 cm^{-1} channel (this fraction is about 4% for channels 2 and 4, and slightly less for channel 3).

After passing through the elliptical concentrator, the light is expanded by the Winston cone into a light pipe, split, and passed through the band defining filters. Because the detectors are roughly insensitive to frequency, pass band filters are required to select the radiation for the desired frequency bands. The filters used have effective frequencies, $\nu_{\rm eff}$, as defined in [Page et al., 1994], of 5.7, 9.3, 16.5, and 22.6 cm^{-1}, with effective bandwidths, $\Delta\nu_{\rm eff}$ =1.3, 2.2, 1.9, and 1.32 cm^{-1}. For each channel the spectrum of the dominant emission source over the frequency passband is used to obtain the effective frequency and bandwidth. For the two lower frequency channels these are obtained by averaging over a CMBR anisotropy spectrum, while for the higher two channels a Raleigh Jeans (RJ) spectrum modified by an emissivity proportional to ν^2, characteristic of thermal emission from Galactic dust, is used.

The detector elements are monolithic silicon bolometers. A thermistor, in this case an ion-implanted non-degenerate conductor, is a part of a larger silicon element. The silicon is covered with a thin layer of Bismuth to absorb the radiation. The silicon element is suspended by thin silicon "legs" which electrically connect the thermistor to the signal electronics, and provide a weak thermal connection to the 0.24 K cold bath. Incident photons heat the absorber, changing its temperature. The thermistor, which is biased with some average current, has a steep resistance as a function of temperature, R(T), so a small temperature change produces a large resistance change, which in turn produces a voltage change. The voltage responsivity, $S(V/W)$, is the change in voltage produced at the top of the biased bolometer for a given change incident power. Signal electronics (shown in Figure 2-7), amplify the small signal from the bolometer for input to the telemetry stream.

The bolometers are described in [Downey et al., 1984]. They have resistances of

$\sim$ 100 MΩ at 240 mK. The noise equivalent power (NEP) is $\sim 3 \times 10^{-16}$ W/$\sqrt{\text{Hz}}$. The high efficiency and the large *étendu* of the system give the radiometer a noise equivalent temperature (NET) of $\sim 200\,\mu\text{K}_{\text{RJ}}\sqrt{s}$.

The radiometer telemetry stream is created in the Main Electronics Box (MEB), which collects the detector signals as well as various radiometer and gondola sensors into a digital format which can be relayed to the ground by the CIP. The telemetry frame rate is 0.5 Hz, and all sensors are sampled at least once in a frame. The MEB was converted from its FIRS configuration, removing the drive electronics for the FIRS cryogenic chopper, and replacing it with drive electronics for the MSAM1 secondary chopper. This radiometer telemetry stream is augmented with pointing information from the gondola telemetry stream after both streams have been separately transmitted to the ground.

2.2.2 Band Pass Filters

A good knowledge of the instrument frequency response, a full description of which can be found in [Page et al., 1994], is critical in interpreting the final results. The incoming radiation is first split with a capacitive grid dichroic filter at 45° (Figure 6 in [Page et al., 1994]). After this first split, both arms are split again with single layer inductive cross mesh (ICM) dichroic filters also at 45°. The band defining filters for channels 1,2 and 3 are composite ICM filters in a double quarter wave configuration, built at MIT. The Channel 4 filter is a multilayer inductive mesh purchased from Cochise Instruments. In addition, there is black polyethylene before the first dichroic which acts to absorb short wavelength out of band radiation. A plot of the band passes is shown in Fig. 2-6.

2.2.3 Signal Electronics

The signal electronics inside the cryostat use Junction Field Effect Transistor (JFET) preamplifiers, operated as unity gain source followers and biased by warm electronics mounted to the side of the dewar. These warm electronics were improved for the 1994 flight. The new design allowed for both the amplified AC signal and the DC level to be read out in the time stream. The DC level provides the operating resistance of the detectors, a useful systematic check.

The amplifier circuit used for the 1994 flight is a modification of a circuit design by Dan MacCammon of University of Wisconsin, and is discussed in Appendix A. The cold JFETs are run in a source follower configuration, which while providing no voltage gain in the first stage, reduces the line impedance of the signal from roughly

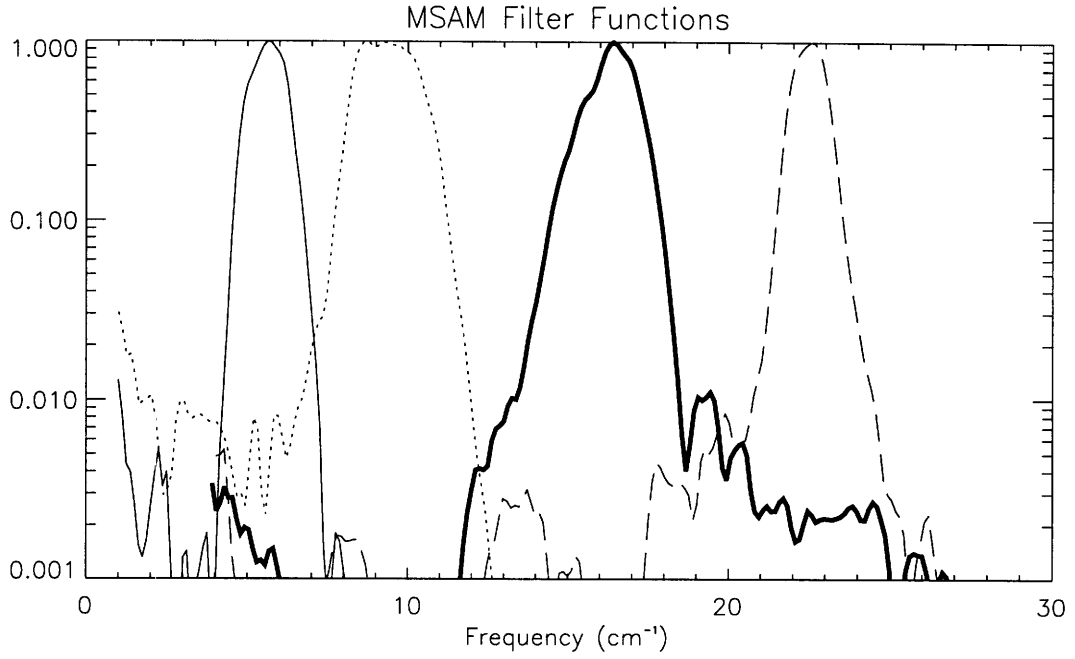

Figure 2-6: Normalized transmittance of the radiometer are shown for all four channels, 5.7 to 22.5 cm^{-1} from left to right.

100 MΩ to roughly 5 kΩ, greatly reducing sensitivity to electrical pickup in the wires. The warm circuit has a gain of 10 at DC and a gain of 300 above 1Hz (3dB at 0.07Hz). The achieved voltage noise of this circuit is better than $5nV/\sqrt{Hz}$ at 2 Hz referred to the input to the cold JFET (point A of Figure 2-7). More traditional systems require dedicated batteries to achieve low noise performance. This amplifier operates entirely from regulated power supplies. The addition of the DC level, battery free operation, and the improved stability of the system were dramatic improvements over the previous amplifier system.

A schematic of the full signal chain is shown in Figure 2-7. The radiant power is incident on the bolometer, where the thermistor ("Rbolo") responds to the temperature change, changing the voltage at the gate of the internal JFET ("internal preamp", point A on Figure 2-7) . Rbolo is mounted to the 0.24 K stage. The internal preamp is mounted to the 4.2 K stage through thermally non-conductive supports, and is temperature regulated to 80.5 ± 0.5 K. This temperature stability is not critical when running the JFET in the follower configuration. The "external preamp" is the amplifier described above. It is mounted to the outside of the dewar, and temperature regulated to roughly 298 K. The rest of the electronics are mounted in the MEB, which is temperature regulated to roughly 303 K. Here the signal is split into

its DC and AC components. The DC level is sampled at 0.5 Hz. The AC component contains the sky signal. It is put through an anti-aliasing elliptical filter, which greatly reduces sensitivity above 8 Hz, and then multiplied by a digitally controllable gain (1-1024). Finally, the signal is sampled at 32 Hz and digitized by integrating A/D converters. Appendix B discusses the achieved in-flight noise performance of the instrument.

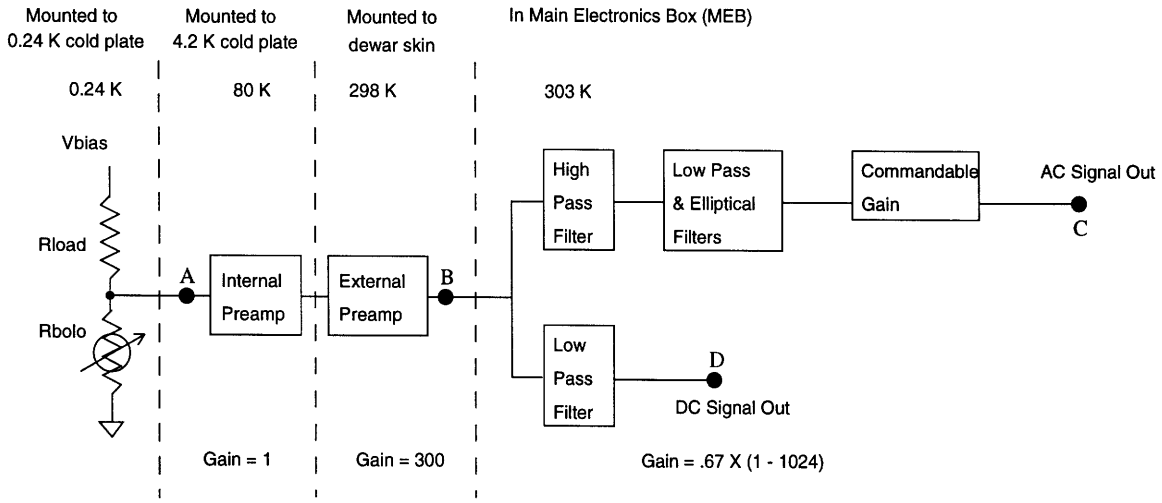

Figure 2-7: Full Detector Signal Chain

Chapter 3

Observations

The observations made for this thesis are from the 1994 flight of the MSAM1 instrument (MSAM1-94). The goal for this flight was to confirm the sky signal measured in the first flight, MSAM1-92. MSAM1-94 observed a similar patch of sky as MSAM1-92, from a right ascension of $\sim$ 15 to $20^{\rm h}$, at declination $+82°$.

The instrument was brought to the National Scientific Balloon Facility, in Palestine, TX, for testing and flight preparation on 1994 March 28. The package was launched on 1994 June 2 00:59 UT. Observations do not begin immediately after launch; the instrument must ascend to near the desired observing altitude, the "float" altitude, and recover from the shock of the initial launch and ascent. The ascent rate was fast, $\sim 7\,{\rm m/s}$ (see Fig.3-1) compared to a more normal $\sim 4-5\,{\rm m/s}$, which added roughly an hour at float altitude ($\sim 38\,{\rm km}$). The downward wind of ascent precluded pointing the telescope in elevation for the first 1.2 hours after launch. Once elevation control was established the package was still rotating uncontrollably ($\sim 7\ °/{\rm s}$). Once the rotations slow to $\sim 0.5\ °/{\rm s}$, control was established in azimuth as well. These numbers are typical for the MSAM1 flights. A flight summary for the 1992 and 1994 flights are given in Appendix C.

The in-flight activities fall into three categories: system tests, planet observations, and CMBR observations. The system tests are described in an instrument paper [Fixsen et al., 1996a].

Jupiter is observed to calibrate the instrument and map the telescope's main beam. The observations consist of a raster and one or more scans of the telescope centered on the planet. Jupiter ($\sim 40''$ in diameter) is much smaller than the beam, so it acts as point source. The raster is a series of slow ($4'$ per second) scans in cross-elevation at each of 9 different elevations. The telescope pointings for the raster used to determine the beam response are shown in Figure 3-2. The telescope starts from center, moves to a cross-elevation approximately $1.^{\circ}6$ degrees to the left, moves up $0.^{\circ}5$ in elevation,

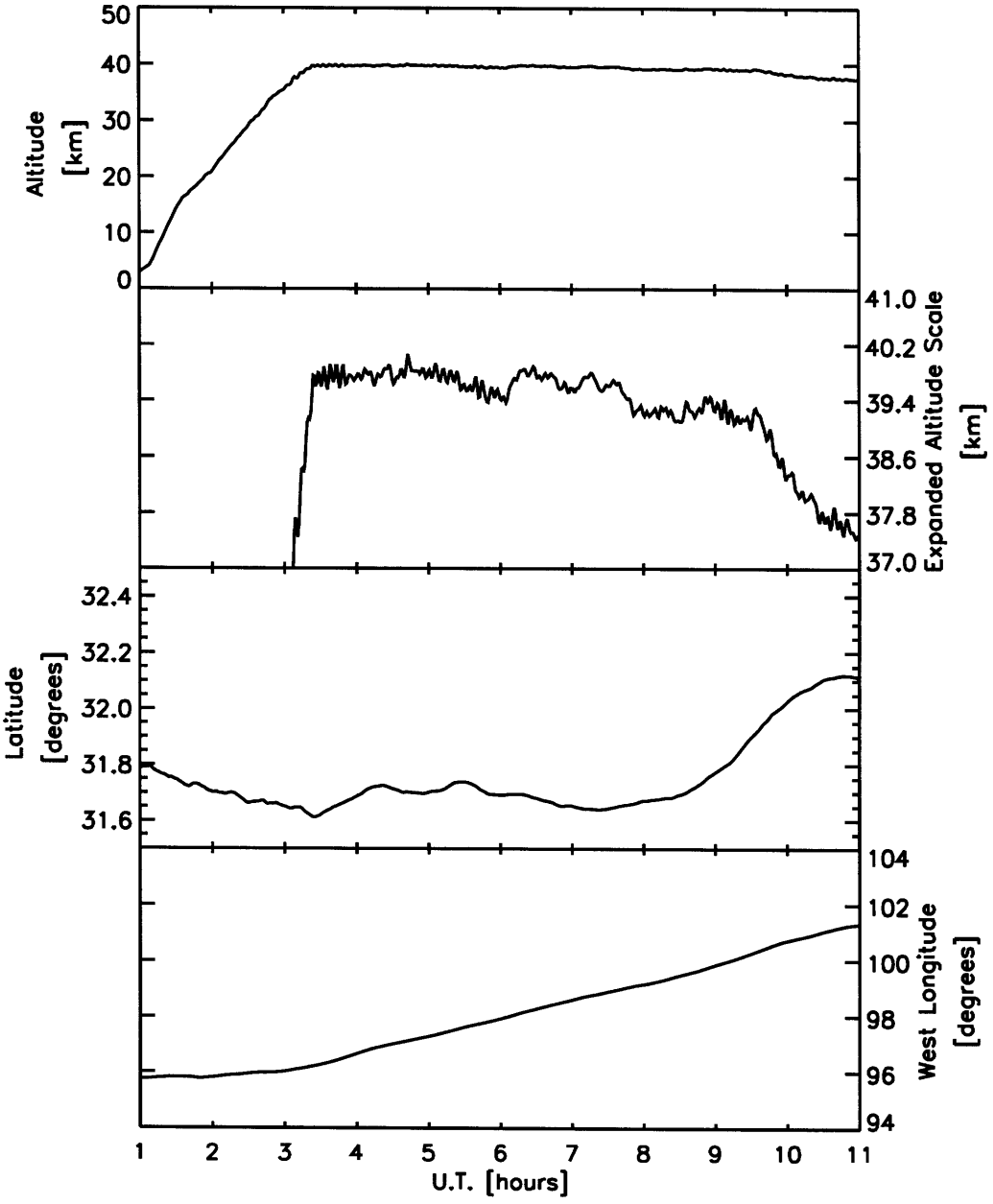

Figure 3-1: Altitude, Latitude and Longitude for the MSAM1-94 flight. Note the latitude scale is expanded 10 times relative to that of the longitude scale.

and begins scanning to the right. At the end of the first scan, at approximately 1.°6 to the right, the telescope moves down in elevation by 7.′5, and then scans back to the left. The raster is used to register the pointing of the telescope main beam to the camera beam. The raster is analyzed in real-time to obtain a beam centroid, and the location of Jupiter in the camera at that time is used as the pointing reference for the beam center for in-flight operations. This determination is within a few arcminutes of the final post-flight determination. Two or three rasters are performed in order to measure a consistent beam center prior to further observations.

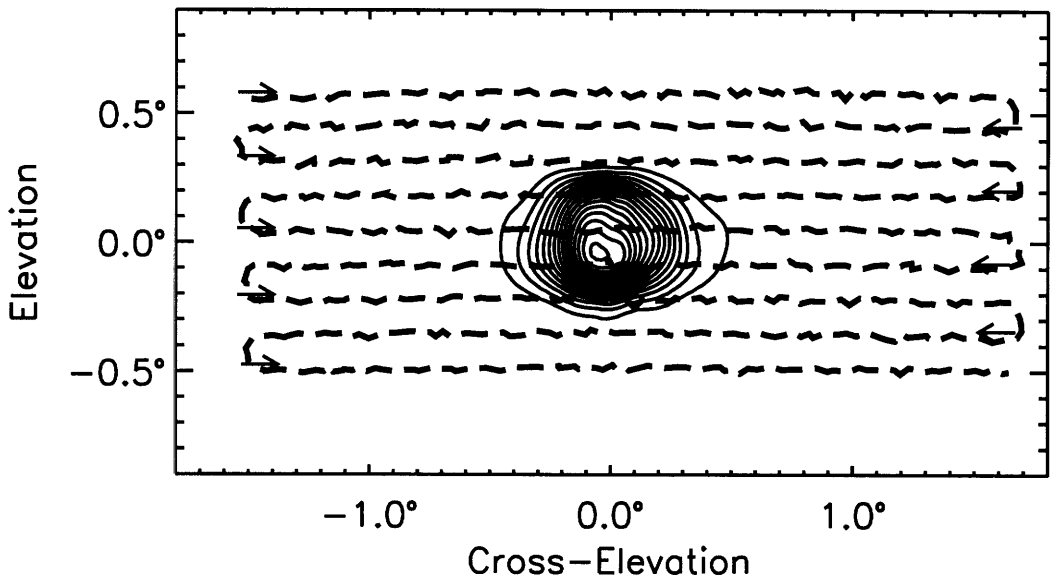

Figure 3-2: An in-flight "raster" is shown. The raster is series of horizontal scans uniformly spaced in elevation shown above as heavy dashed lines, intended to map a rectangular region on the sky. The raster pattern starts in the center, then continues moving first horizontally then vertically (not shown) to the upper left corner of the region. After finishing the series of horizontal scans, the telescope moves back first to the original elevation, and then to the original azimuth, finishing in the center of the region. The main beam response measured for channel 1 is overlayed for comparison.

The gondola is operated to minimize contamination from Earthshine, instrumental offsets and atmospheric gradients, while measuring true sky signals on two different angular scales. The CMBR observations are performed at nearly constant telescope elevation, to minimize modulation of Earthshine and reflections from the local gondola environment. Also, the highest attainable telescope elevation is used, to minimize both Earthshine and atmospheric emission (which is $\propto 1/\sin(\theta)$, where θ is the angle

measured from the horizontal). For the MSAM1 gondola this is $\sim 40°$. For flights from Palestine, TX (32° N latitude), this means north-looking observations are roughly at declination +82°(Galactic latitude ($\sim 30°$)), 8° above the North celestial pole.

The principle behind the observing strategy is to provide several levels of modulation on the sky signal, so as to distinguish it from more slowly and smoothly varying offset drifts. The first level of modulation is rapid beam-switching. This is accomplished by chopping of the secondary mirror (see first panel of Fig. 3-3) at 2 Hz, well above the $1/f$ knee of the signal electronics ($\sim$ 0.8 Hz) and the atmosphere. The beam is continuously switched in a square wave pattern between three positions on the sky, making two complete cycles (center, right, center, left, center, right, center, left) per second.

The absolute sky brightness is not measured by this experiment, but rather the difference in sky brightness between patches of sky separated by a set distance. Two sky difference signals are obtained from the beam switching. The single difference weights the secondary-left data positively while weighting the secondary-right data negatively, where secondary-left, -right, or -center data are that taken when the secondary is in the left, right, or center position of its cycle, respectively. This gives a signal proportional to the difference between left detected signal and right detected signal, resulting in a two lobed beam pattern on the sky with 80′ beam separation. The double difference weights the secondary-centered data positively, while weighting the secondary-left and secondary-right data negatively. This gives a signal proportional to the difference between the center detected signal and the side detected signals. This produces a three lobed beam pattern on the sky, with 40′ beam separation (see Chapter 2, Figure 2-2). The single difference and double difference data are nearly statistically independent. Since *differences* are taken for the final signals, atmospheric offsets and, for the double difference, atmospheric gradients, are suppressed.

The second level of modulation is a telescope scan in cross-elevation with peak-to-peak amplitude of 1.°5 and a 1-minute period, as shown in the second and third panels of Fig. 3-3. Cross-elevation is the direction locally perpendicular to elevation. The scan center is tracked on the sky during this motion. A region of the sky is observed for the maximum amount of time without substantially varying the telescope elevation. To achieve this, observations are performed near the meridian. The telescope tracks the center-point of the scan beginning 10 minutes prior to upper culmination, and follows it for 20 minutes (i.e., symmetrically about transit, the point of maximum elevation for a point on the sky). During this time, sky rotation moves the point $\sim 40'$ westward.

At the end of each 20-minute scan, the telescope pauses for the star camera to

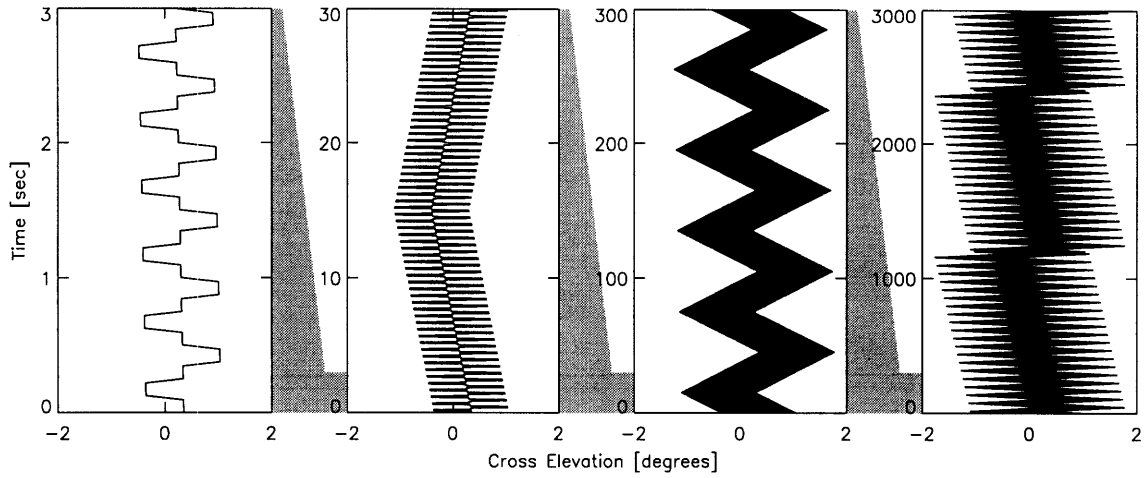

Figure 3-3: CMBR Observation Strategy. The four panels illustrate the various levels of modulation of the sky signal. The leftmost panel shows the secondary mirror chopper motion, the next two show the scanning of the gondola, and the final panel shows the effect of Earth rotation. Each panel shows a time scale, expanded by a factor of 10 (as indicated by the shading between the panels) from the following panel.

obtain a new absolute pointing image, and then steps $\sim$ 40′ to the east to position itself for the subsequent scan. Since each scan is 1°.5 in length, adjacent scans overlap by $\sim$ 50%; these overlapping scans provide the third and final level of modulation for the experiment, and nominally distribute the signal from each point on the sky across 40 minutes in time. This is illustrated in the last panel of Fig. 3-3.

The goal in the 1994 flight was to observe the identical sky observed in the 1992 flight. Fig. 3-4, which has been enlarged in declination relative to right ascension, shows the reconstructed weighted beam centers for the two flights. The declination during the 1994 flight was low by about 10′ . While this is not ideal, the separation is less than the beam size, permitting meaningful comparison between the two flights. Unfortunately difficulties in receiving commands in-flight prevented 1994 observations between roughly 14.4^h to 15.3^h of right ascension, thus missing the largest signal region of the 1992 flight.

Both 1992 and 1994 have a gap in CMBR observations at roughly 17^h right ascension. This corresponds to the MSAM1-92 observations of the Coma cluster, and the MSAM1-94 observations of Jupiter. This break in the observations requires the data be divided into "Sections 1 and 2" for later analyses. For the 1992 flight, the observed region for CMBR covered from right ascension $14^h.44$ to $16^h.89$, and from $17^h.18$ to $20^h.33$ (J1992.5). The 1994 flight observed the CMBR from right ascension

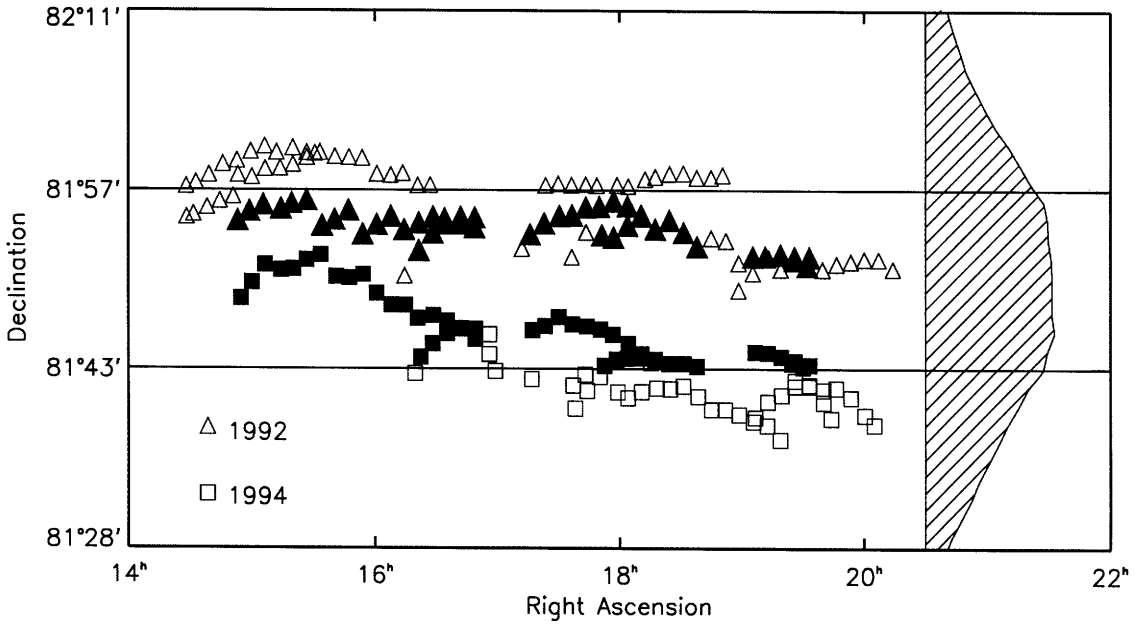

Figure 3-4: The sky coverage for MSAM1-92 and MSAM1-94 are shown above. The open symbols show the beam centers for the 1992 and 1994 flights as derived from the sky binning procedure. The triangles mark the 1992 centers and the squares mark the 1994 centers. The filled symbols are the beam centers for the bins used in the comparison. The horizontal lines indicate the bin boundaries in declination. The beam size is indicated by the hatched region on the side of the plot. Here the beam response versus declination is plotted.

$15^h.27$ to $16^h.84$, and from $17^h.57$ to $19^h.71$. The comparison uses 50% of the data from the two flights. Approximately 3.8 hours were spent engaged in CMBR observations.

Chapter 4

Data Reduction

Data reduction is the process of recovering binned sky power from the time stream of the detector signals. The "94 main analysis" is the reduction carried out for the 1994 data [Cheng et al., 1996], while the "92 main analysis" is that for the 1992 data [Cheng, 1994]. The "92 reanalysis" and "94 reanalysis" are new data reductions for the 1992 and 1994 flights, respectively. These "reanalysises" were done in a consistent way similar to the 94 main analysis, to facilitate the comparison. First, the details for the 94 main analysis will be presented, inserting along the way detailed differences in the 94 reanalysis. Then the detailed differences specific to the 92 reanalysis will be presented.

4.1 1994 Flight Data Reduction

Data reduction starts from an archive containing the radiometer telemetry stream, augmented with pointing information from the gondola telemetry stream and derived quantities. The quantity of interest is the integral of the sky brightness weighted by the beam response function of the telescope. In practice, the power emitted by the telescope optics and the power that leaks in through sidelobe response also contribute to the detected signal. Also ideally, the detected signal is nearly the same when the secondary is in the center, left or right positions ("center beam", "left beam", or "right beam"). For MSAM1 this is not the case: there is a systematic offset in the measured differences between the center, right and left beam data, which must be removed. Once this stable offset is subtracted, the signal stream is dominated by noise and events which are likely to be cosmic rays hitting the detectors. First, these cosmic ray events are modeled and subtracted. Then the time stream from each frequency channel is fit to a model consisting of modulated sky signal plus an instrument offset drift. The results of this linear fit are signal amplitudes for each binned position on

the sky ("sky bin") with their associated covariances. These data are fit with a two component spectral model consisting of CMBR anisotropy and emission from warm Galactic dust to recover the CMBR anisotropy. This process is described in more detail below.

4.1.1 Deglitching

The detector signals contain spikes, or "glitches," at a rate of ~ 1 every 3 seconds, consistent with the hypothesis that they are due to cosmic rays striking the detectors [Charakhch'yan et al., 1978]. Cosmic rays deliver energy to the detectors essentially instantly, acting as a delta function power input. The input power must be multiplied by the small signal voltage responsivity, $S(\omega)$ (Volts/Watt), to get the detected voltage, where $\omega = 2\pi f$ is angular frequency. $S(\omega)$ is a function of the detector thermal time constant, τ, which must be measured from the in-flight data. The detected signal at the output of the signal chain (point C on Figure 2-7) is a convolution of the input voltage and the electronic transfer function of the signal chain. The response to a cosmic ray event then is either 1) the temporal response of $S(\omega)$ times the time response of the signal electronics if the cosmic ray energy is deposited on the bolometer, or 2) just the temporal response of the signal electronics, if the energy is deposited in something with a frequency independent voltage responsivity. An example of two cosmic ray events in the signal stream is shown in Figure 4-1. The second event shown is consistent with the energy being deposited in the bolometer, a category labeled "Type 1". The effect of the detector thermal time constant is seen in the response to this event. A "Type 2" event is shown earlier in the signal stream, which is consistent with just the time response of the signal train. These Type 2 events are likely due to upsets in the front-end electronics, possibly due to cosmic rays striking the JFETs.

Cosmic rays are removed by fitting the data to the impulse response function of the detector/amplifier/filter chain. The τ in $S(\omega)$ is found by fitting about 400 medium sized Type 1 glitches in the signal stream to the model,

$$G(t) = \text{Amplitude} \times FT^{-1}((S(\omega) \times A(\omega) \times I(\omega)), \tag{4.1}$$

where t is time, FT is the Fourier Transform, $A(\omega)$ is the measured analog transfer function versus frequency, and $I(\omega)$ is the frequency response of the integrating filter sampled at 32 Hz, $I(\omega) = 64/\omega \times \sin(\omega/64)$. The τ which minimizes the total $\chi^2$for all 400 fits is then used in $G(t)$ to model all the events in the signal stream.

Fitting and removing spikes, "deglitching," requires an estimate of the noise. A

accurate estimate of the noise can't be made until the spikes have been removed, so a naive estimate is used. To do this, the offset subtracted signal stream is assumed to have random noise. Throughout this work "offset subtracted" means that the average signal in the center, left and right beams over the flight has been removed from the signal stream. A histogram of all the offset subtracted signals are fit to a Gaussian, and the fitted Gaussian width is used to approximate the rms. This estimate is slightly better than the raw rms, because it is less susceptible to the tails of the distribution. This rms is used to estimate the standard deviation, σ, in the following discussion. A better estimate will be made once deglitching is complete.

Candidate spike locations are identified using a $1.5\,\sigma$ threshold on the offset subtracted signal stream. The data within 1 second of a spike are fit to a model of the response function. A fraction of the spikes require a second spike 0.06–0.31 seconds (2–10 detector signal samples) separated from the first to be added to the fit; these are reported as "Doubles" in Table 4.1. If the resulting spike amplitude has less than $3\,\sigma$ significance (i.e., the amplitude of the glitch divided by the formal fit error on that amplitude is less than 3), the signal stream is not modified. If the spike amplitude has more than $3\,\sigma$ significance, then the quality of the fit is considered. The criterion for a good fit corresponded to a χ^2 / DOF of roughly 1.5. If the fit is good, the spike template is subtracted from the signal stream. If the fit is poor, full data records (64 samples, or 2 sec) before and after the spike are deleted; this removes about 6% of the data ("Lost" quoted in Table 4.1). The number of glitches subtracted of both Type 1 and 2 are given in Table 4.1. About 1 % of the degrees of freedom in the data were used to fit the glitches. Either positive or negative amplitudes are allowed in the fit; in channels 1, 2, and 3 $\sim$ 90% of the Type 1 spikes have positive amplitude consistent with the cosmic ray hypothesis. The 10% that are negative is probably an indication of contamination to the deglitching process from noise. In channel 4 there are an equal number of positive and negative amplitude Type 1 glitches, implying more significant contamination to the deglitching process by random noise; however, since the number of degrees of freedom affected is small (less than 1 percent) and the spikes appear random, this contamination is ignored. The Type 2 glitches are most probably due to cosmic rays striking either the gate of the JFET in the internal preamplifier, or one of the gates of dual JFET in the external preamplifier. This possibility, as well as the rate and energy spectrum of the fit glitches are discussed in Appendix D. The signal stream after cosmic ray subtraction is shown as the second panel in Figure 4-1, where the average radiometric offset has been removed. The results of the deglitching process are shown in Table 4.1. The "Initial Number of Samples" is the total number of data points used in the data reduction, before any cutting. An electrical anomaly

in channel 4 resulted in a slightly smaller initial sample.

Channel	1	2	3	4
Initial Number of Samples	504256	504256	504256	488640
Doubles	4.6%	4.8%	3.8%	4.8%
Number of Type 1 Glitches	4237	5545	2399	3789
positive amplitude	88%	93%	96%	45%
Number of Type 2 Glitches	1028	1129	1308	1032
positive amplitude	93%	87%	72%	49%
Lost	5.7%	6.4%	6.1%	0.3%

Table 4.1: Summary of Deglitching Results.

4.1.2 Demodulation and Beam Maps

As described in Chapter 3, the experiment provides 3 levels of sky signal modulation. The first level comes from the 2 Hz secondary mirror motion, reproduced in the third panel of Figure 4-2 . The absolute brightness of the sky is not measured by this experiment, but rather the brightness difference in patches of sky separated by a set distance. Linear combinations, "templates," of the detector signals are constructed to give difference signals with well defined nearly orthogonal antenna patterns on the sky. The motion of the secondary (center, right, center, left) provides two sky difference signals, the single difference and double difference. The single difference signal is proportional to the difference between the power input to the left and right beams, and, naively, can be obtained by multiplying the secondary-left data by 1 and the secondary-right data by -1 and summing, while ignoring the secondary-center data. The naive "demodulation template" is shown in Figure 4-2 as a vector containing 1's, -1's and zeros corresponding to when the secondary mirror is in the left, right and center positions. In addition, a double difference signal, proportional to the difference between the power in the center-beam, and that in the side beams, can be obtained by multiplying the secondary-center signals by 1 and the secondary-right and left signals by -1, also shown in Figure 4-2.

The naive templates are not ideal for two reasons. First, the times at which the integrated samples are read by the data acquisition system is fixed relative to

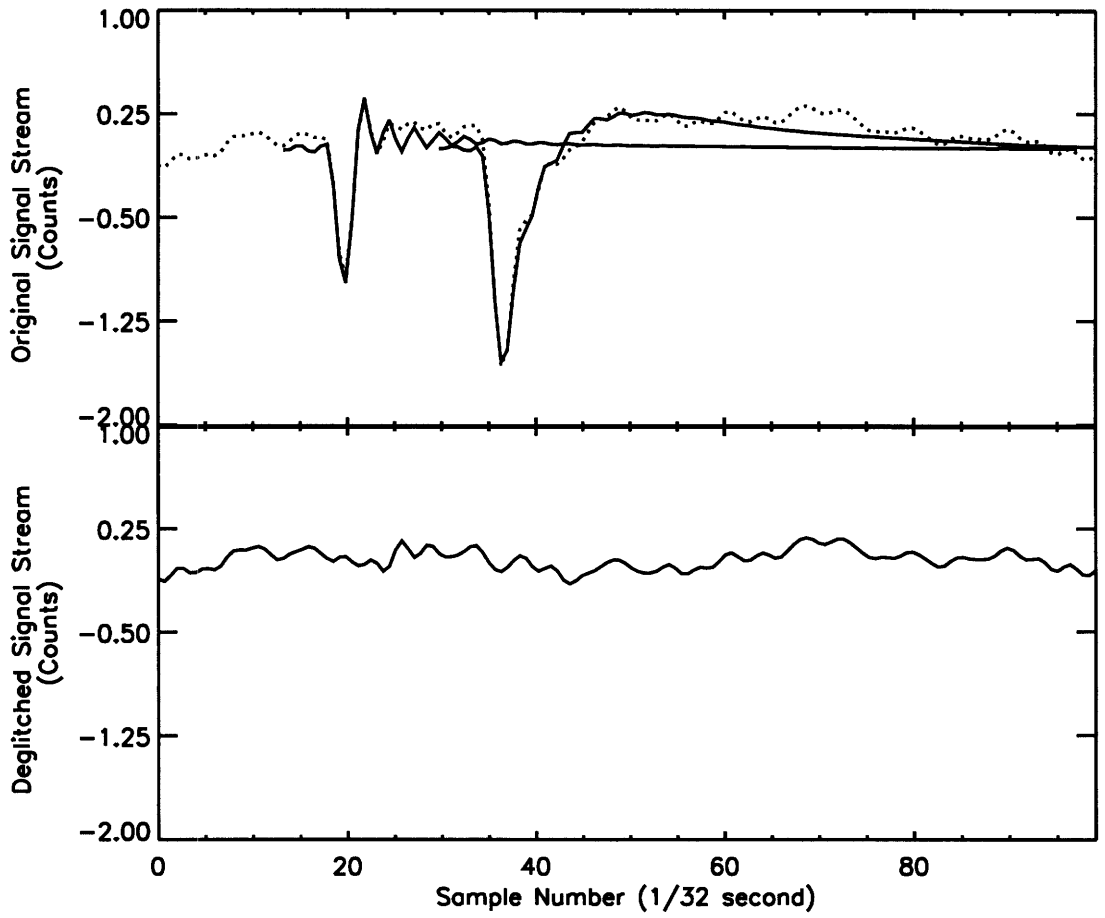

Figure 4-1: The first panel shows examples of the two types of "glitches" seen in the signal stream. The spikes appear negative because positive power impulses to the detector cause the bolometer resistance to decrease, thereby decreasing the voltage across the detector. The dotted line is the original time stream. The solid lines overlayed are the cosmic ray fits. The second panel shows the signal stream after the cosmic rays have been removed.

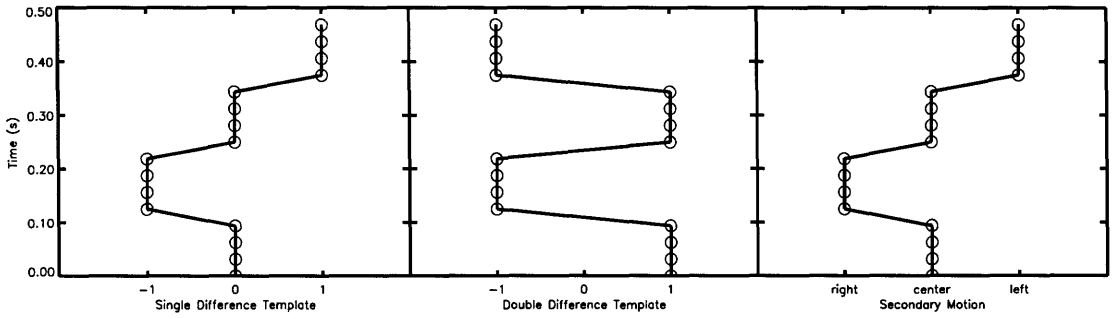

Figure 4-2: The naive demodulation templates are shown as well as the secondary chopper position versus time. For the single difference template, the secondary-center data are ignored (weighted by zero), the secondary-left data are multiplied by 1 and the secondary-right data are multiplied by -1. For the double difference template, the secondary-center data are multiplied by 1, while the secondary-right and left data are multiplied by -1. The symbols mark the time separation of the 16 A/D samples in the 1/2 second cycle of the secondary chopper.

the chopper movement, but not known. The correct phasing of the template must be determined from the data. Also the naive demodulations are effectively square waves with power at the principle frequency, and all the odd harmonics. The single difference template has power at $2, 6, 10, 14, \ldots$ Hz, and the double difference template has power at $4, 12, \ldots$ Hz. However, the signal electronics effectively roll-off signal at frequencies above 8 Hz, so signal-to-noise is not improved by keeping higher frequency components of the difference templates.

The data from a scan over Jupiter, which has 5 passes over the planet, are used to adjust the naive templates, creating a better set of demodulation templates, d_k^D for the double difference and d_k^S for the single difference [Puchalla, 1995]. The templates used for the analysis are shown in Figure 4-3.

The antenna pattern, or "beam map," is the response of the instrument to power from the sky as a function of angular position relative to the optical axis of the telescope. The beam maps are used later to integrate over models of sky brightness, for both the CMBR and the thermal emission from Galactic dust. To determine the beam maps for the difference signals, the data taken when rastering over Jupiter are used, because Jupiter is nearly a point source in our beam. The detector signal stream, S_i (where i indexes the time-ordered A/D samples), can be rearranged as S_{jk}, where $j = 1, \ldots 16$ and $k = 1, \ldots N_{\text{cycles}}$, so that $i = 16k + j$. The difference signals are produced by demodulating the detector signal stream. A "demodulated data point", t_k, is obtained for each cycle k by evaluating the inner product of the

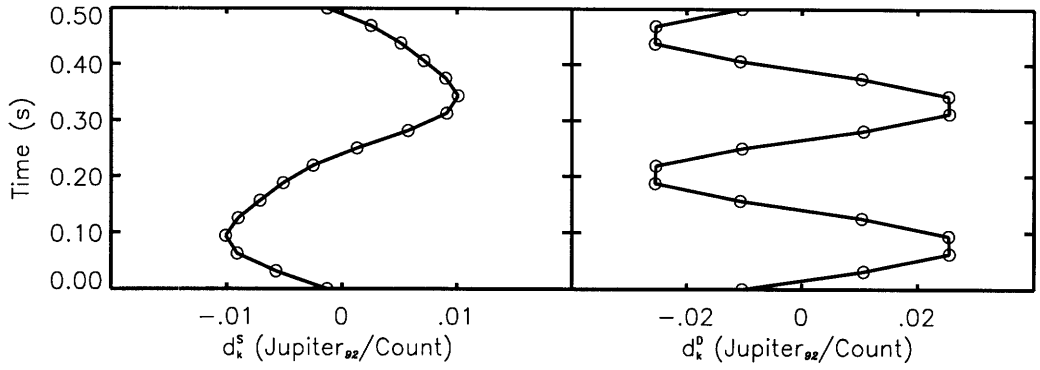

Figure 4-3: The final demodulation vectors, d_k^S for the single difference and d_k^D for the double difference. These are for channel 1; the other channels are similar. The normalization is chosen so that the flux density of Jupiter as observed on 1992 June 5 is defined to be 1.0 in the central lobe of the double difference and 1.0 in the difference between the left and right lobes in the single difference.

signal stream, S_{jk}, with one of two demodulation templates, d_j,

$$t_k = \sum_j d_j S_{jk}. \tag{4.2}$$

The demodulated data at each point in cross-elevation in each horizontal scan in the raster are fit to a cubic spline in cross-elevation. The spline has a maximum of 27 knots, with more knots grouped in the high response regions of the beam map. These splines in cross-elevation are interpolated to 1.′5 centers. Then splines, again on 1.′5 centers, in the elevation direction are used to interpolate between the scan elevations of the raster. The binning is very fine to minimize the loss of any real information in the beam. Typical resulting beam maps are shown in Chapter 2, Figure 2-2. The single difference beam map is a two lobed pattern on the sky with 80′ separation between lobes. The double difference beam map is a three lobed pattern on the sky, with 40′ separation between lobes. The single difference maps are normalized such that the difference in the average peak height of the two lobes is 1. The double difference maps are normalized such that the average peak height of the central lobe is 1.

4.1.3 Calibration

The raster over Jupiter provides more than just the shape of the antenna pattern. The full disk brightness temperatures of Jupiter for the four spectral channels are $T_{\rm RJ} = 172, 170, 148$, and 148 K, derived from ground-based measurements [Griffin et al., 1986]. Using these, together with the apparent size of Jupiter at the time of observation, $\Omega_{Jupiter}$, gives the spectral flux density of Jupiter,

$$S_\nu = \frac{k_{\rm B} T_{\rm RJ} \nu_{\rm eff}^2}{c^2} \Omega_{\rm Jupiter}, \tag{4.3}$$

where $k_{\rm B}$ is Boltzmann's constant, $\nu_{\rm eff}$ is the effective frequency for each channel given in Chapter 2, and c is the speed of light. This provide an absolute calibration of the instrument. There is a 10% systematic uncertainty in the calibration of the instrument, due to uncertainty in the above brightness temperature. This uncertainty does not affect the comparison between MSAM1-92 and MSAM1-94, since Jupiter was used to calibrate the instrument for both flights.

The primary calibration unit for MSAM1 is spectral flux density (W/m^2 Hz), or equivalently, Kelvin $\times$ steradian. Dividing by the effective beamsize for the four channels, $\Omega_{\rm beam} = 5.5, 5.8, 6.0$ and 5.8×10^{-5} steradian, converts the demodulated data into brightness units (W/m^2 sr Hz), or equivalently Raleigh Jeans temperature units ($K_{\rm RJ}$). In Section 4.1.8, it will be useful to express the demodulated data in units of W/m^2 sr; these are obtained by multiplying the brightness by the effective Raleigh Jeans bandwidth, 1.3, 2.3, 1.9, 1.3 cm^{-1}.

4.1.4 Understanding Noise

It is important to estimate the noise in the data. This way the χ^2 statistic can be used to determine the quality of a fit. The offset subtracted signal stream, S_i, is assumed to have random noise which can be described by a covariance matrix $V_{ij}^S = \langle S_i S_j \rangle$. The finite frequency response of the detectors, together with phase shifts in the signal electronics correlate the data.

The noise is assumed to be stationary over 20 minute periods. That is

$$V_{i,j=i+n}^S = \langle S_i S_{i+n} \rangle = {\rm Corr}(S,S)_n, \tag{4.4}$$

where ${\rm Corr}(S,S)_n$ is the autocorrelation of the offset subtracted signal stream, evaluated at lag n. The autocorrelation of the signal is equal to the Fourier transform (FFT) of the power spectrum of the noise (the Weiner-Khinchin theorem) [Press et al., 1992]. An average power spectrum is found for all continuous 16 second

portions of data. These are then averaged, and a Fourier Transform is done to obtain an autocorrelation vector. The power spectra were obtained from data after removing the model, M_i, of drift and sky signal fit using uniform errors (described below), ie.

$$\mathrm{Corr}(S,S) \sim FFT^{-1}(\langle |FFT(S_i - M_i)|^2 \rangle_{20\ \mathrm{minutes}}), \tag{4.5}$$

The variance on the demodulated data is then,

$$V_{ij}^T = \sum_{jk} d_j d_k V_{j,k=j+n}^S, \tag{4.6}$$

where d_j are the demodulation vectors, and n is correlation length. Since these estimates come from the residuals of the M_i fit, they do not permit an independent goodness-of-fit test; however they can reliably be used as a noise estimate for later analysis steps. For the 1994 reanalysis (described in Section 4.2), the noise is estimated prior to the fit, eliminating this restriction.

4.1.5 Simultaneous Drift Removal and Sky Binning

To obtain a measure of signal on the sky, the demodulated data are fit to a set of functions representing bins on the sky, $B_{\beta i}$, slowly varying functions of time $K_{\kappa i}$, and measured monitor signals, $P_{\rho i}$, which are combined into a single design matrix, $H_{\alpha i}$. Unlike the deglitching and noise estimation steps of the analysis, the offset is left in the demodulated data for this fit. The model for the data is M_i:

$$M_i = \sum_\alpha a_\alpha H_{\alpha i} = \sum_\beta a_\beta B_{\beta i} + \sum_\kappa a_\kappa K_{\kappa i}(k) + \sum_\rho a_\rho P_{\rho i}, \tag{4.7}$$

where the a's are the free parameters of the model. $B_{\beta i}$ is formed by determining pointing, $\vec{\Theta}_i$, for each time, i. Square bins are chosen with $0^h.057$ width in right ascension and $0^\circ.12$ width in declination and 10° in "twist", where twist is the angular orientation of the secondary chopper axis with respect 0^h RA. $B_{\beta i}$ is the matrix representation of this binning, with β running over the number of bins, making a_β the binned data values.

$$B_{\beta i} = \begin{cases} 1 & \text{if } \vec{\Theta}_i \in \text{ bin}_\beta \\ 0 & \text{otherwise ,} \end{cases} \tag{4.8}$$

$K_{\kappa i}(k)$ are cubic splines, with knot spacing of k. Lastly, $P_{\rho i}$ is a matrix of various measured quantities on the instrument which correlate with the offset: air pressure and the pitch and roll of the gondola outer frame. The average value is removed from $K_{\kappa i}$ and $P_{\rho i}$ so that the average offset is left in the binned data. The solution to this

linear fit is:

$$a_\alpha = \sum_{ij\gamma km} (H_{\alpha i} W_{ij} H_{j\gamma})^{-1} H_{\gamma k} W_{km} t_m, \tag{4.9}$$

where W_{ij} is the weight matrix of the demodulated data, $V_{ij}^{T^{-1}}$. The covariance of the fit parameters is given by :

$$\mathrm{Var}(a_\alpha) = V^A_{\alpha\gamma} = \sum_{ij} (H_{\alpha i} W_{ij} H_{j\gamma})^{-1} \tag{4.10}$$

χ^2 for the fit is:

$$\chi^2 = \sum_{ij} (t_i - \sum_\alpha a_\alpha H_{\alpha i}) W_{ij} (t_j - \sum_\beta a_\beta H_{\beta j}) \tag{4.11}$$

The binned data, a_β, have a covariance given by the upper β by β quadrant of $V^A_{\alpha\gamma}$. χ^2 of the fits are given in Table 4.2.

The offset drifts are modeled with $K_{\kappa i}(k)$, a cubic spline with knots every 12 minutes (2.5 minutes for the 16.5 cm^{-1} channel), and $P_{\rho i}$, the gondola inclination, roll, and air pressure. The fitted drifts, $\sum_\kappa a_\kappa K_{\kappa i}(k) + \sum_\rho a_\rho P_{\rho i}$, are described in detail in Appendix F. The drifts are all on time scales from 5 - 15 minutes, placing them well away from the time scale of the telescope scans ($\sim$ 1 minute).

The simultaneous fit of long-term drift and sky signal ensures that this drift removal does not bias our observations of the sky. This fit is done separately for each channel, section and demodulation of the flight. The resulting sky signals have bin-to-bin correlation, and we propagate a full covariance matrix through the remainder of the analysis. Sky bins containing less than 4 s of integration are deleted. An example of raw demodulated data, fitted drift signal ($\sum_\kappa a_\kappa K_{\kappa i}(k) + \sum_\rho a_\rho P_{\rho i}$), and fitted sky signal ($a_\beta B_{\beta i}$) for channel 1 for the double difference data set are shown in Fig.4-4.

Channel	1 (χ^2 / DOF)	2 (χ^2 / DOF)	3 (χ^2 / DOF)	4 (χ^2 / DOF)
Single Difference	6027/5640	5820/5540	6760/5770	6160/5944
Double Difference	5870/5640	5800/5540	6310/5770	6530/5944

Table 4.2: χ^2 for 1994 Analysis Bin And Drift Fit

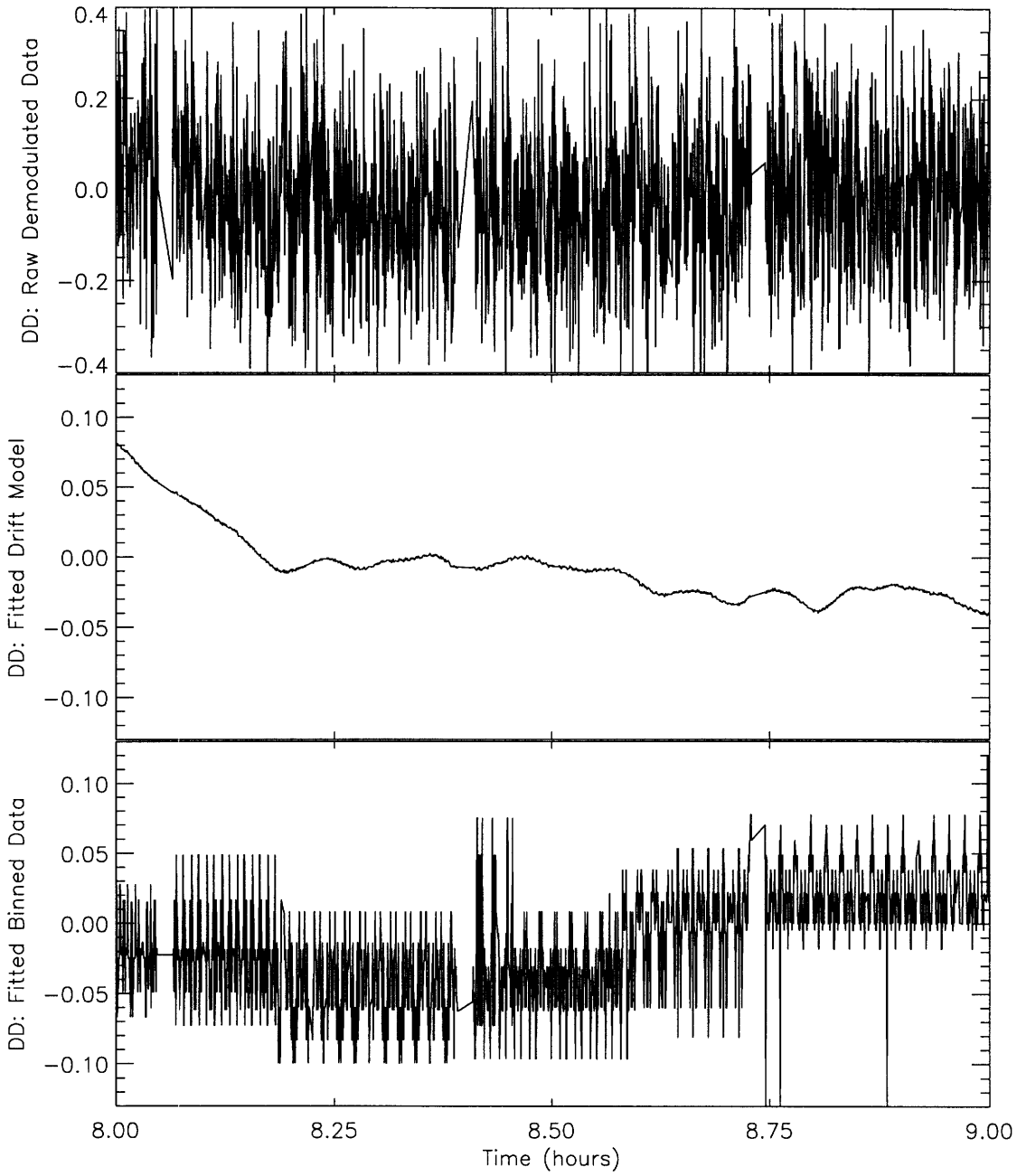

Figure 4-4: Double difference data, fitted drift ($\sum_\kappa a_\kappa K_{\kappa i}(k) + \sum_\rho a_\rho P_{\rho i}$) and fitted binned sky signal ($\sum_\beta a_\beta B_{\beta i}$) versus time are shown. The sum of the lower two panels is the complete model, M_i, for the data shown in the upper panel. Gaps at $\sim$ 8.1, 8.4, and 8.75 correspond to pauses for star camera exposures. The high frequency structure in the lower panel shows the effect of scanning the telescope across the sky bins with a 1 minute period. The amplitudes are in $\mathrm{mK_{RJ}}$. The y-axis for the lower two plots are 1/3 the size of the y-axis for the upper plot.

4.1.6 1994 Internal Consistency Check : $rt-lt$

A check for systematic effects in the data is to divide it into two independent parts which should be measuring the same sky signal and compare them. One such segmentation can be done by considering the direction the gondola was moving as an additional parameter in the binning. Now dividing this data into set rt (bins with gondola moving to the right) and set lt (bins with gondola moving to the left), $rt+lt$ is formed by averaging (summing and dividing by 2) the two sets and removing a weighted average. $rt-lt$ is formed by differencing the two sets, dividing by 2, and removing a weighted average. The χ^2 and degrees of freedom (DOF) for $rt-lt$ and $rt+lt$ datasets for the 1994 data are given in Table 4.3.

A Kolmogorov-Smirnov (KS) test [Press et al., 1992] of the $rt-lt$ probabilities gives a .29 probability that these eight probabilities are drawn from a uniform distribution from 0 to 1. Based on this, we conclude that the $rt-lt$ data in both the single and double difference demodulations for all channels are consistent with no signal, and that the error estimates are reasonable.

A KS test of the $rt+lt$ probabilities gives a 1×10^{-3} probability that they are drawn from a uniform distribution from 0 to 1. The χ^2 probabilities show significant signal in channels 1 and 3. The signal in channel 2 is marginally significant, and channel 4 is consistent with noise.

		Double Difference		Single Difference	
Channel	Data Set	χ^2 /DOF	P	χ^2 /DOF	P
1	$rt-lt$	196 / 201	0.59	195 / 201	0.61
	$rt+lt$	289 / 201	4×10^{-5}	267 / 201	1×10^{-3}
2	$rt-lt$	201 / 201	0.49	190 / 201	0.70
	$rt+lt$	243 / 201	0.02	233 / 201	0.06
3	$rt-lt$	201 / 202	0.51	179 / 202	0.88
	$rt+lt$	335 / 202	1×10^{-8}	355 / 202	2×10^{-10}
4	$rt-lt$	208 / 203	0.39	234 / 203	0.07
	$rt+lt$	202 / 203	0.51	235 / 203	0.06

Table 4.3: Comparison of Right and Left Going Data : 1994 Analysis

4.1.7 Offset Amplitude

Offsets correspond to measured differences in input power to the center, right and left beam. There is an offset in the binned data, the amplitude of which is given in Table 4.4 for each channel and demodulation for the 1994 flight. The offsets are quite stable, and between 1 and 6 mK in the four channels. These offsets are lower than the ~ 10 mK offsets in 1992 [Cheng et al., 1994]. The offset in *rt−lt* is less than 10 μK, and is consistent with zero. The fact that the instrument has no significant right/left asymmetry justifies the use of all the data together for the main analysis.

Channel	1	2	3	4
Average Offset				
Double Difference (mK)	6.0	4.6	2.8	5.8
Single Difference (mK)	5.7	3.2	1.7	1.3
rt−lt Offset				
Double Difference (μK)	1.8 ± 5.0	-1.9 ± 1.9	-0.8 ± 0.5	-4.1 ± 4.2
Single Difference (μK)	-4.2 ± 5.5	-0.1 ± 1.5	-0.7 ± 0.5	4.1 ± 5.4

Table 4.4: Summary of Offsets : 1994 Analysis. The low *rt−lt* offsets imply that there are no significant right/left systematic effects in the data.

4.1.8 Decomposition into Dust + CMBR

To extract the part of the signal due to variations in the CMBR, we fit the data t_{ck} for each channel c and sky bin k to a two component spectral model:

$$t_{ck} = \int d\nu\, F_c(\nu) \left[D_k \left(\frac{\nu}{\nu_0}\right)^{\alpha} B_\nu(T_{\rm D}) + M_k \left.\frac{dB_\nu}{dT}\right|_{T_{\rm CMBR}} \right], \tag{4.12}$$

where t_{ck} is the demodulated data in units of W/m^2 sr (see Section 4.1.3), $F_c(\nu)$ is the spectral response of the instrument, $B_\nu(T)$ is the Planck function at temperature T, $T_{\rm D} = 20$ K is the dust temperature, $\alpha = 1.5$ is the spectral index of the dust, $\nu_0 = 22.5$ cm^{-1} is the reference frequency, $T_{\rm CMBR} = 2.73$ K is the temperature of the CMBR [Fixsen et al., 1996b], and D_k and M_k are free parameters. The result of the fit is a component sensitive to the CMBR temperature difference (M_k) and a component sensitive to the dust gradient (D_k), with their associated covariance matrices, V_{jk}^M,

and V_{jk}^{D}.

Plots of the DUST component, M_k, and the CMBR component, D_k, are shown in Fig. 4-5 and 4-6 for the 1994 data set. The plot is has had the largest eigenmode of the covariance matrix removed from the data (for further information see Appendix. G). Also for clarity, the data have also been binned more coarsely than for the analysis.

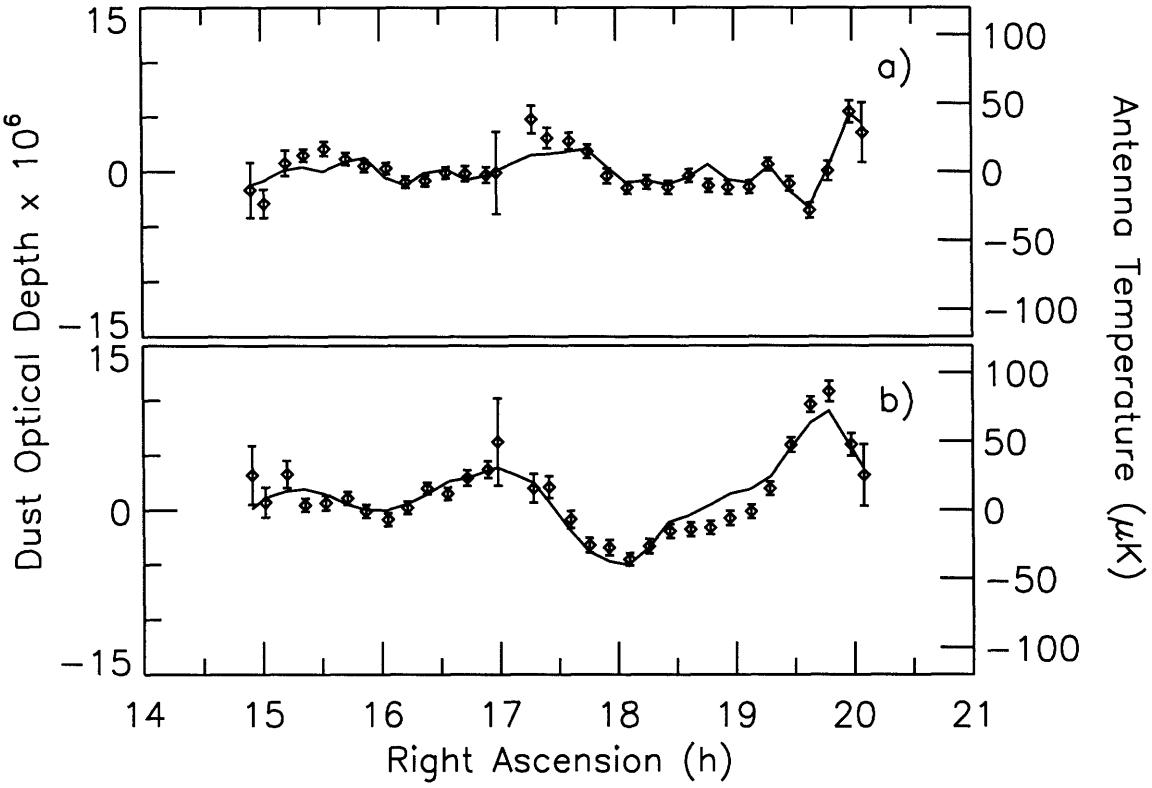

Figure 4-5: Dust optical depth times 10^6 at 22.5 cm^{-1}. The overlayed solid line shows the dust signal expected from integrating the beam pattern over the IRAS 100 μm data, scaled in overall amplitude to our measurements. The double difference results are shown in a), while those for the single difference are shown in b).

4.1.9 Cut Summary

A cut summary for the 1994 analysis is shown in Table 4.5. "Electrical" is the cut due to an electrical anomaly, and only affects channel 4. As discussed in Section 4.1.1, some data are removed which have large amplitude poorly fitting glitches; "Deglitching" is the amount of data lost when cutting out these glitches. "Full Records" is the

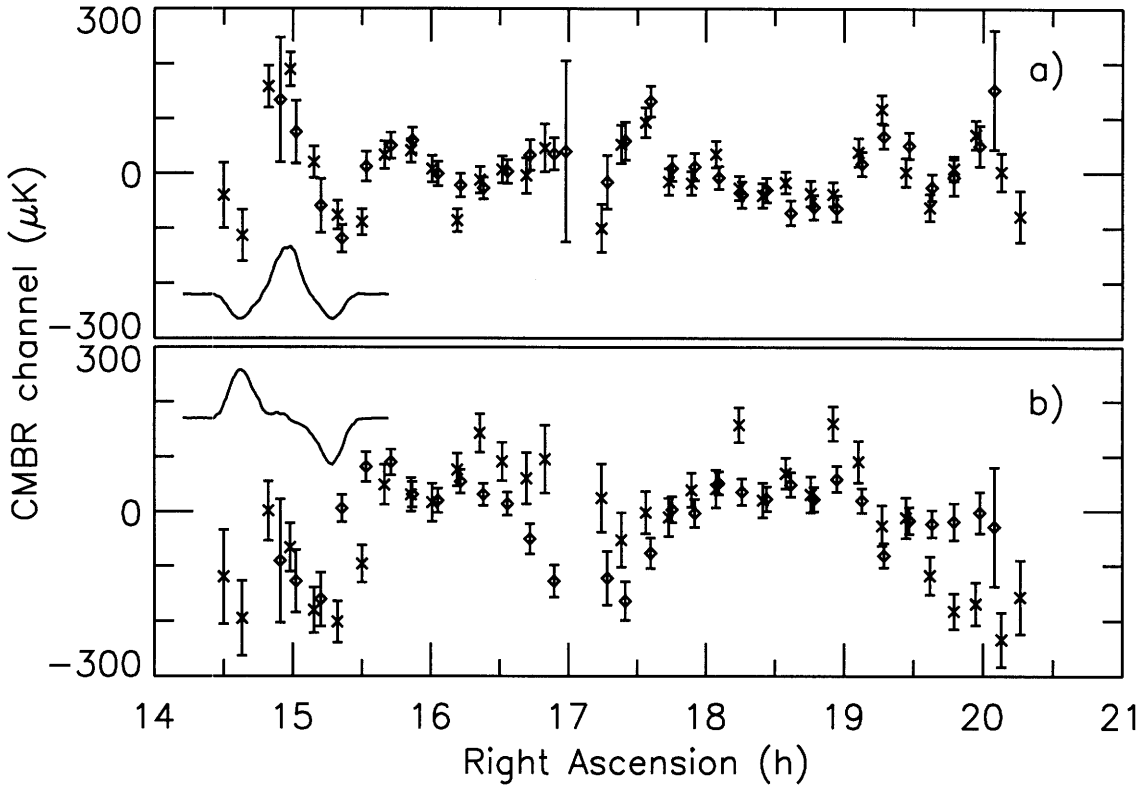

Figure 4-6: CMBR Component for the a) double difference and b) single difference data sets. The diamond shaped symbols show the 1994 main analysis results. Overlayed are x symbols showing the 1992 main analysis results. The central cut through the beam pattern is overlayed for comparison.

additional loss due to cutting out the full record, 64 samples, around these glitches. At one point during the CMBR observations, a commanding failure caused the telescope to scan erroneously. "Pointing" refers to the data cut during this time. The fit to the model consisting of sky bins and drifts in time relies on the bin bases being non-degenerate with the drift bases. This condition is not well satisfied when the telescope is stationary for the star camera exposures, so "StarCam Exp" of data are cut prior to performing the fit. Finally, the requirement of 4 seconds of integrated data in a bin leads to the very small "Min Bin Occ" cut.

cut	Channel 1	Channel 2	Channel 3	Channel 4
Before Cuts:	3.77 hr	3.77 hr	3.77 hr	3.77 hr
Electrical:	0 hr (0)	0 hr (0)	0 hr (0)	−0.09 hr (2.4%)
Deglitching:	−0.20 hr (5.3%)	−0.24 hr (6.3%)	−0.10 hr (2.7%)	−0.01 hr (0.3%)
Full Records:	−0.08 hr (2.2%)	−0.11 hr (3.0%)	−0.07 hr (2.0%)	−0.01 hr (0.2%)
Pointing:	−0.06 hr (1.6%)	−0.07 hr (1.8%)	−0.06 hr (1.7%)	−0.07 hr (1.9%)
StarCam Exp:	−0.16 hr (4.1%)	−0.14 hr (3.7%)	−0.14 hr (3.8%)	−0.16 hr (4.1%)
Min Bin Occ:	−0.00 hr (0.1%)	−0.00 hr (0.1%)	−0.00 hr (0.1%)	−0.00 hr (0.1%)
Total Cut:	−0.50 hr (13.3%)	−0.56 hr (14.8%)	−0.39 hr (10.3%)	−0.33 hr (8.8%)
After Cuts:	3.27 hr (86.7%)	3.22 hr (85.2%)	3.39 hr (89.7%)	3.44 hr (91.2%)

Table 4.5: Cut Summary for 1994 main analysis

4.2 1994 Reanalysis

A reanalysis of the data from MSAM1-94 was performed to facilitate the comparison to the MSAM1-92 results. This was very similar to the main 1994 analysis, except in the following details.

In the main analysis, the noise was estimated by measuring the autocorrelation of the offset-subtracted signal stream after removing the fit to a model composed of sky signals and time drifts. Motivated by the desire for a noise estimate prior to this fit, a new noise estimate is made based on fluctuations in the demodulated data. For this, the noise on the demodulated data, n_i, is assumed to be describable by a covariance matrix,

$$V_{ij}^T = \langle n_i n_j \rangle. \tag{4.13}$$

where i is now an index for a full 2 seconds of demodulated data. Because the detector and electronic correlations are all substantially shorter than 2 seconds, it is reasonable to approximate V_{ij}^T by a vector of diagonal variances, V_i^T.

The $\langle n_i n_i \rangle$ is estimated from the rms in each minute of demodulated data,

$$V_M^T = \langle (t_i - \bar{t})^2 \rangle_{\text{1 minute}}, \tag{4.14}$$

where $\bar{t}$ is the average of the demodulated data over that minute. This has the advantage of not depending on the stationary nature of the noise over longer periods, and being insensitive to drifts on time scales longer than 1 minute. This estimate has the disadvantage of having relatively large uncertainty (12% given only 32 DOF), and of being slightly contaminated by signal. The uncertainty in the variance estimate, V, leads to a bias in the weight, V^{-1}, which in turn leads to high bias on χ^2/DOF. The one minute estimates are plotted versus time in Appendix E (Fig. E-1 - E-4). The estimates are fairly constant over the flight.

The average over the flight of these noise estimates are given in Table 4.6. Comparing these noise estimates to those used for the main 1994 analysis, also given in Table 4.6, one can see they are equivalent.

Estimate	Channel	1	2	3	4
			(μK$\sqrt{s}$)		
$V^T_{\langle \mathrm{Corr} \rangle}$	Double Difference	245	150	80	230
from average autocorrelation	Single Difference	252	130	75	355
V^T_M	Double Difference	240	150	85	230
from rms of 1 minute of data	Single Difference	255	130	85	350

Table 4.6: Summary of Noise Estimates

The fit to a model consisting of drifts in time and signals on the sky is repeated for the 1994 reanalysis. The reanalysis uses a 0.°24 bin size, double that used for the main analysis, which corresponds to the size of the central plateau of the main beam pattern. A 20° angular orientation bin size is used, also double that used previously. The χ^2 for the fit are given Table 4.7, where the noise estimates used are those described above.

The cuts made to the data for the 94 reanalysis were the same as those made for the main analysis, as shown in Table 4.5. The only difference is in the "Min Bin Occ" cut, which is made even smaller than in the main analysis due to the larger bin sizes used in the reanalysis.

Channel	1 (χ^2/DOF)	2 (χ^2/DOF)	3 (χ^2/DOF)	4 (χ^2/DOF)
Single Difference	5790/5700	5710/5600	5760/5910	6180/6000
Double Difference	5830/5700	5780/5600	5920/5910	6190/6000

Table 4.7: χ^2 for 1994 Re-analysis Bin And Drift Fit

4.3 1992 Reanalysis

The initial paper on the 1992 results [Cheng et al., 1994] neglects correlations in the binned data introduced by the removal of the drift. The 1992 data are reanalyzed to account for these correlations. The techniques used are basically the same as those used for the 1994 analysis, with the exception of the details listed below.

The deglitching procedure was different for the 1992 main analysis and is described in [Cheng et al., 1994]. For the reanalysis the deglitched, demodulated data from the original analysis are used.

The noise estimates for the data are made from the rms of 1 minute sections of data, as described in Section 4.2, and shown in Appendix E (Fig. E-5 - E-8). The 1992 noise estimates are considerably less uniform than those for the 1994 flight, possibly due to electrical problems or sidelobe pickup from the superstructure in 1992.

The fit to a model consisting of drifts in time and signals on the sky is repeated for the 1992 reanalysis. The bin size is the same as that for the 1994 reanalysis. The model used for the 1992 data did not include any physical monitors, just the bins and a spline with knots with every 2.5 minutes. This is similar to the drift model used in the 92 main analysis [Cheng et al., 1994]. The χ^2 for the fit are given Table 4.8.

The fitted drifts are shown in Appendix F. The drift has the same $\sim$ 5 minute time scale oscillatory nature, but does not scale in frequency like residual atmosphere (many hundreds of μK in channel 1).

The decomposition into CMBR and DUST is done as described for the 1994 main analysis.

4.3.1 1992 Internal Consistency Check : $rt-lt$

The MSAM1-92 data set is divided into set rt (bins with gondola moving to the right) and set lt (bins with gondola moving to the left). The χ^2 and degrees of freedom (DOF)

Channel	1 (χ^2/DOF)	2 (χ^2/DOF)	3 (χ^2/DOF)	4 (χ^2/DOF)
Single Difference	27781/27233	28069/27756	28962/28828	31399/31075
Double Difference	27474/27233	27954/27756	29033/28828	31281/31075

Table 4.8: χ^2 for 1992 Reanalysis Bin And Drift Fit

for the *rt−lt* and *rt+lt* datasets for the 1992 data are given in Table 4.9.

A KS test of the *rt−lt* probabilities gives a .38 probability that they are drawn from a uniform distribution from 0 to 1. Again, for the 1992 data, the *rt−lt* data are consistent with no signal, and that the error estimates are reasonable.

A KS test of the *rt+lt* probabilities gives a 7×10^{-3} probability that they are drawn from a uniform distribution from 0 to 1. The χ^2 probabilities show significant signal in channels 1,2 and 3. The signal in channel 4 is marginally significant. The 1992 *rt+lt* probabilities for channels 1 and 3 are likely more significant than those for 1994 (see Table 4.3) because there was deeper coverage of the high signal regions of sky in the 1992 flight than the 1994 flight.

		Double Difference		Single Difference	
Channel	Data Set	χ^2 /DOF	P	χ^2 /DOF	P
1	*rt−lt*	120 / 100	0.08	99 / 100	0.51
	rt+lt	253 / 100	3×10^{-15}	140 / 100	5×10^{-3}
2	*rt−lt*	123 / 101	0.07	112 / 101	0.21
	rt+lt	168 / 101	3×10^{-5}	108 / 101	0.30
3	*rt−lt*	72 / 100	0.98	133 / 100	0.02
	rt+lt	282 / 100	1×10^{-17}	221 / 100	3×10^{-11}
4	*rt−lt*	102 / 100	0.43	83 / 100	0.89
	rt+lt	115 / 100	0.14	126 / 100	0.04

Table 4.9: Comparison of Right and Left Going Data : 1992 Reanalysis

4.3.2 Cut Summary

A cut summary for 1992 reanalysis is shown in Table 4.10. For MSAM1-92, the data were deconvolved with a model of the electronic response function, which concentrated the glitches into 1-2 samples. There was nothing subtracted, these highly affected samples were simply cut. "Deglitching" is the amount of data lost when cutting out these glitches. "Full Cycles" is the additional loss due to cutting out the full chopper cycle, 16 samples, around these glitches. The fit to the model consisting of sky bins and drifts in time relies on the bin bases being non-degenerate with the drift bases. This condition is not well satisfied when the telescope is stationary for the star camera exposures, so "StarCam Exp" of data are cut prior to performing the fit. The requirement of 4 seconds of integrated data in a bin leads to a negligibly small loss of data, so is not reflected in the table.

cut	Channel 1	Channel 2	Channel 3	Channel 4
Before Cuts:	4.83 hr	4.83 hr	4.83 hr	4.83 hr
Deglitching:	−0.29 hr (6.0%)	−0.28 hr (5.8%)	−0.22 hr (4.5%)	−0.12 hr (2.4%)
Full Cycles:	−0.60 hr (12.4%)	−0.53 hr (11.0%)	−0.44 hr (9.1%)	−0.22 hr (4.6%)
StarCam Exp:	−0.12 hr (2.5%)	−0.13 hr (2.6%)	−0.13 hr (2.8%)	−0.15 hr (3.0%)
Total Cut:	−1.02 hr (21.0%)	−0.94 hr (19.5%)	−0.79 hr (16.4%)	−0.48 hr (10.0%)
After Cuts:	3.81 hr (79.0%)	3.89 hr (80.5%)	4.04 hr (83.6%)	4.35 hr (90.0%)

Table 4.10: Cut Summary for 1992 Reanalysis

Chapter 5

Results and Conclusions

The CMBR and DUST component signals are fit to emission models for these sources. There are no dust maps in these spectral bands, so the IRAS measurements from 100 μm are scaled using the Planck spectrum and a frequency dependent emissivity law to obtain the expected dust signal. For the CMBR, the measured signal is used to put limits on $\Delta T/T$. Finally, the signals measured by the 1994 flight are compared with those measured in 1992 to show that the two flights give the same results.

5.1 Comparison to IRAS Dust to 1994 Data

The expected signal from warm interstellar dust is computed by convolving the IRAS 100 μm Sky Survey Atlas [Wheelock et al., 1994] with both beam patterns. This signal is fit to the dust data; the χ^2 / DOF for the single difference fit is 310/210 and 262/210 for the double difference fit. The fit overlays the data in Fig. 4-5. It gives an average dust spectral index between our bands and 100 μm of $\alpha = 1.40 \pm 0.16$ assuming a dust temperature, T_D, of 20 K. The single and double differenced dust signals are reduced from the un-differenced values by roughly a factor 10. In the lowest frequency channel, the average dust contribution to sky signal is less than 2 μK.

5.2 Δ T /T results

Theory can only predict the *distribution* of temperature anisotropies, rather than specific magnitudes at locations on the sky. Thus the sky data can not be simply fit to a model for anisotropy. Instead, a model distribution is assumed, and a statistic is used to characterize both the measured data and simulated data which follows the

model distribution.

The assumed temperature distribution is that of a Gaussian random field described by a two-point correlation function

$$C(|\mathbf{x}_1 - \mathbf{x}_2|) = \langle \Delta T(\mathbf{x}_1)\, \Delta T(\mathbf{x}_2) \rangle = C_0 \exp(-\frac{1}{2}(\frac{\theta}{\theta_c})^2), \tag{5.1}$$

where $\mathbf{x}_1$ and $\mathbf{x}_2$ are positions on the sky, θ is the angle between them ($\mathbf{x}_1 \cdot \mathbf{x}_2 = \cos\theta$), and θ_c is the angle of peak sensitivity for a given beam pattern. The observations are binned on the sky in right ascension, declination and twist. Each of these observations can be thought to have its own beam pattern, B_i, at the i^{th} location on the sky, where all the B_i are translations and/or rotations of the measured beam pattern, B. The signal on the sky is $s_i = \int d\mathbf{x} B_i(\mathbf{x}) \Delta T(\mathbf{x})$. The covariance of the signal on the sky, V_{ij}^S, is then given by

$$V_{ij}^S = \int d\mathbf{x}_1\, d\mathbf{x}_2\, B_i(\mathbf{x}_1) B_j(\mathbf{x}_2) C(|\mathbf{x}_1 - \mathbf{x}_2|). \tag{5.2}$$

To simulate a measurement this signal covariance is added to the measured noise covariance, V_{ij}^M, to give the predicted total covariance of the sky binned data, V_{ij}^T. The variances can be summed because there is assumed to be no correlation between the sky signal and instrument noise covariances.

The likelihood ratio [Martin, 1971], λ, is chosen as the statistic to measure on the real and simulated skies, defined as

$$\lambda = \left(\frac{\det W^T}{\det W^M}\right)^{1/2} \exp\left(-\frac{1}{2}\sum_{kl} M_k (W_{kl}^T - W_{kl}^M) M_l\right). \tag{5.3}$$

where M_k is the measured signal, $W^T = (V^S + V^M)^{-1}$, and $W^M = (V^M)^{-1}$.

Let λ^* be the value of λ for our measurement, and $\rho_C(\lambda)$ be the probability density function of λ under the hypothesis that the fluctuations follow the correlation function C. Note that λ^* as well as $\rho_C(\lambda)$ depend on C. The cumulative probability,

$$\int_0^{\lambda^*} d\lambda\, \rho_C(\lambda) = P, \tag{5.4}$$

is used to set a confidence interval for C_0, by varying it to find a chosen value of P. The 95% lower limit on C_0 is the value for which $P = 0.05$ and the 95% upper limit is the value for which $P = 0.95$. The amplitudes reported are $[C_0]^{1/2}$. The parameter θ_c is adjusted to set the most restrictive upper bound on $[C_0]^{1/2}$. The upper and lower bounds determined in this way are shown in Table 5.1 for both the 1992 and 1994

flights. The confidence intervals set for the 1994 flight are consistent with those set in the 1992 flight. The MSAM1-92 bounds are higher than the MSAM1-94 bounds. Since the 1992 sky signal was largest near 15^h and the 1994 flight didn't observe long in that region of the sky, this is as expected.

			Double Difference $\theta_c = 0.^\circ3$		Single Difference $\theta_c = 0.^\circ5$	
Flight	Section	R.A.	Upper Bound (μK)	Lower Bound (μK)	Upper Bound (μK)	Lower Bound (μK)
MSAM1-94	1	15.27–16.84	132	44	163	40
	2	17.57–19.71	74	24	75	17
	All	15.27–19.71	78	34	79	30
MSAM1-92	All	14.44–20.33	97	50	116	53

Table 5.1: Upper and lower bounds on total rms CMBR anisotropy ($\sqrt{C_0}$). The limits in this table do not include the calibration uncertainty.

Taking into account the 10% uncertainty in the calibration, the resulting limits from the double difference data are $1.1 \times 10^{-5} \leq \Delta T/T \leq 3.1 \times 10^{-5}$ (90% confidence interval) for total rms fluctuations with a correlation angle, $\theta_c = 0.^\circ3$. For the single difference data, the limits are $1.0 \times 10^{-5} \leq \Delta T/T \leq 3.2 \times 10^{-5}$ (90% confidence interval) for total rms fluctuations with a correlation angle, $\theta_c = 0.^\circ5$.

5.3 1992 / 1994 flight Comparison Results

The signal is now compared at each point on the sky as measured in the two flights, not just the rms levels of the sky signal found in each data set. In the 1994 flight, the goal was to observe the identical swath of sky observed in the 1992 flight. As can be seen in Fig. 3-4 (enlarged in declination relative to right ascension) the 1994 flight was low in declination by about 10′. To enable a direct comparison, only the data from those bins which fall into the center declination bin are used. This selection cuts ~50% of the data. The data from the 1994 flight is subtracted from that of the 1992 flight to form a difference data set, *92−94* . Similarly, the two data sets are summed to form a sum data set, *92+94* . This is done for each demodulation and channel, as well as for both CMBR and DUST. To allow for differing offsets in the two flights, a weighted mean is removed from each dataset. The noise covariance matrix, V_{ij}, for

both the sum and difference sets is the sum of the masked 1992 and 1994 covariance matrices. There is no cross term because the flights have independent noise.

The *92+94* and *92−94* data sets for both the single and double difference demodulations are plotted below twice, using techniques fully described in Appendix G. Figure 5-1 and 5-2, for the CMBR and DUST, respectively, show *92+94* and *92−94* data in the diagonal basis, defined such that the covariance of the rotated data is diagonal. In this basis, the uncertainties in the individual values plotted are uncorrelated, providing a rigorously correct description of the errors on the points; however, the abscissa values do not have a one-to-one correspondence to locations on the sky. Figure 5-3 and 5-4, for the CMBR and DUST, respectively, show the same *92+94* and *92−94* data, after being rotated into the diagonal basis, having the highest noise mode removed, and being rotated back into the original basis. The covariance matrix resulting from this cutting procedure is nearly diagonal; the on-diagonal elements are used as the estimate of the variance on the corresponding data point. The χ^2 using this on-diagonal estimate is shown on each panel for each half of the data set and can be compared to the true χ^2 shown on the diagonal basis plots (Figure 5-1 and 5-2). However, due to the neglected non-zero off-diagonal elements, this χ^2 is not a formally correct representation of the significance in this data. This cutting procedure is done, not for further analysis, but exclusively for providing an intuitive picture of the data.

The significance of any detected signal in the sum or difference is tested with a χ^2 statistic,

$$\chi^2_{\pm} = \sum_{ij} (92 \pm 94)_i V_{ij}^{-1} (92 \pm 94)_j.$$

where i indexes a sky bin. The χ^2, degrees of freedom, and the cumulative probability, $P(\chi^2)$, for the comparison is shown in Table 5.2. P is the probability of drawing a value of χ^2 at or above the observed value, under the assumption that there is no signal in the data. Significantly overlapping signals should have a higher χ^2 in the sum than in the difference. This would be true even if the errors were estimated incorrectly. If the errors have been estimated correctly, and the signals are the same, the difference χ^2 should be approximately equal to the number of degrees of freedom in the dataset.

To check the effect of the relative calibration uncertainty on χ^2, the 1994 dataset is rescaled by $\pm 6\%$ (see 4.1.2) and the value of χ^2 recalculated. In all cases $|\Delta\chi^2| \leq 2$.

A Kolmogorov-Smirnov (KS) test is applied to the cumulative probabilities, $P(\chi^2)$, of the *92−94* data for the individual channels and for the CMBR and DUST. The KS test for the four channels for both demodulation probabilities gives 36% probability that these $P(\chi^2)$ are uniformly distributed between 0 and 1. The KS test of the *92−94*

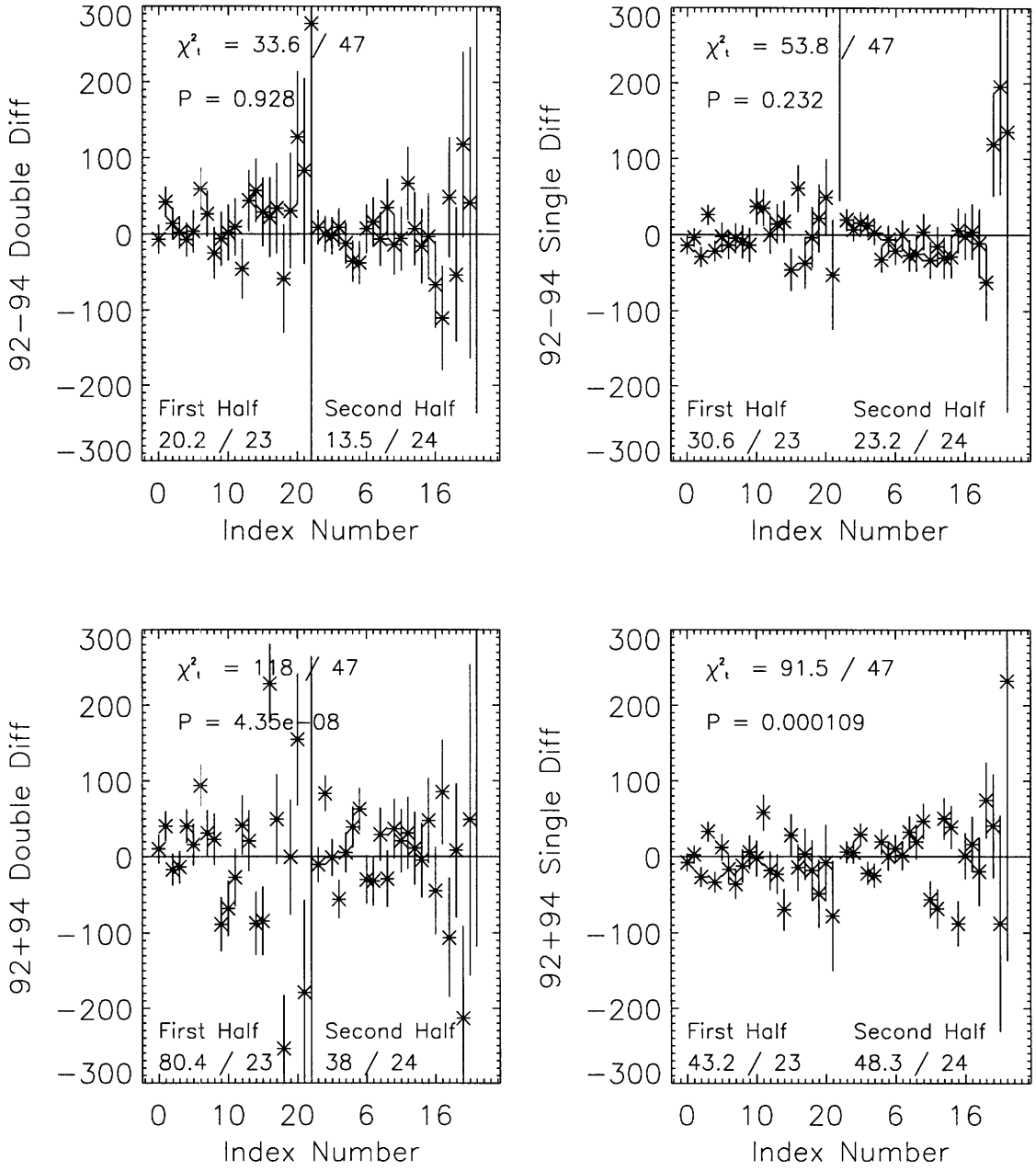

Figure 5-1: CMBR sum and difference data are shown in the rotated basis. In this basis, the data are shown with their corresponding uncorrelated 1-sigma error bars. The x-axis corresponds to mode number, where the modes are indexed by increasing variance separately for the two halves of the flights. The index numbers increase from 0 to 22 in the first half of the data set, and then again from 0 to 23 in the second half of the data set. The χ^2 / DOF for each half is shown in the lower part of each panel. χ^2_t is the sum of these two χ^2's.

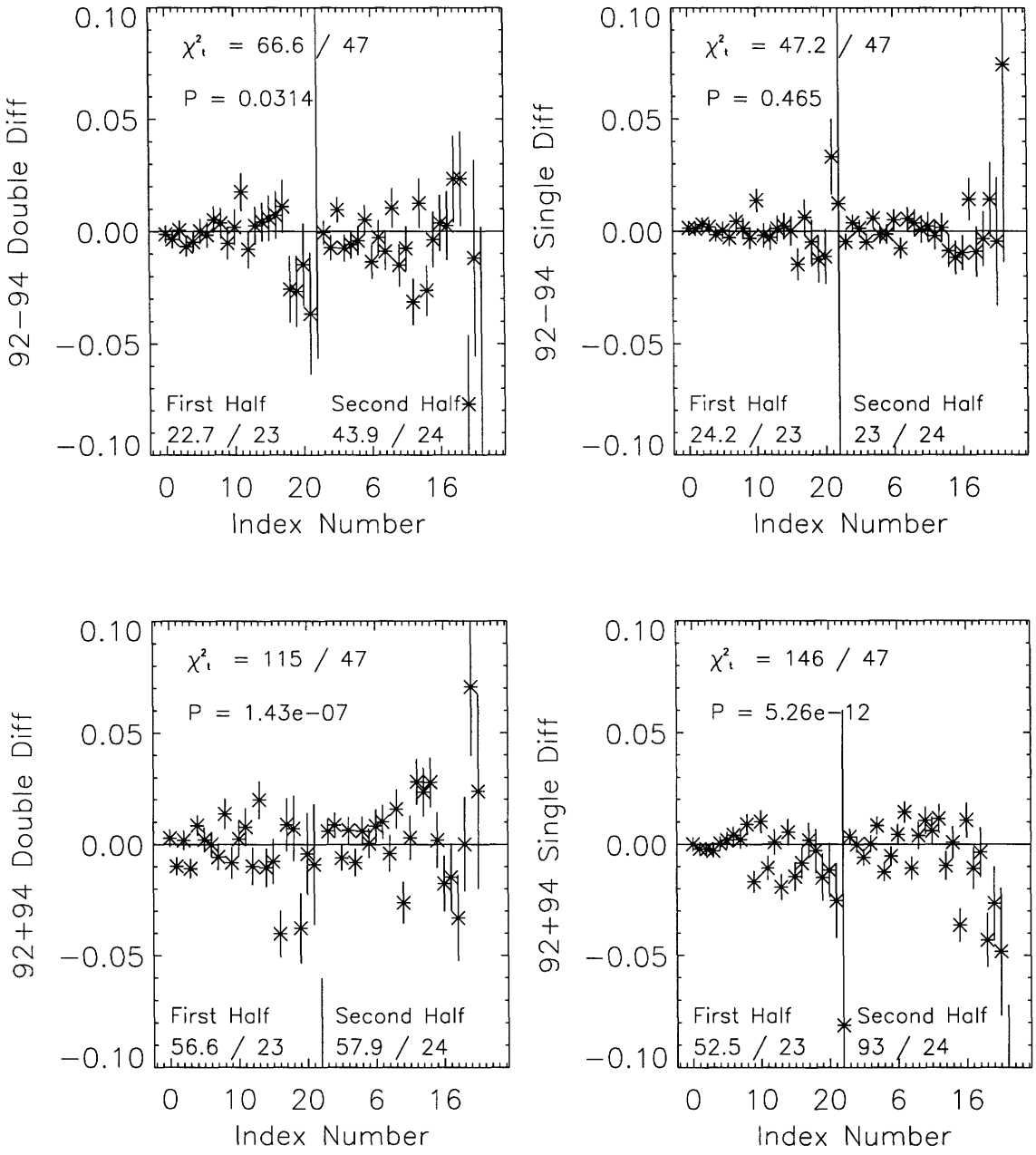

Figure 5-2: DUST sum and difference data are shown in the rotated basis. In this basis, the data are shown with their corresponding uncorrelated 1-sigma error bars. The x-axis corresponds to mode number, where the modes are indexed by increasing variance separately for the two halves of the flights. The index numbers increase from 0 to 22 in the first half of the data set, and then again from 0 to 23 in the second half of the data set. The χ^2 / DOF for each half is shown in the lower part of each panel. χ^2_t is the sum of these two χ^2's.

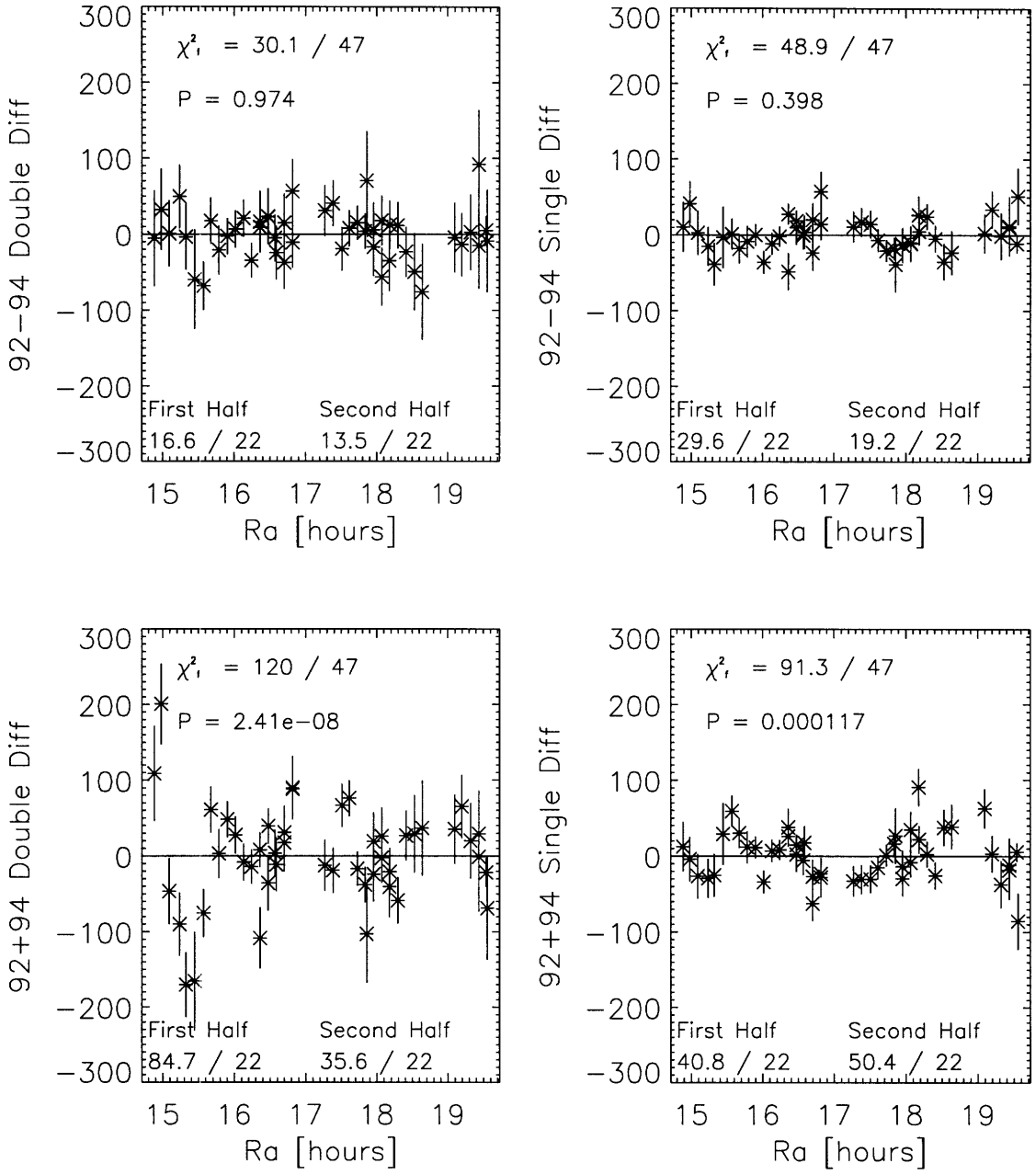

Figure 5-3: CMBR sum and difference data are shown. For this plot, the highest noise eigenvalue has been removed as described in Appendix G. The data are shown with the square root of the corresponding on-diagonal element of the covariance matrix plotted as the 1-sigma error bar. The χ^2 ($\sum_i \text{data}_i^2/\sigma_i^2$) / DOF for each half flight is shown in the lower part of each panel. χ_f^2 is the sum of these two χ^2's.

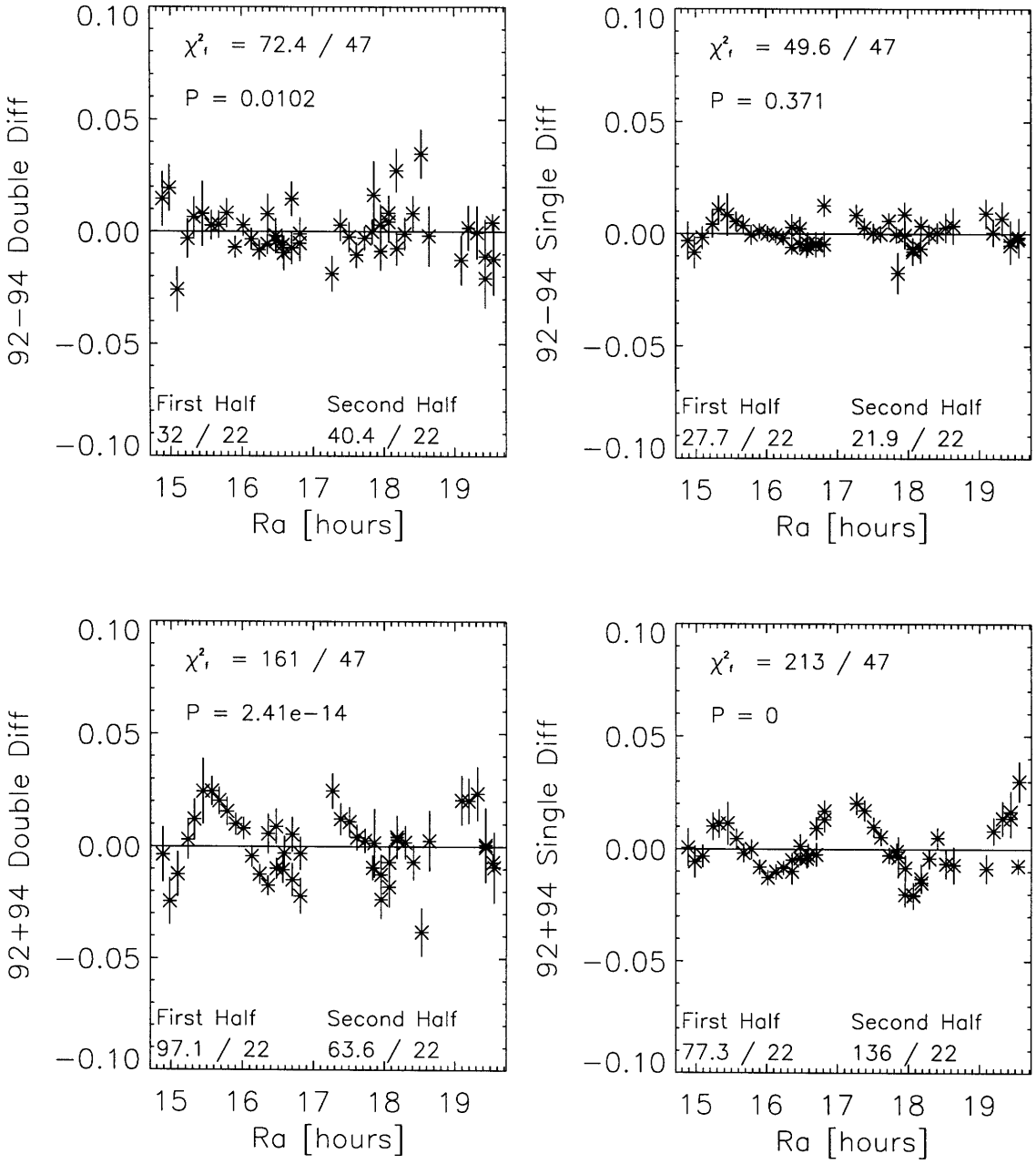

Figure 5-4: DUST sum and difference data are shown. For this plot, the highest noise eigenvalue has been removed as described in Appendix G. The data are shown with the square root of the corresponding on-diagonal element of the covariance matrix plotted as the 1-sigma error bar. The χ^2 ($\sum_i \text{data}_i^2/\sigma_i^2$) / DOF for each half flight is shown in the lower part of each panel. χ^2_f is the sum of these two χ^2's.

CMBR and DUST probabilities (.04, .22, .41, and .91) gives a 74% probability that these are consistent with a uniform distribution. Based on this, the *92–94* data in both the single and double difference demodulations for all channels, as well as the CMBR and DUST components, is consistent with no observed signal.

The KS test of the *92+94* probabilities for the four channels for both demodulation gives 7% probability these are uniformly distributed. This alone would be inconclusive; however, stronger conclusions can be drawn by considering the CMBR and DUST components. For CMBR and DUST, the KS test of gives a 7×10^{-4} probability that these are drawn from a uniform distribution from 0 to 1. This, together with the extremely low χ^2 probabilities themselves, show there are statistically significant signals in all the *92+94* decomposed datasets. This result, combined with the absence of such signals in the *92–94* datasets, compels me to conclude that the signals observed during the two flights are common, and therefore present on the sky.

Type	Data Set	Double Difference		Single Difference	
		χ^2 /DOF	P	χ^2 /DOF	P
Channel 1	*92–94*	42 / 45	0.60	58 / 45	0.09
	92+94	111 / 45	2×10^{-7}	72 / 45	7×10^{-3}
Channel 2	*92–94*	41 / 45	0.62	30 / 45	0.96
	92+94	60 / 45	.06	52 / 45	.22
Channel 3	*92–94*	53 / 45	0.18	51 / 45	0.26
	92+94	104 / 45	1×10^{-6}	127 / 45	8×10^{-10}
Channel 4	*92–94*	42 / 45	0.59	35 / 45	0.85
	92+94	44 / 45	0.49	43 / 45	0.56
CMBR	*92–94*	33 / 45	0.91	52 / 45	0.22
	92+94	118 / 45	2×10^{-8}	89 / 45	1×10^{-4}
DUST	*92–94*	63 / 45	0.04	47 / 45	0.41
	92+94	109 / 45	4×10^{-7}	145 / 45	2×10^{-12}

Table 5.2: Comparison of 1992 and 1994 Data Sets

The same region of the sky was observed in the 1992 and 1994 flights to confirm the detection of a celestial signal. It is clear from the statistical analysis that the same

sky signal is measured in these two flights. At the level of our signal, this implies that the MSAM1 measurements are free from significant contamination from time-varying systematics such as sidelobe pickup or atmospheric contamination.

5.4 Astrophysical Foregrounds

In the introduction, concerns were raised about the signal due to Galactic and extragalactic foreground sources. The most important source at our observing frequencies is the emission from warm interstellar dust, which has been accounted for in the decomposition part of the analysis (Section 4.1.8). The Galactic synchrotron and free-free emissions are negligible: synchrotron emission is prominent in the 1420 /MHz Sky Maps [Reich and Reich, 1986], with a brightness temperature of roughly 3.5 K in this field. The synchrotron emission is expected to have a power law frequency spectra, $I_\nu \propto \nu^\alpha$, where $\alpha \sim -0.7$. Converting this emission to Raleigh Jeans temperature units, the radiation temperature scales with frequency like $\nu^{-2.7}$. The 3.5 K emission at 1420 MHz implies 7 μK, a negligible contribution at the MSAM1 observing frequencies. Limits on free-free emission can be extrapolated from measurements of Hα emission near the north celestial pole. These suggest that the contrast in free-free emission on the degree-scale should have a total rms $< 1\,\mu$K when scaled to 5.7 cm^{-1}[Gaustad et al., 1995], [Simonetti et al., 1996].

Another source for confusing astrophysical signals is from extragalactic compact objects. The possibility is considered that the bright emission feature near the beginning of the observations in MSAM1-92 is due to such as object. To be a point source, this feature requires a flux density, $S_\nu \sim 5$ Jy at 5.7 cm^{-1}. A search of the 5 GHz S5 Polar Cap Survey ([Kuehr et al., 1981]) indicated no counterparts within one beamwidth of the brightest two features in the MSAM1-92 data set [Kowitt et al., 1996]. The S5 survey is estimated to be complete at 5 GHz down to 250 mJy, ruling out any known type of radio counterpart for this feature.

The double difference signal has independently been confirmed recently by the Saskatoon experiment. The Saskatoon instrument observed this section of sky at lower frequencies, 36 GHz to 46 GHz ([Netterfield et al., 1996]). They have compared their signal with that from MSAM1-92, and find good agreement in magnitude and shape of the signal. A plot of the comparable data from the Saskatoon and the MSAM1-92 experiments, as well as the sum and difference of those two data sets are shown in Figure 5-5, reproduced here from [Netterfield et al., 1996]. The reduced χ^2 quoted from [Netterfield et al., 1996] is 3.43 for the sum, and 1.05 for the difference, where they have ignored the third sample at 14.58^h in right ascension in the MSAM1-

92 data set. Although unable to check the single difference result, this confirmation of the double difference, spanning nearly a decade in frequency, is strong evidence that MSAM1 is observing CMBR anisotropies rather than some other astrophysical foreground source.

5.5 Conclusions

In conclusion, the MSAM1 instrument has made measurements of CMBR anisotropy at the half-degree angular scale. The detections reproduce on the sky, from flights in different years with a modified instrument. This result allows one to conclude that this kind of balloon-borne experiment is capable of making reproducible measurements of CMBR anisotropy.

The future of this work is observing more sky. However, as experiments become more aggressive with observing strategies, continued diligence against systematic effects is crucial to the ongoing success of our field.

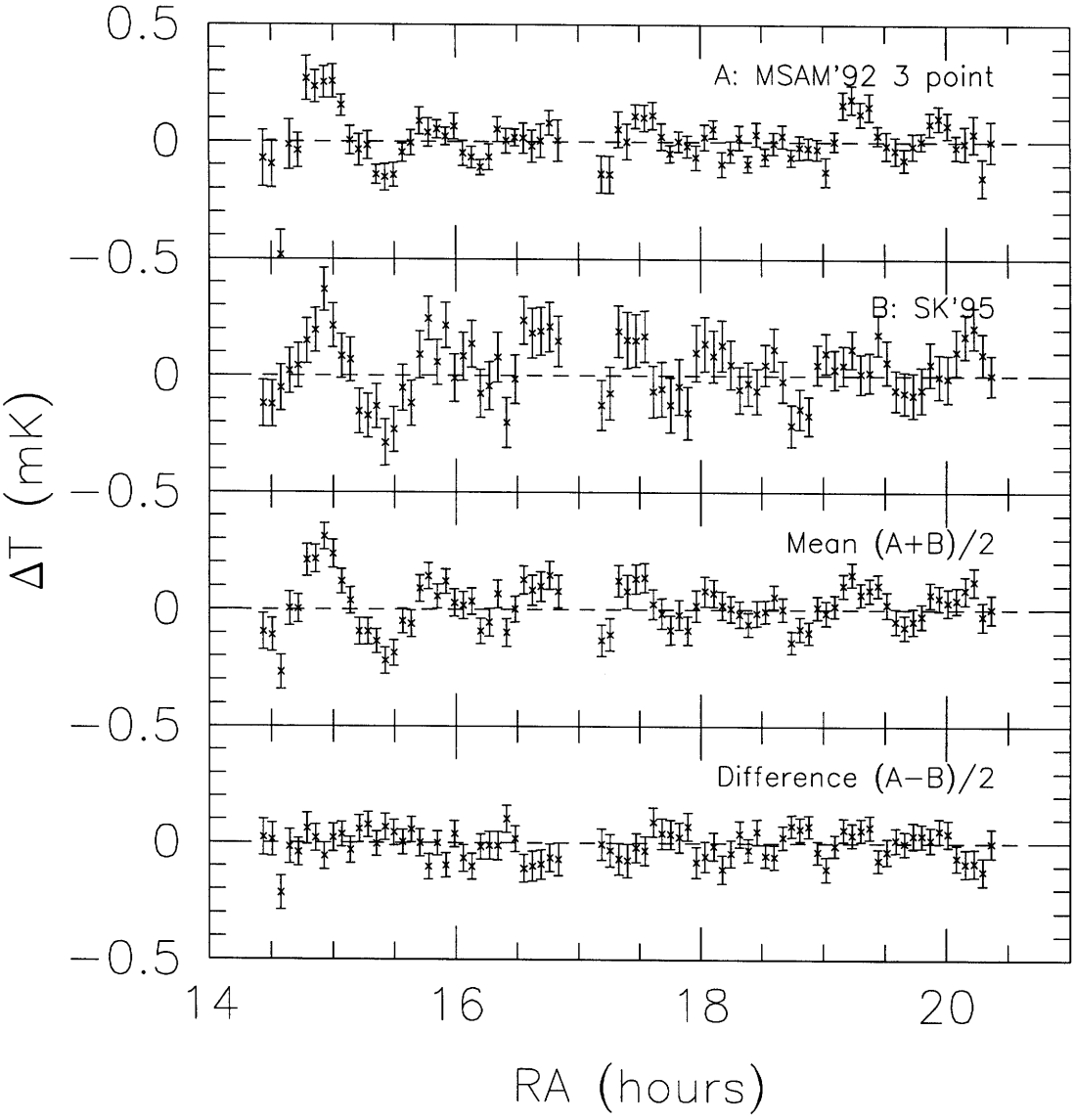

Figure 5-5: Comparison of the MSAM1-92 and SK95, reproduced from [Netterfield et al., 1996]. The first panel shows the MSAM1-92 double difference data from the 1992 main analysis. The second panel gives the corresponding data from the Saskatoon experiment. The third shows the sum, and the fourth the difference.

Appendix A

Preamplifier Design

The 1994 preamplifier design is shown in Figure A-1. It was built to drive the existing cold JFETs, and act as the first warm stage of amplification. This is a modification of a circuit design by Dan MacCammon of University of Wisconsin.

The drawing shows a schematic of the amplifier board. There is a separate Vector card containing this circuit for each of the four signal channels. The box containing the boards has an extra board which forms and filters the 10 Volt reference signal. The box is mounted to the side of the radiometer, and receives power (± 15 Volts) from the main electronics box (MEB), which also regulates the preamplifier box temperature. The ± 15 Volts is regulated down to ± 12 Volts and filtered to run the operational amplifiers (op-amp's) in the amplifier circuit.

The ± 10 Volt reference signal is produced by a low noise voltage reference chip (AD587U with $60\text{nV}/\sqrt{\text{Hz}}$), and received differentially on each amplifier card. This is divided down with a series of resistors to the appropriate bias voltage for the detectors, V_{bias}. It serves as the bias voltage for the internal JFET, V_{Adrain}. There are two internal JFETs per channel in the radiometer. One of these, B, is not used, so its drain and source are tied together to V_{Adrain}. The 10 Volt is also inverted to provide a -10Volt reference voltage. The internal JFET is run as a source follower, giving it a roughly temperature independent gain of one. It is typically biased with about $200\,\mu A$. The $15\,k\Omega$ resistor above V_{Adrain} reduces the voltage from 10 Volt to ~ 6 Volt, to help prevent current noise in the JFET.

The signal is on the JFET source, V_{Asource}, read through a $39\,\text{k}\Omega$ resistor. This signal inputs to one side of a "long tail pair", a dual JFET (NJ132) run with an op-amp attached differentially to the two drain voltages. The NJ132 has very good noise performance, measured as low as $3.5\text{nV}/\sqrt{\text{Hz}}$ in this circuit at 2 Hz. This JFET is biased with a current source made with a biased 2N2222 transistor. The feed back of the long tail pair goes through a resistor capacitor network which has gain of one at

DC, gain of one at high frequency, and gain of 30 in this case at band pass frequencies. The gain is set by the ratio of the capacitors. The low and high cut off frequencies are set by the resistor/capacitor sets.

The signal out of the first op-amp is offset by 0.4 Volt for maximum dynamic range: this is the average of the DC level measured before flight. An additional op-amp provides an additional gain of 10, giving an overall gain of 300 for the AC signal, and an overall gain of 10 for the DC signal. This op-amp also produces a buffered copy of the board ground voltage to send as a reference voltage with the signal to the MEB.

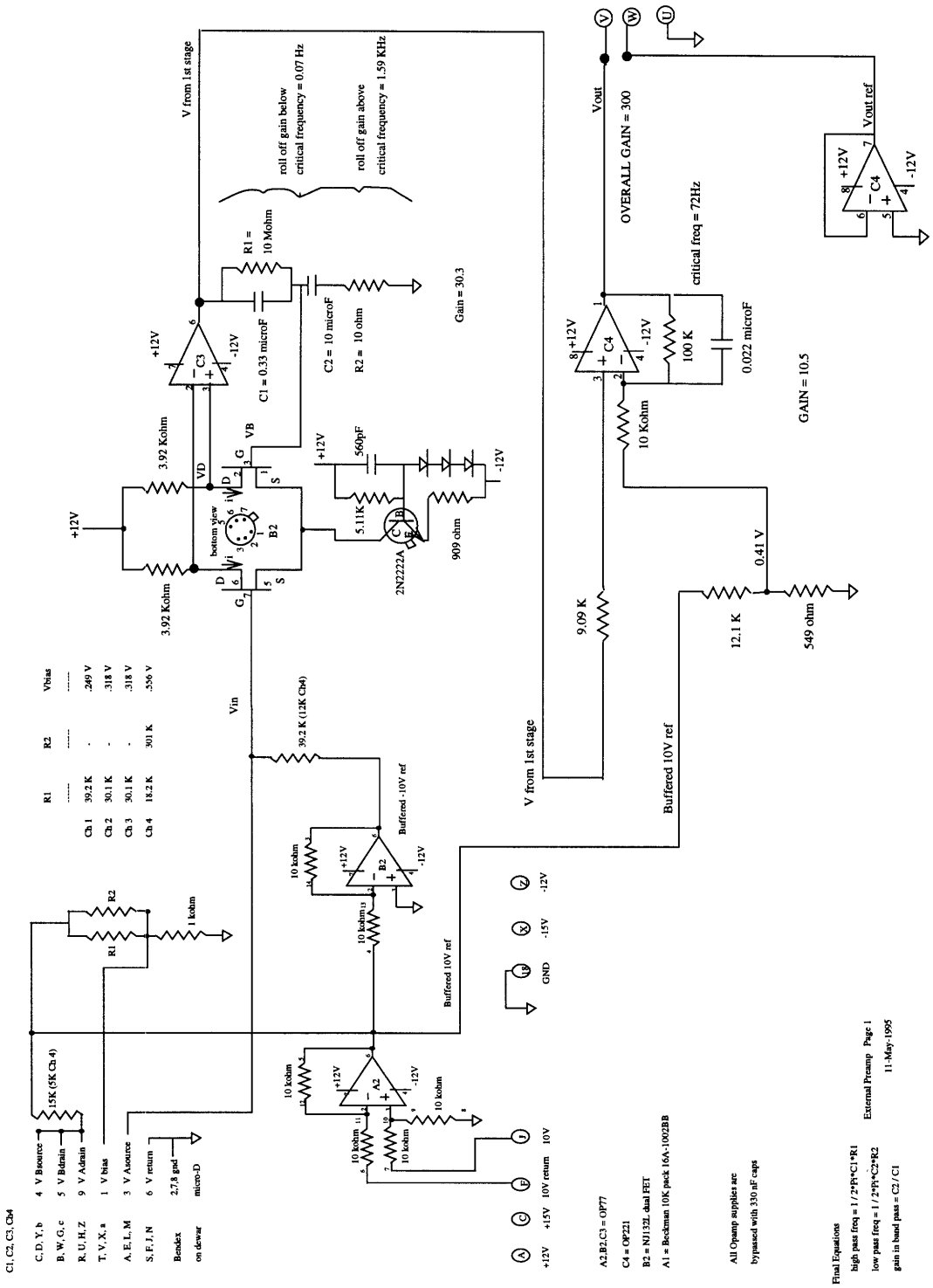

Figure A-1: Schematic of MSAM1-94 Preamplifier

Appendix B

In Flight Noise Performance

The initial noise performance estimates for the radiometer were made for the FIRS flights and are described in [Page, 1989]. The framework for understanding bolometer performance used therein is the bolometer model of Mather ([Mather, 1982], [Mather, 1984a], and [Mather, 1984b]). Some of the relevant bolometer parameters are given in Table B.1.

The in-flight noise performance of the MSAM1 instrument is measured by taking the power spectrum of approximately 5 minutes of post-deglitched, offset-removed data, for each of the four channels. Although this noise is measured from the end of the full signal chain (Point C in Figure 2-7), it has been referenced to the input to the internal preamplifier (Point A in Figure 2-7) in order to understand the noise at that point. Possible noise sources include noise at the bolometer (Johnson noise and thermal noise), input photon noise, readout noise in the electronics, and $1/f$ noise at the input to the internal preamplifier.

The noise power spectrum is modeled with the following components, $V_{\rm flat}$, $V_{\rm power}$, $V_{\rm readout}$, and $V_{1/f}$. $V_{\rm flat}$ has a flat voltage noise power spectrum at the input to the internal pre-amplifier (point A in Figure 2-7), as would the Johnson noise from the detector and bias resistor, or amplifier white noise in the internal pre-amplifier. $V_{\rm power}$ has a flat input power, which is the sum of thermal noise associated with the "legs" of the bolometer, or input photon noise. Since this is a power noise it must be multiplied by the voltage responsivity to give a predicted voltage noise power spectrum at the input to the internal preamplifier. The voltage responsivity is a function of the detector time constant, τ, which was measured in flight from cosmic ray strikes. Since the responsivity, $S(\omega)$ (ω is the angular frequency $= 2\pi f$), is proportional to $1/(1+i\omega\tau)$, this component of the noise has a $\mid (1/(1+i\omega\tau)) \mid$ spectrum. $V_{\rm readout}$ is white noise injected after the first stages of amplification (Point B on Figure 2-7). $V_{1/f}$ has a $1/f$ spectrum, possibly from excess noise in the cold JFET. Microphonic noise

likely due to capacitive pickup has an unknown spectrum, and therefore could mimic any of the above components. The measured noise power spectrum are modeled as the quadratic sum of noise power spectra,

$$\begin{aligned} V_{\rm Fit}^2 &= V_{\rm flat}^2 \times (A(\omega) \times I(\omega))^2 + \\ & V_{\rm power}^2 \times (S(\omega) \times A(\omega) \times I(\omega))^2 + \\ & V_{\rm readout}^2 \times (I(\omega))^2 + \\ & V_{1/f}^2 \times 1/f(\times A(\omega) \times I(\omega))^2, \end{aligned} \tag{B.1}$$

where $A(\omega)$ is the measured analog transfer function versus frequency, $I(\omega)$ is the frequency response of the integrating filter sampled at 32 Hz, $I(\omega) = 64/\omega \times \sin(\omega/64)$, and $V_{\rm flat}^2$, $V_{\rm power}^2$, $V_{\rm readout}^2$, and $V_{1/f}^2$ are the free parameters of the fit. Curves of the measured power spectra, and the power spectra of each noise component multiplied by its amplitude, are shown in Figures B-1 through B-4 (all curves are referenced to point A in Fig. 2-7).

The fit noise levels are shown in Table B.1. The model worked fairly well for channels 1 and 4. The model did not work well for channels 2 and 3. This is due both to the $1/f$ noise not fitting the $1/f$ spectrum, and because there is excess microphonic noise from 2.5 to about 7 Hz, mostly in Channel 3. For Channels 2 and 3, the $V_{\rm flat}$ values can probably be used as upper limits for the true Johnson noise. It is clear that voltage noise dominates in all four channels, and that the "$1/f$ knee" is at about 0.8 Hz. This voltage noise is probably too high in all channels to be Johnson noise, and is most likely due to capacitive microphonic noise in the signal wires or current noise in the cold JFET. The voltage noise of the amplifier chain is measured to be $\sim$ $15{\rm nV}/\sqrt{\rm Hz}$. Since all components of the amplifier chain are temperature regulated, this noise is not expected to change in-flight, thus being negligible in all but channel 4, where it is probably the dominant noise source.

The detector time constants, τ, for MSAM1 were found to be substantially longer than those measured in the FIRS flight for the same detectors. This may be due to different in-flight radiation loading. The Mather bolometer model is used to find a set of inputs which could describe the observed time constants, various predictions of which are shown in Table B.1.

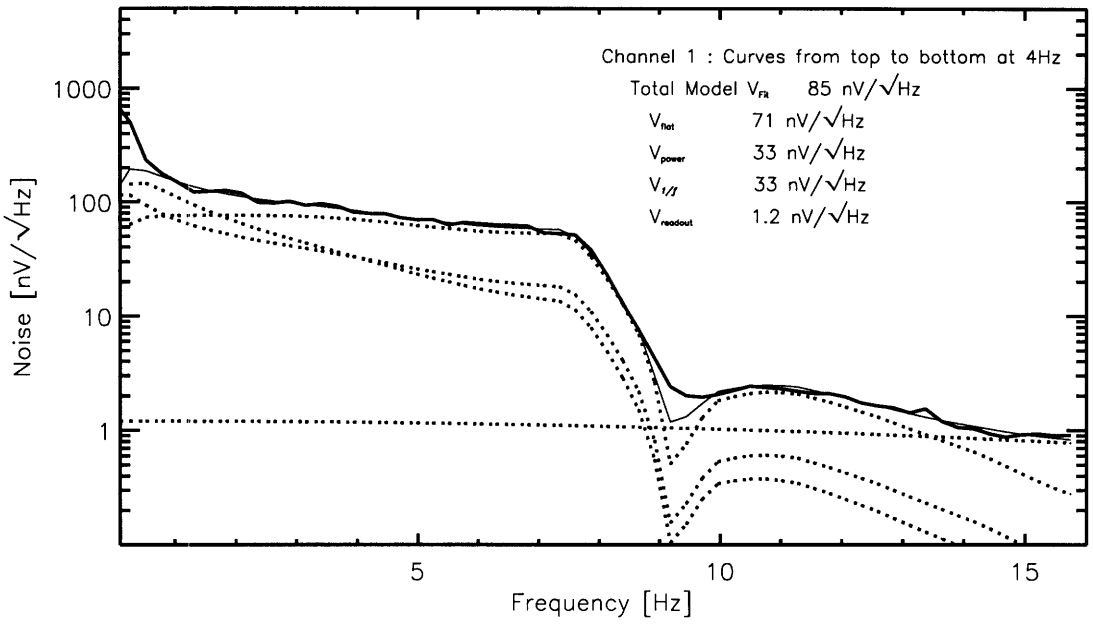

Figure B-1: In Flight Noise for Channel 1. Curves of the measured noise power spectra (solid), the fit (thin solid), and the power spectra of each noise component multiplied by its fit amplitude (dotted), are shown. All curves are referenced to point A in Fig. 2-7.

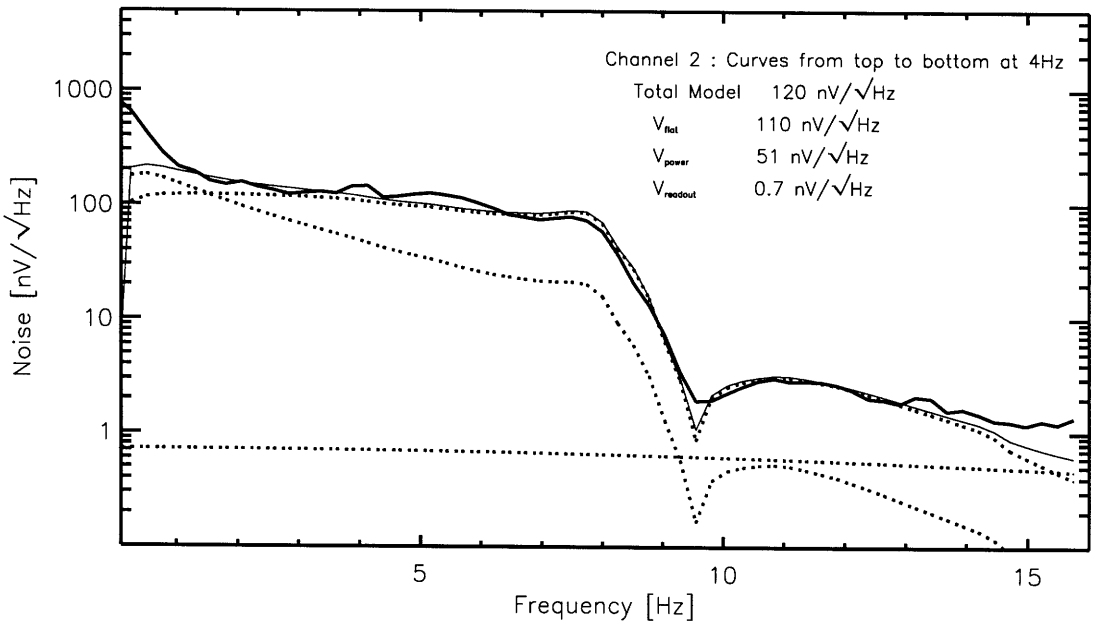

Figure B-2: In Flight Noise for Channel 2. Curves of the measured noise power spectra (solid), the fit (thin solid), and the power spectra of each noise component multiplied by its fit amplitude (dotted), are shown. All curves are referenced to point A in Fig. 2-7.

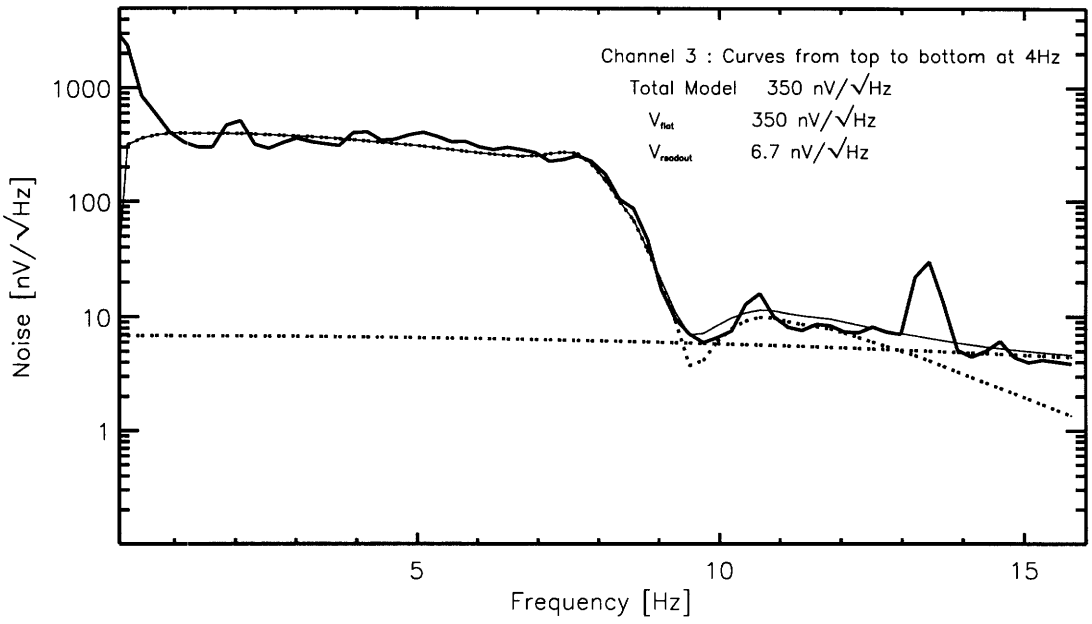

Figure B-3: In Flight Noise for Channel 3. Curves of the measured noise power spectra (solid), the fit (thin solid), and the power spectra of each noise component multiplied by its fit amplitude (dotted), are shown. All curves are referenced to point A in Fig. 2-7.

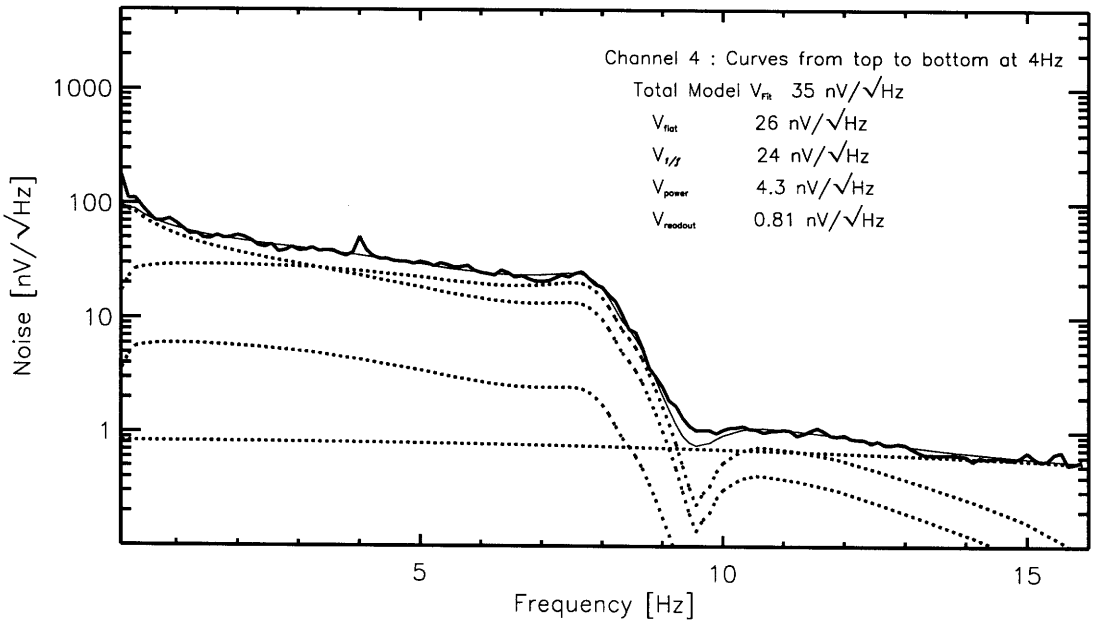

Figure B-4: In Flight Noise for Channel 4. Curves of the measured noise power spectra (solid), the fit (thin solid), and the power spectra of each noise component multiplied by its fit amplitude (dotted), are shown. All curves are referenced to point A in Fig. 2-7.

Channel	1	2	3	4
Operating Conditions:				
Vbias[V]	0.20	0.275	0.317	0.764
$R_L[M\Omega]$	90	60	80	20
Detector Parameters:				
$R_0[\Omega]$	1627	1698	1383	2902
T_0 [K]	45.0	36.6	44.3	16.5
$G_0[W/K^4]$	3.2×10^{-8}	7.6×10^{-8}	5.9×10^{-8}	4.4×10^{-8}
Measured Quantities:				
τ_{det}[ms]	205	150	50	30
V_{flat}(@ 4 Hz) $[V/\sqrt{Hz}]$	7.0×10^{-8}	1.1×10^{-7}	3.5×10^{-7}	2.6×10^{-8}
V_{power}(@ 4 Hz) $[V/\sqrt{Hz}]$	3.3×10^{-8}	5.1×10^{-8}	...	4.3×10^{-9}
NET_{92}(RJ) $[\mu K\sqrt{s}]$	400	210	140	330
NET_{94}(RJ) $[\mu K\sqrt{s}]$	240	150	80	230
NET_{94}(CMBR) $[\mu K\sqrt{s}]$	490	850	...	...

Table B.1: Detector Summary

Appendix C

Flight Summaries

Shown below is a summary of all the principal flight activities for MSAM1-92.

Event	~UT	~Duration [hours:min]
Launch	00:59	...
Elevation Controlled	01:06	...
Azimuth Controlled	02:08	...
Observed Moon	02:42	00:09
Azimuth Spin	02:54	00:15
Elevation Scans	03:13	00:04
Observed Jupiter	03:29	00:31
CMBR Scans	04:20	02:01
Observe Coma	06:41	00:13
CMBR Scans	07:02	02:48
Observe Saturn	09:56	00:46
Elevation Scans	10:46	00:06
Azimuth Sunrise Spin	10:53	00:23
Shutter Closed	11:18	00:21
Sunlight Scans	10:53	00:03
Power off	11:49	...

Table C.1: 1992 Flight Summary

Shown below is a summary of all the principal flight activities for MSAM1-94.

Event	~UT	~Duration [hours:min]
Launch	00:59	...
Elevation Controlled	01:14	...
Azimuth Controlled	02:04	...
Observed Jupiter	02:37	01:48
CMBR Scans	05:11	01:28
Observe Jupiter	06:49	00:20
CMBR Scans	07:21	02:22
Observe M31	09:54	00:33
Elevation Scans	10:54	00:11
Elevation Holds	11:05	00:27
Shutter Closed	11:35	00:25
Power off	12:04	...

Table C.2: 1994 Flight Summary

Appendix D

Cosmic Rays

"Glitches," caused by cosmic rays in the upper atmosphere impinging on the detectors and signal electronics are prominent in the raw, offset subtracted, signal stream. These are removed to form the deglitched signal stream. There are two types of glitches, Type 1 and Type 2, as discussed in Chapter 4 in Section 4.1.1. Type 1 spikes appear to be thermalized in the detector, while Type 2 do not. The arrival rates of the two glitch types, as well as the energy spectrum are discussed below.

A histogram of the separation time between adjacent glitches is plotted in Fig. D-1 for the Type 1 glitches and in Fig. D-2 for the Type 2 glitches. If the glitches are cosmic rays their arrival time should be random, thus the number vs separation should follow an exponential where the time constant is τ, and $\frac{1}{\tau}$ is the arrival rate. These fits are overlayed.

The number versus energy is plotted in Fig. D-3 and D-4 for Type 1 and Type 2 respectively. The positive energy glitches are shown as a solid line, the negative energy glitches are shown as a dashed line. For Type 1, the negative energy pulses can not be due to cosmic rays thermalized in the detector because these can only have positive energy. Thus the negative pulses are indicative of the noise contamination in the identified glitch population; this contamination is only a small contribution to the energy spectrum. For the Type 2 glitches, since they do not appear to be absorptions by the bolometer, the amplitudes are not necessarily positive. A possible source for these is absorbed cosmic ray energy into a JFET either in the internal preamplifier or the external preamplifier. The internal preamplifier has a JFET run in a single-ended configuration, so the amplitude of absorbed radiation is likely to have a set sign, while the JFET in the external preamplifier is dual JFET, thus cosmic rays here would have an equal probability of effecting the signal with a positive or negative spike. The detectors have an active absorbing area of $0.25\,\mathrm{cm}^2$. The internal JFET (NJ4867A) has a gate area of $0.11\,\mathrm{cm}^2$, about 1/5 of which is active area. The

external JFET (NJ132L) has a gate area of $0.14\,\mathrm{cm}^2$, about 1/3 of which is active area. While not definitive, it is plausible that cosmic rays striking a JFET could be the source of the Type 2 glitches. There is a low amplitude cutoff due to the fact that if the spike amplitude has less that $3\,\sigma$ significance it is not considered a glitch. The smooth high amplitude roll off is probably due to high amplitude glitches fitting poorly, and thus being thrown out. In between, the spectrum is roughly a power law.

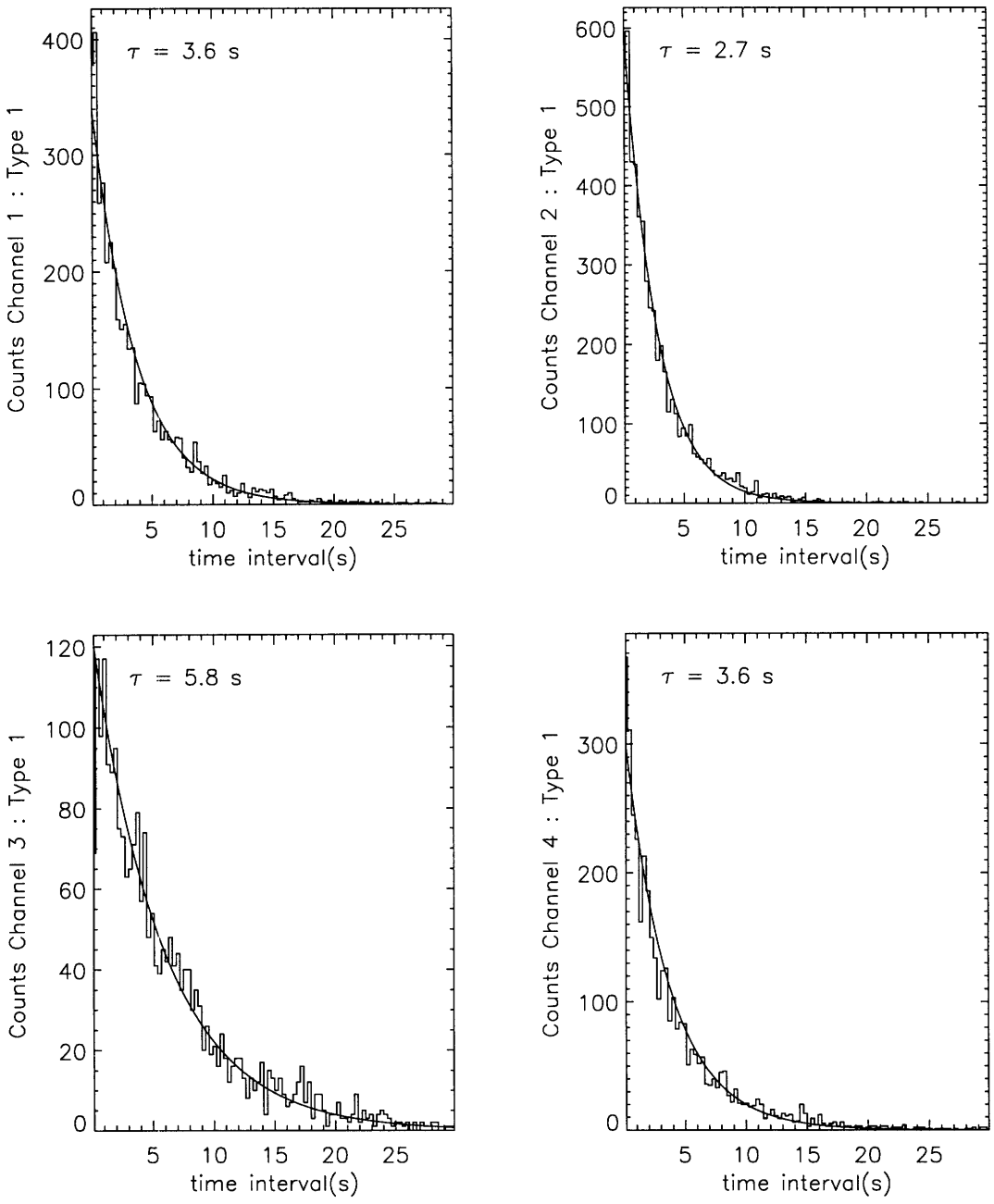

Figure D-1: Cosmic Ray Rate Spectrum for Type 1 glitches. Overlayed is the exponential fit. $\frac{1}{\tau}$ is the average arrival rate.

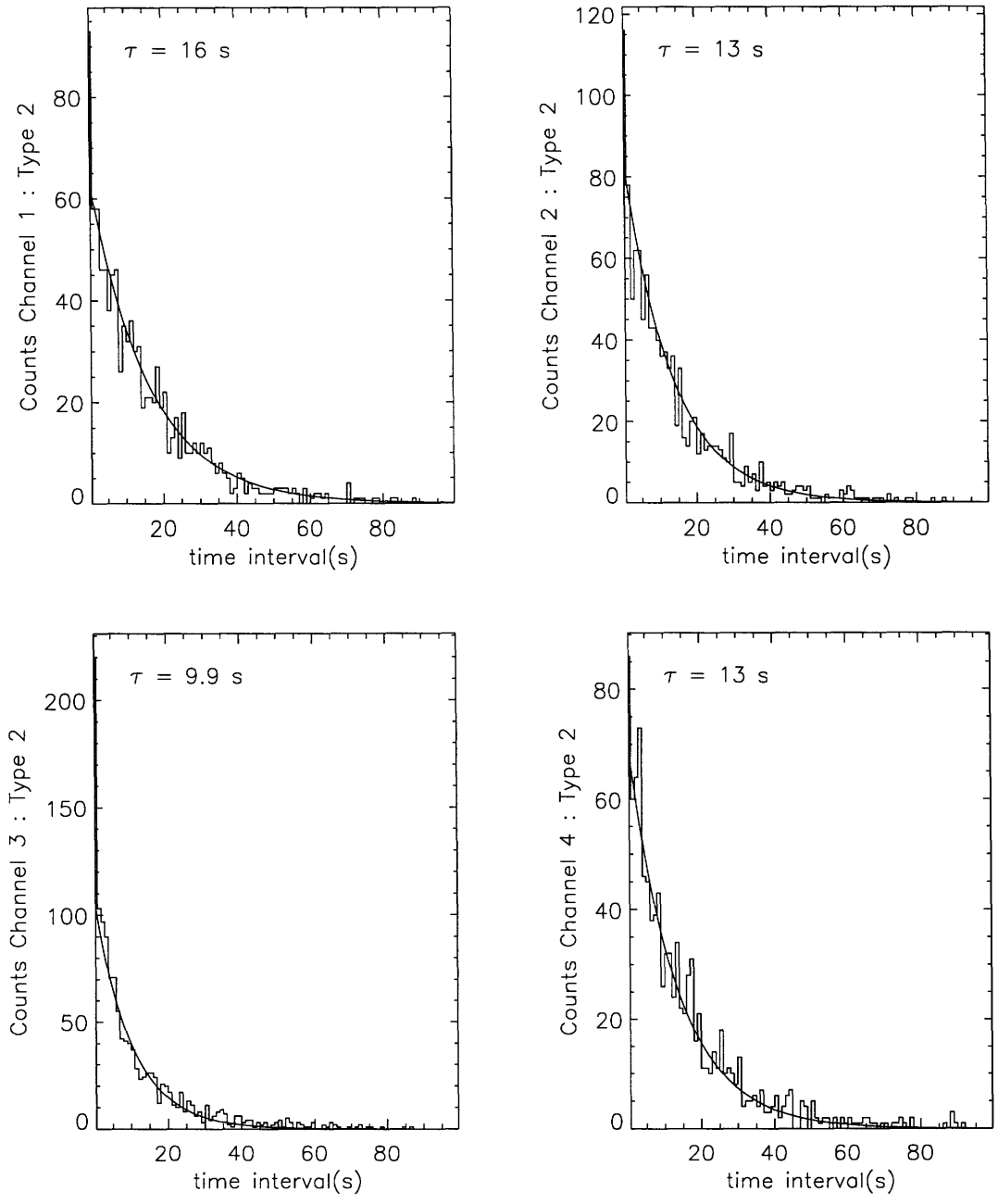

Figure D-2: Cosmic Ray rate spectrum for Type 2 glitches. Overlayed is the exponential fit. $\frac{1}{\tau}$ is the average arrival rate.

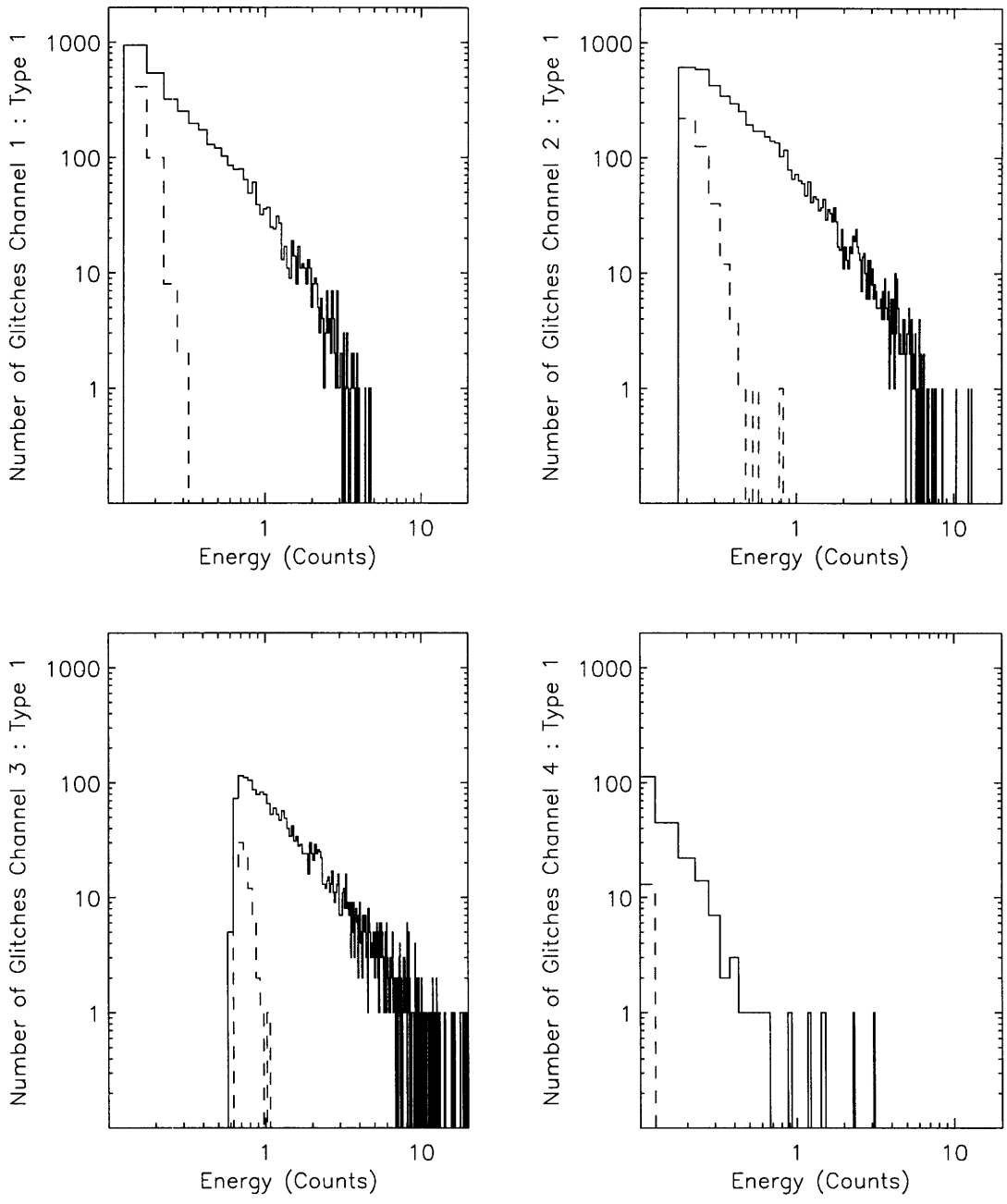

Figure D-3: Cosmic ray number spectrum for Type 1 glitches. The positive power glitches are shown as a solid line, the negative power glitches are shown as a dashed line.

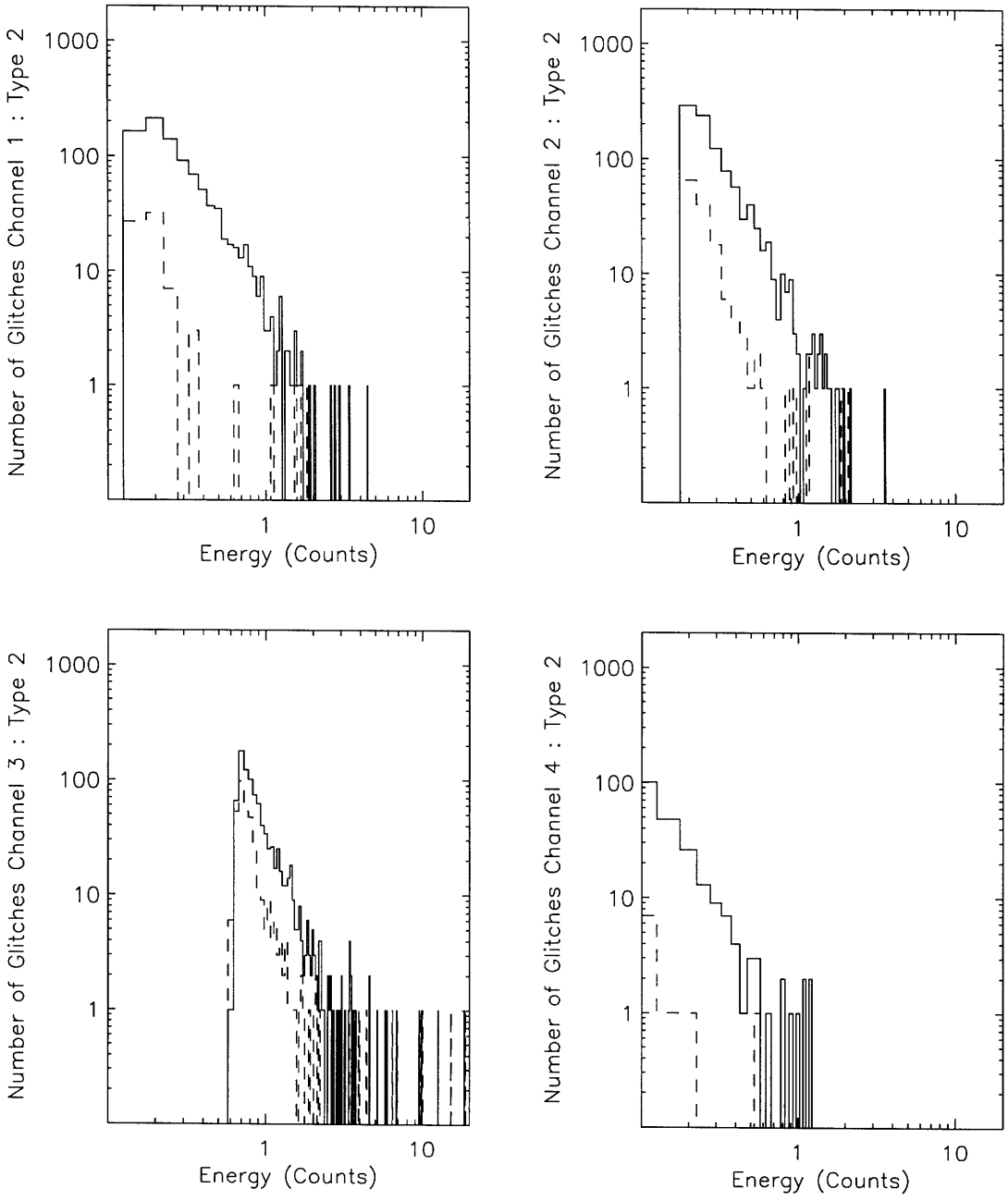

Figure D-4: Cosmic ray number spectrum for Type 2 glitches. The positive power glitches are shown as a solid line, the negative power glitches are shown as a dashed line.

Appendix E

In Flight Noise Estimates

The noise on the demodulated data, $\langle t_i t_i \rangle$ was estimated from the rms in each minute of demodulated data. These noise estimates are plotted below for the 1994 and 1992 data. The 1994 estimates are close to constant. The noise estimates for the 1992 data show much greater variability.

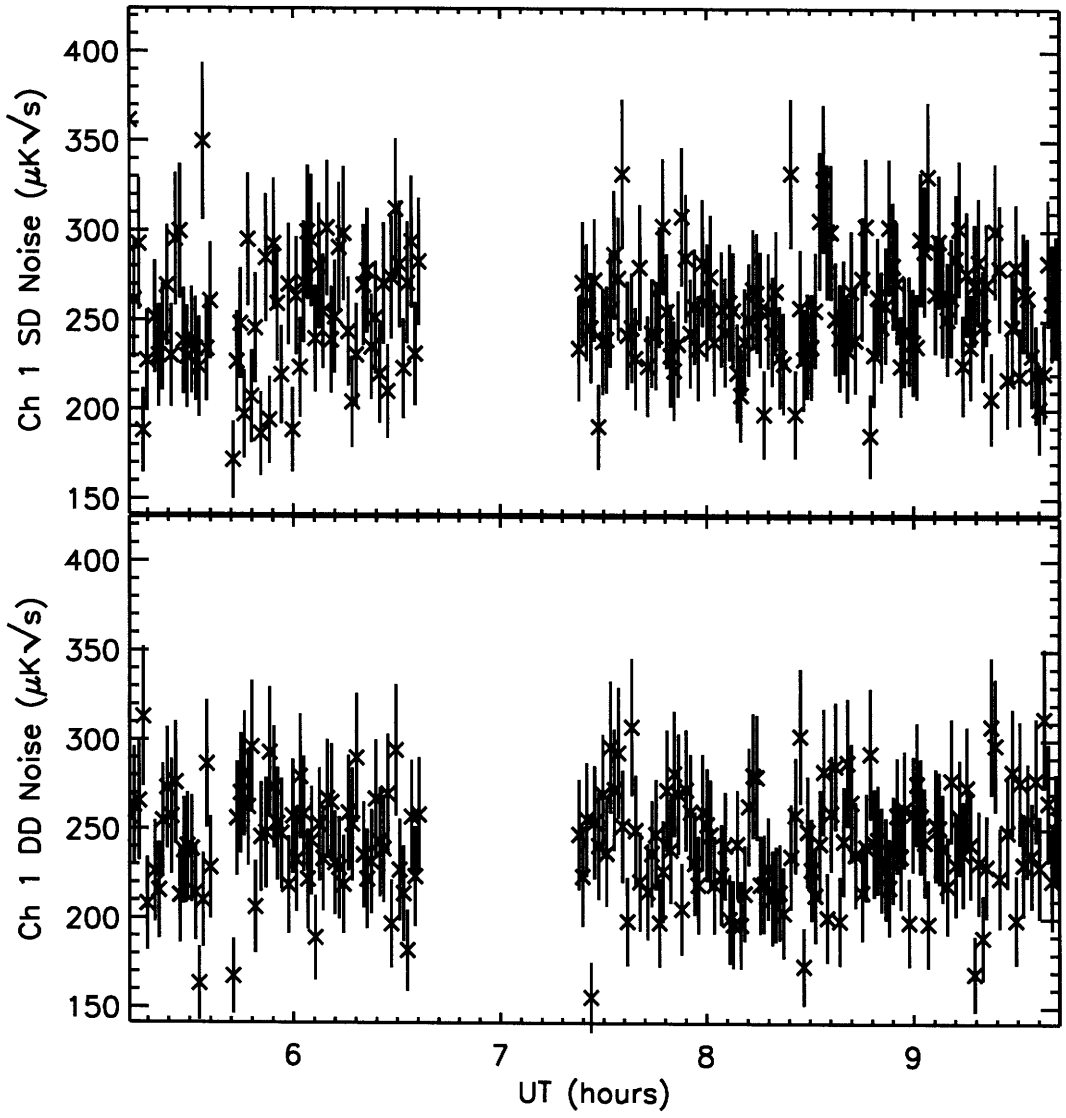

Figure E-1: 1994 Flight noise estimates for each minute of data in $\mu K_{RJ}\sqrt{s}$: Channel 1.

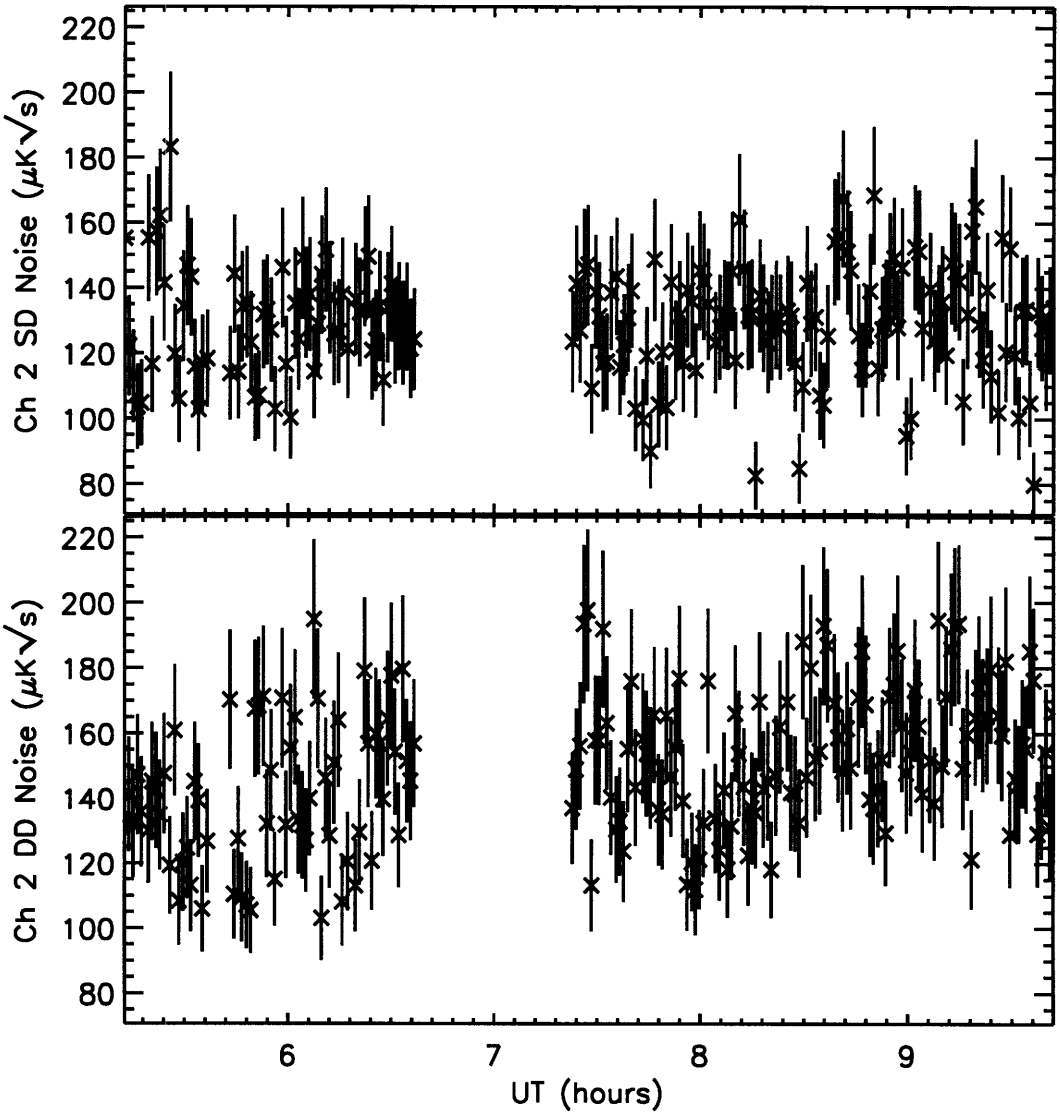

Figure E-2: 1994 Flight noise estimates for each minute of data in $\mu K_{RJ}\sqrt{s}$: Channel 2.

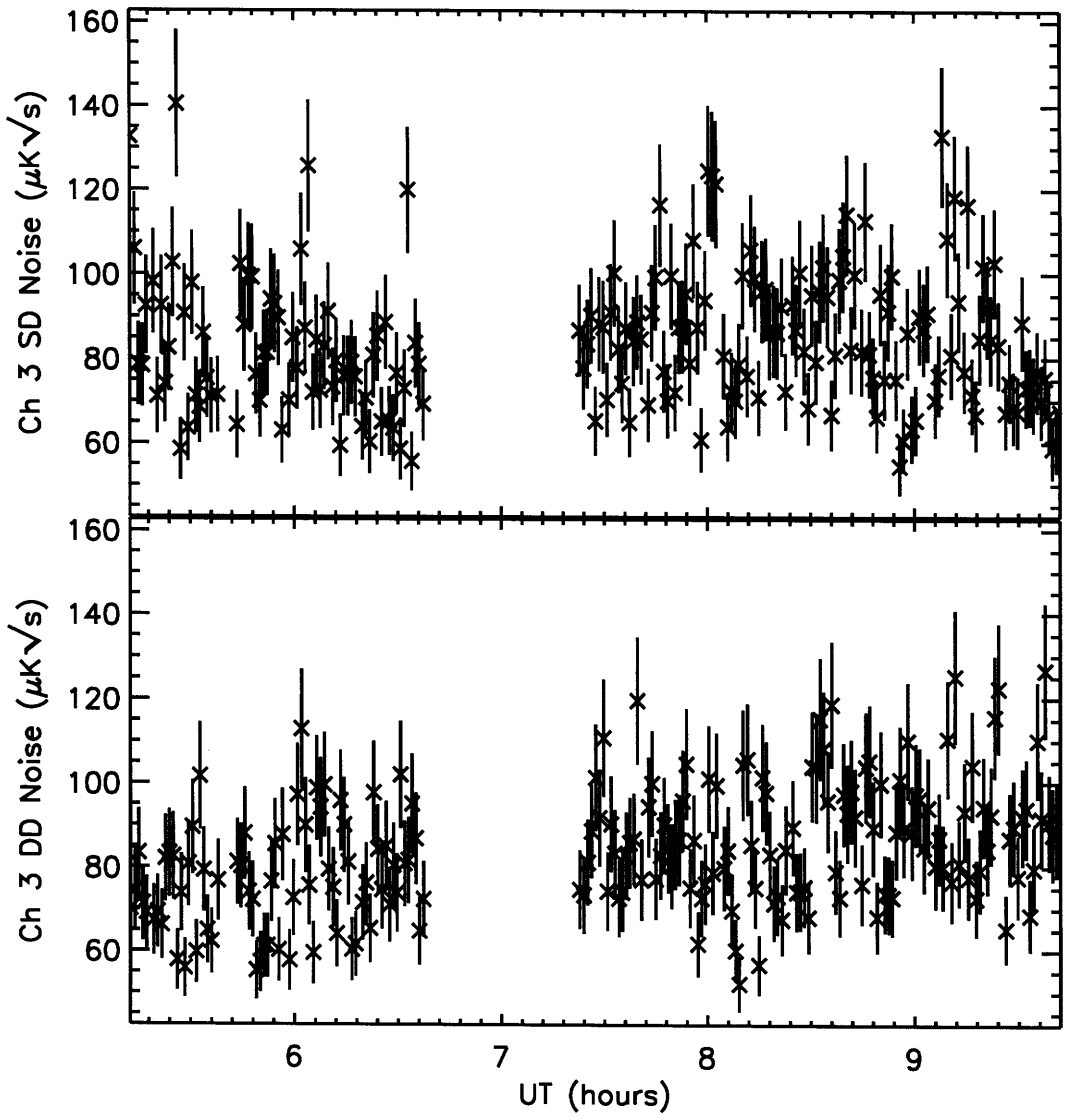

Figure E-3: 1994 Flight noise estimates for each minute of data in $\mu K_{RJ}\sqrt{s}$: Channel 3.

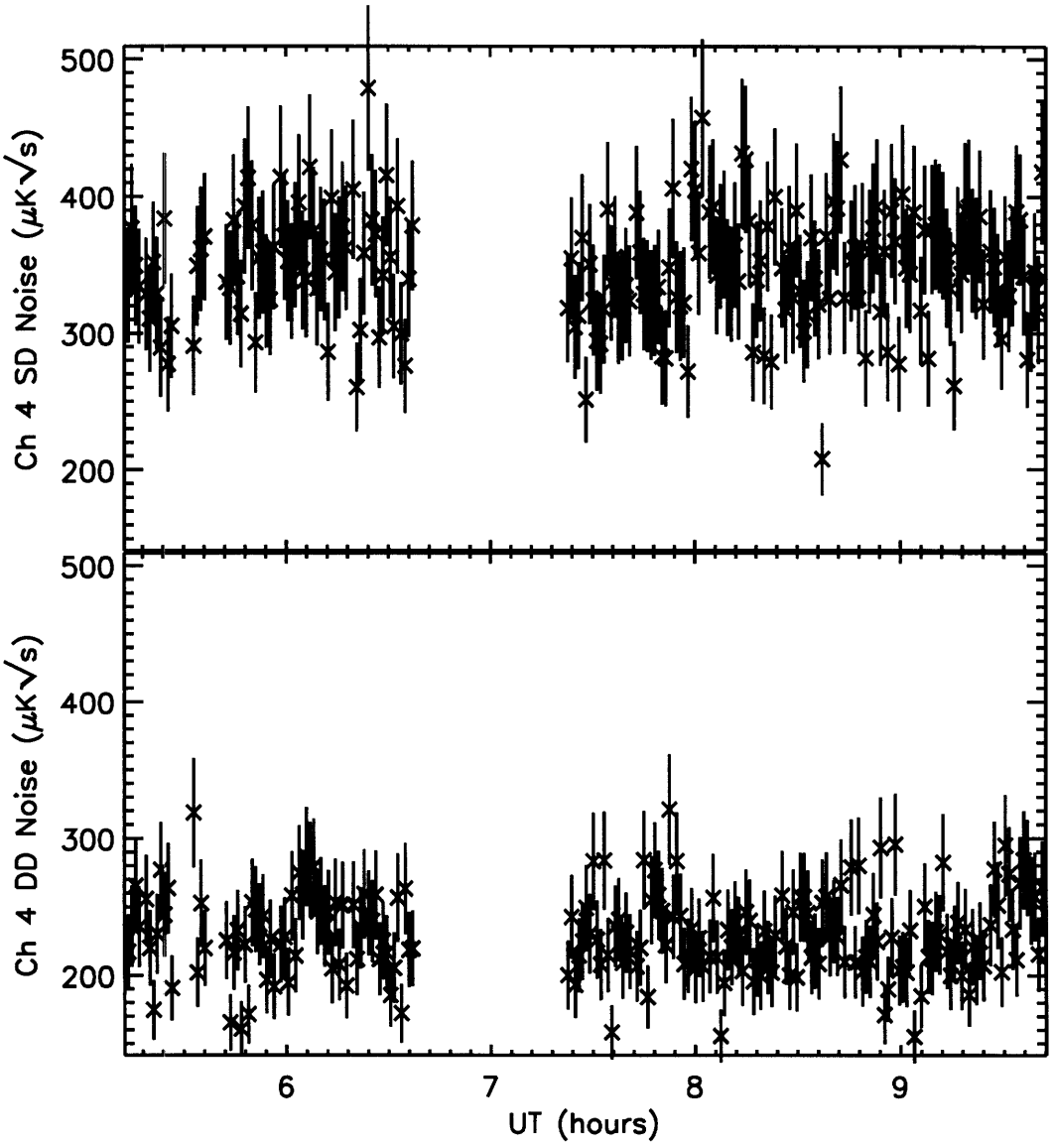

Figure E-4: 1994 Flight noise estimates for each minute of data in $\mu K_{RJ}\sqrt{s}$: Channel 4.

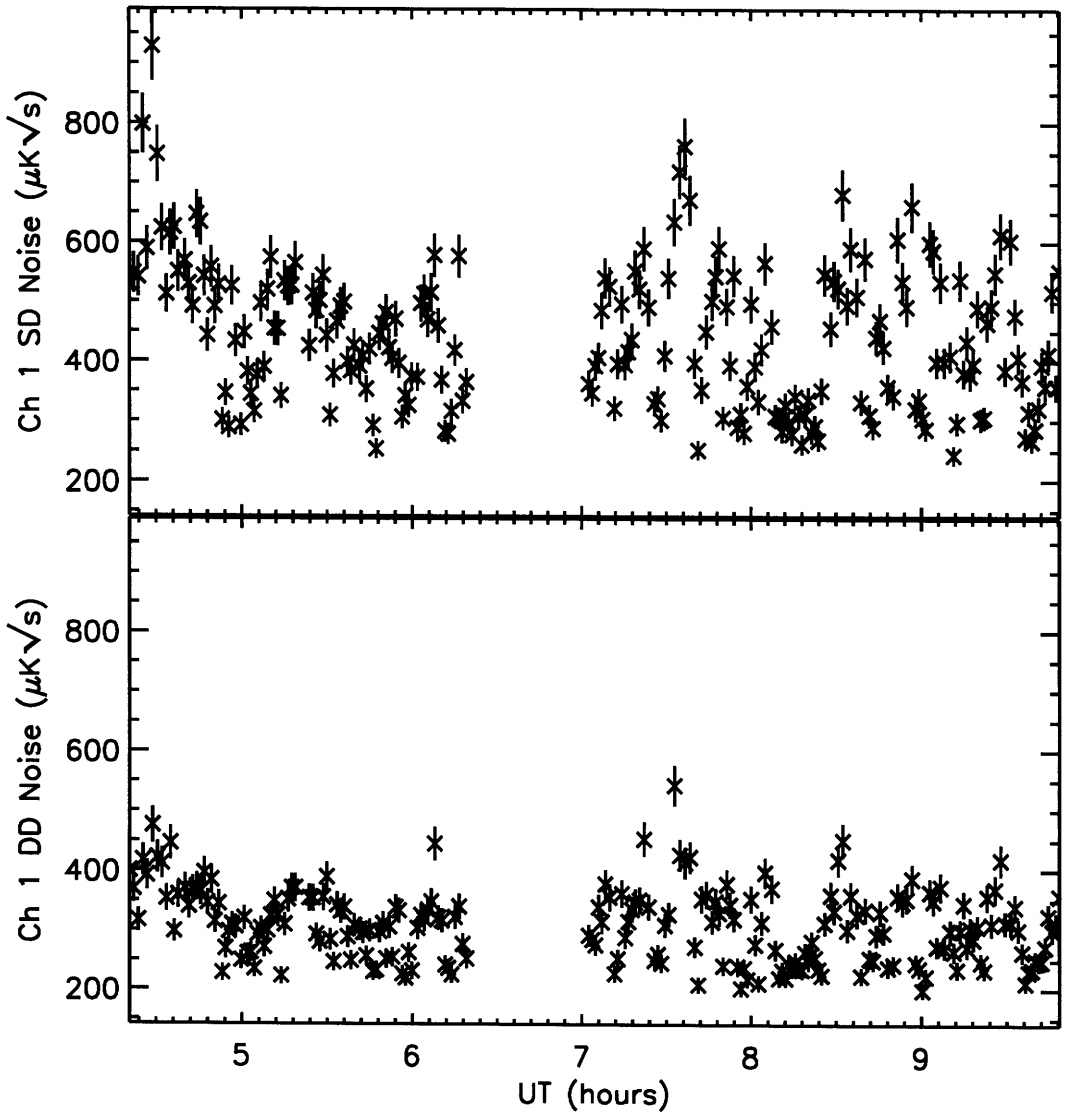

Figure E-5: 1992 Flight noise estimates for each minute of data in $\mu K_{RJ}\sqrt{s}$: Channel 1.

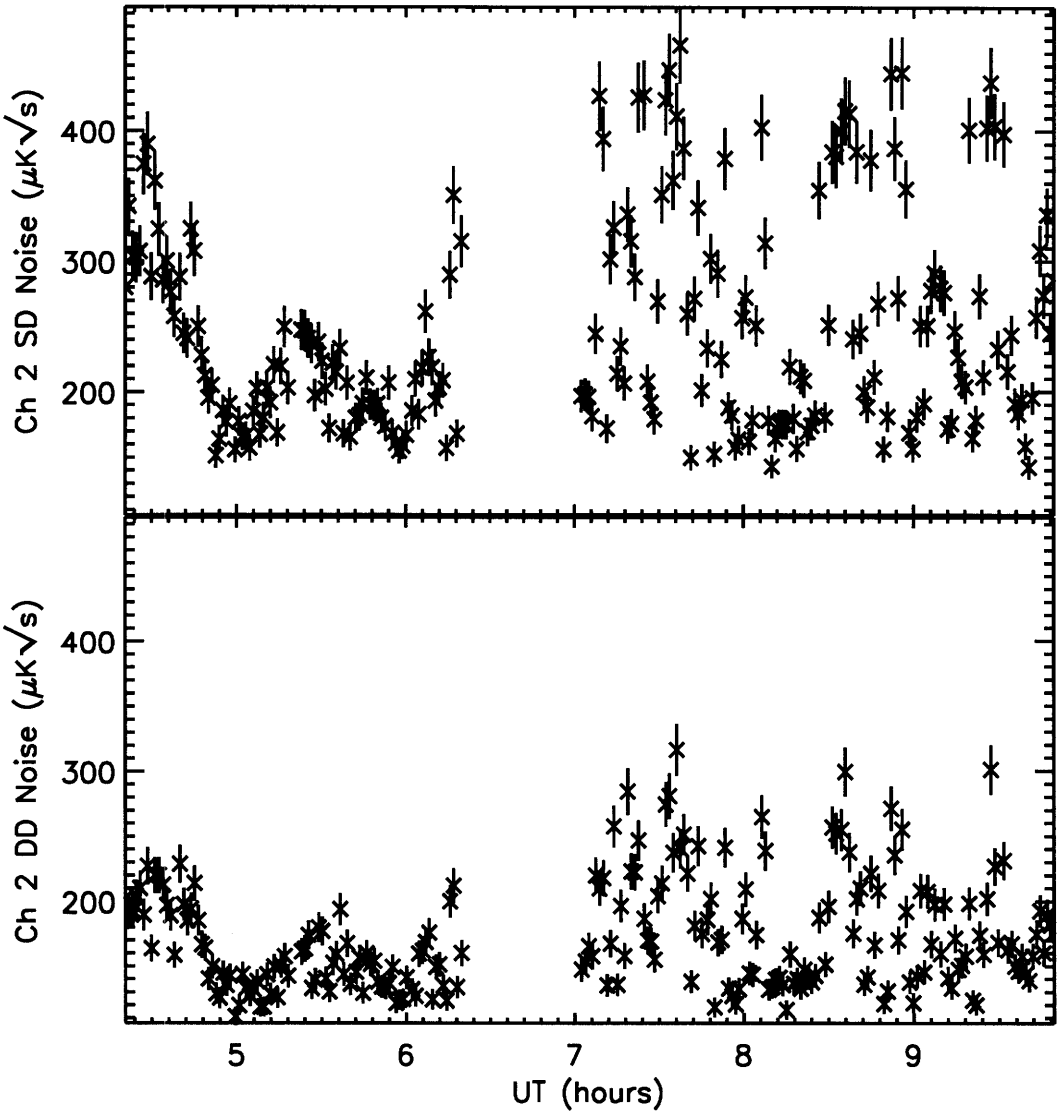

Figure E-6: 1992 Flight noise estimates for each minute of data in $\mu K_{RJ}\sqrt{s}$: Channel 2.

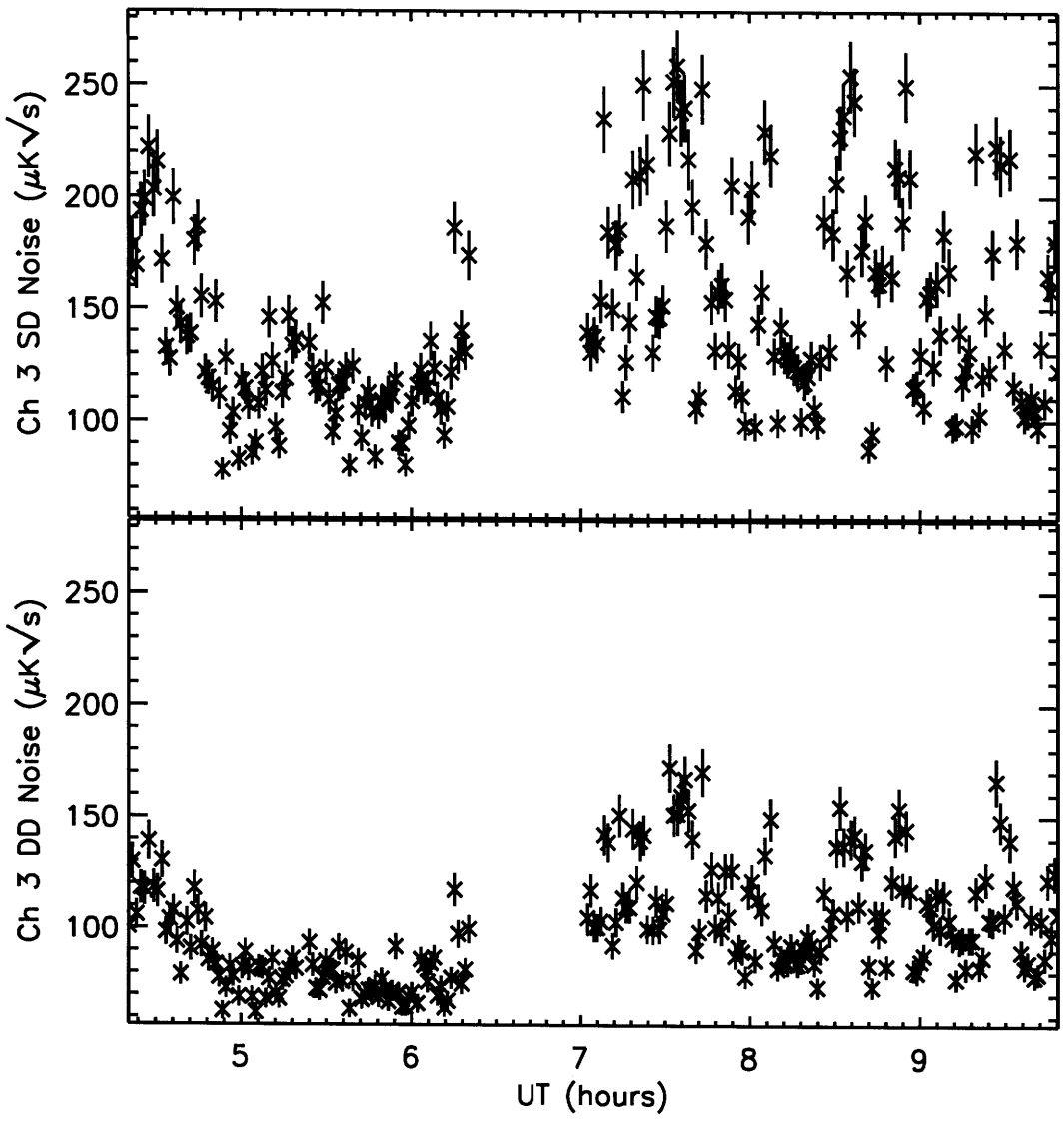

Figure E-7: 1992 Flight noise estimates for each minute of data in $\mu K_{RJ}\sqrt{s}$: Channel 3.

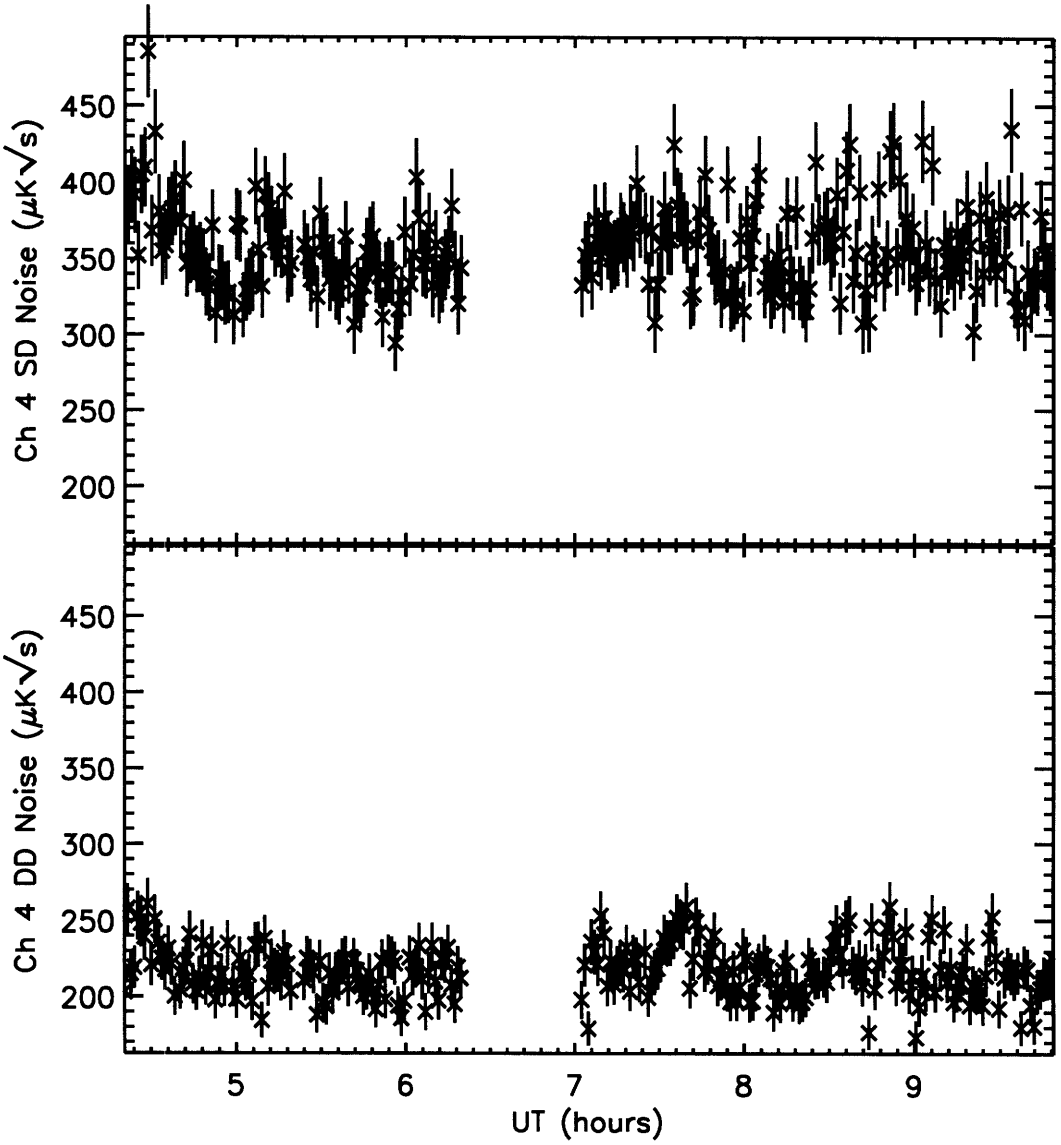

Figure E-8: 1992 Flight noise estimates for each minute of data in $\mu K_{RJ}\sqrt{s}$: Channel 4.

Appendix F

Offset Drifts

The offset drift is found in the simultaneous fit of the data to a model containing sky binned data and drifts in time. The nature of the drift in the 1992 and 1994 flights is described below.

Figure F-1 and F-2 shows the offset drift for all four channels in Raleigh-Jeans (RJ) temperature units, as well as the measured atmospheric pressure at the gondola. The total atmospheric emission in our bands at float altitude is expected to be 20, 60, 400, and 350 mK/mmHg with roughly 30% uncertainty [Page, 1989]. The plots show that the short time scale drifts have the same characteristic $\sim$ 5 minute time scale as the pressure oscillations (caused by altitude oscillations of the balloon, also known as "porposing"). Close inspection shows the phase between the offset drifts and the pressure oscillations wanders substantially. The porposing is a ubiquitous perturbation on the system. It drives swinging motions of several arcminutes amplitude in pitch and roll of the gondola, as well as modulating the total atmospheric column density through which the telescope observes. Distinguishing between these correlated contributions to the offset is complicated. However, because the observed offset drifts scale with wavelength roughly as expected from atmospheric emission, it is likely that the short time scale drifts are dominated by atmosphere. The long time scale drifts do not appear to be correlated with any known effects.

Figure F-3 and F-4 shows the offset drift for all four channels for the 1992 flight. As in the 1994 the porposing is readily apparent. However, in the 1992 flight the solid gondola top diffracted into the beam, having a substantial effect on channel 1. Unlike the 1994 drift, which follows the atmospheric emission frequency dependence, the 1992 drift is roughly constant with radiometer channel. This was a strong motivation to change the top gondola support structure, which was done prior to the flight in 1994 [Fixsen et al., 1996a].

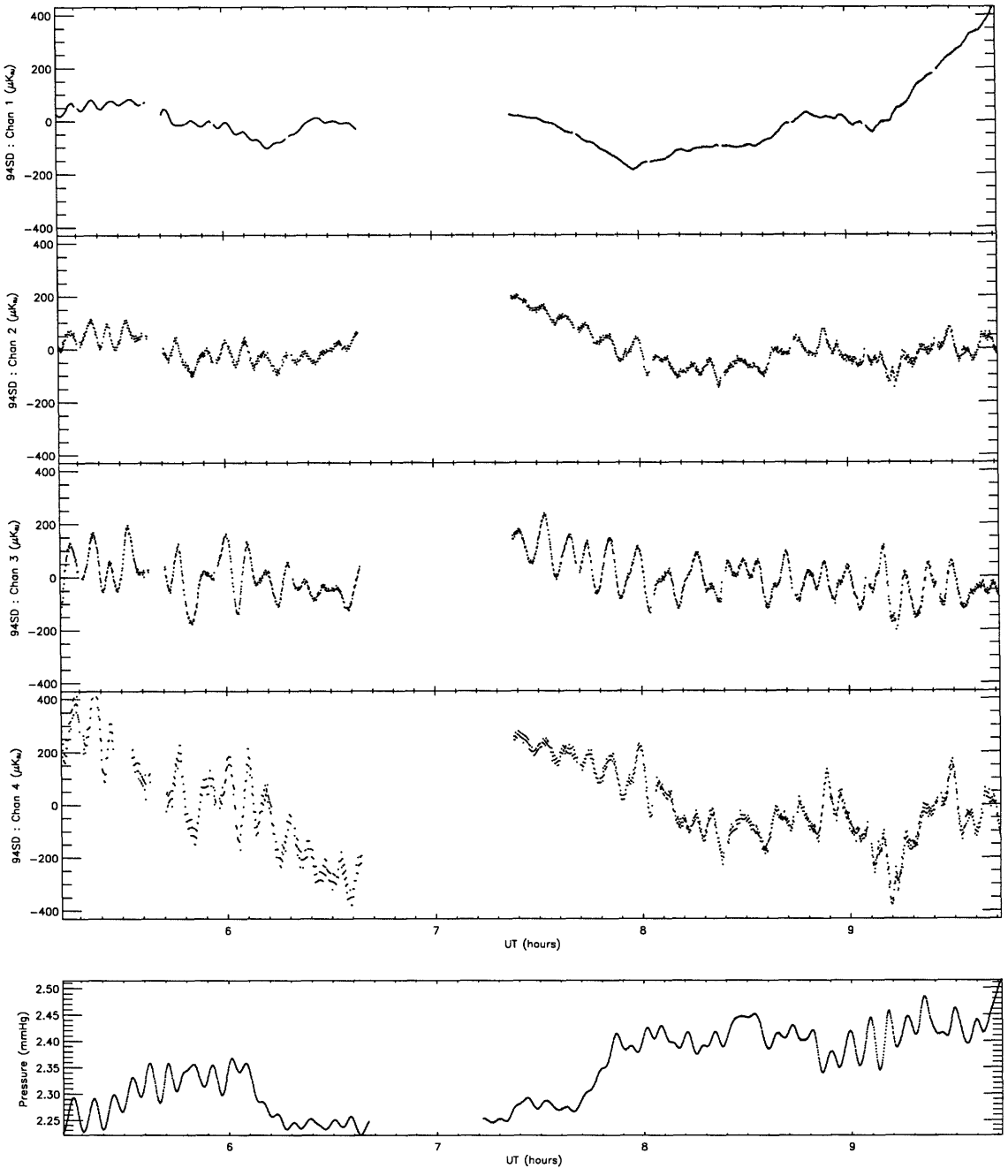

Figure F-1: Single difference offset drift versus time for all channels in μK_{RJ} for the 1994 flight. The atmospheric pressure at the balloon is also plotted. A separate drift is fit for each half flight, from which an average offset is subtracted for this plot.

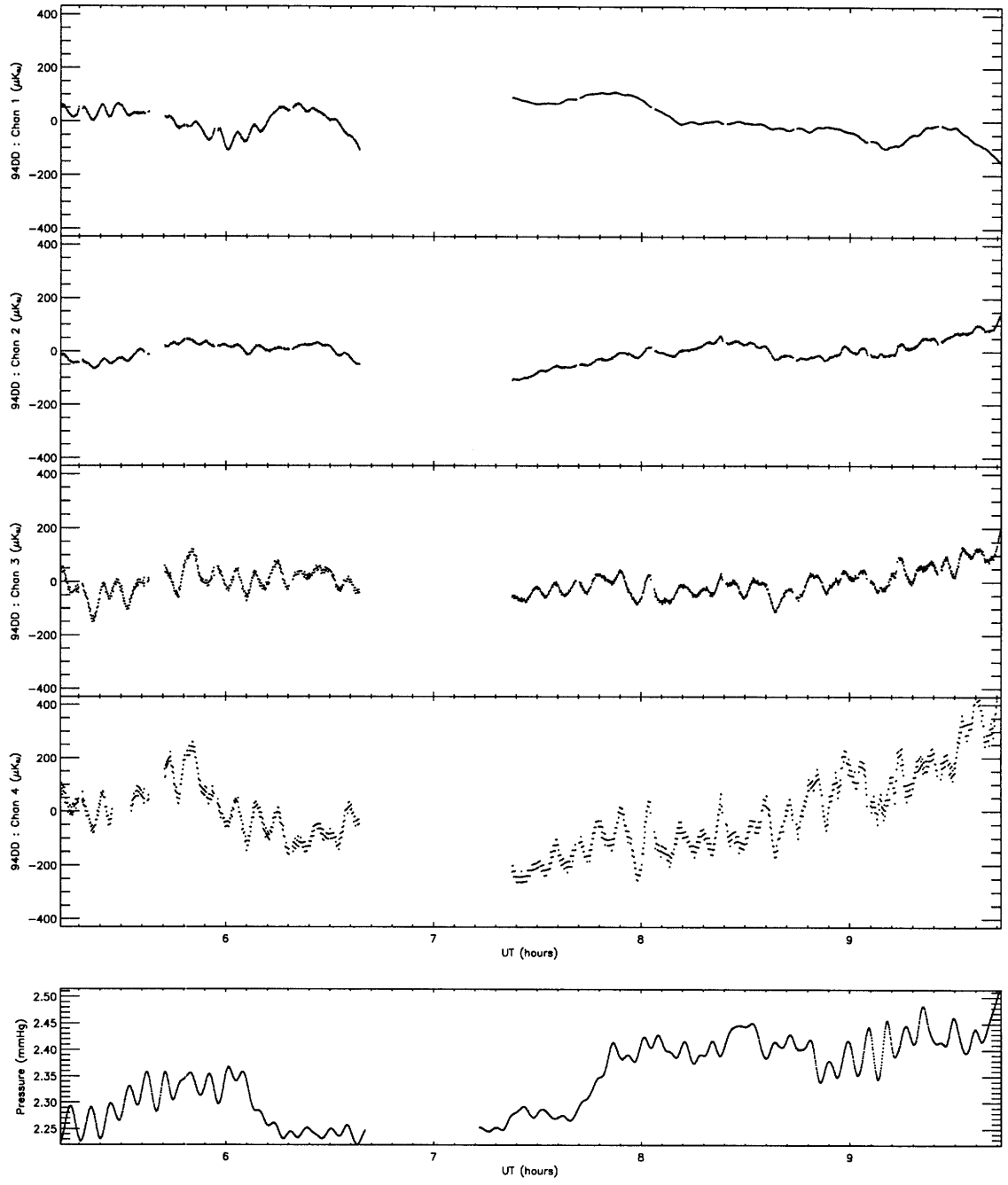

Figure F-2: Double difference offset drift versus time for all channels in μK_{RJ} for the 1994 flight. The atmospheric pressure at the balloon is also plotted. A separate drift is fit for each half flight, from which an average offset is subtracted for this plot.

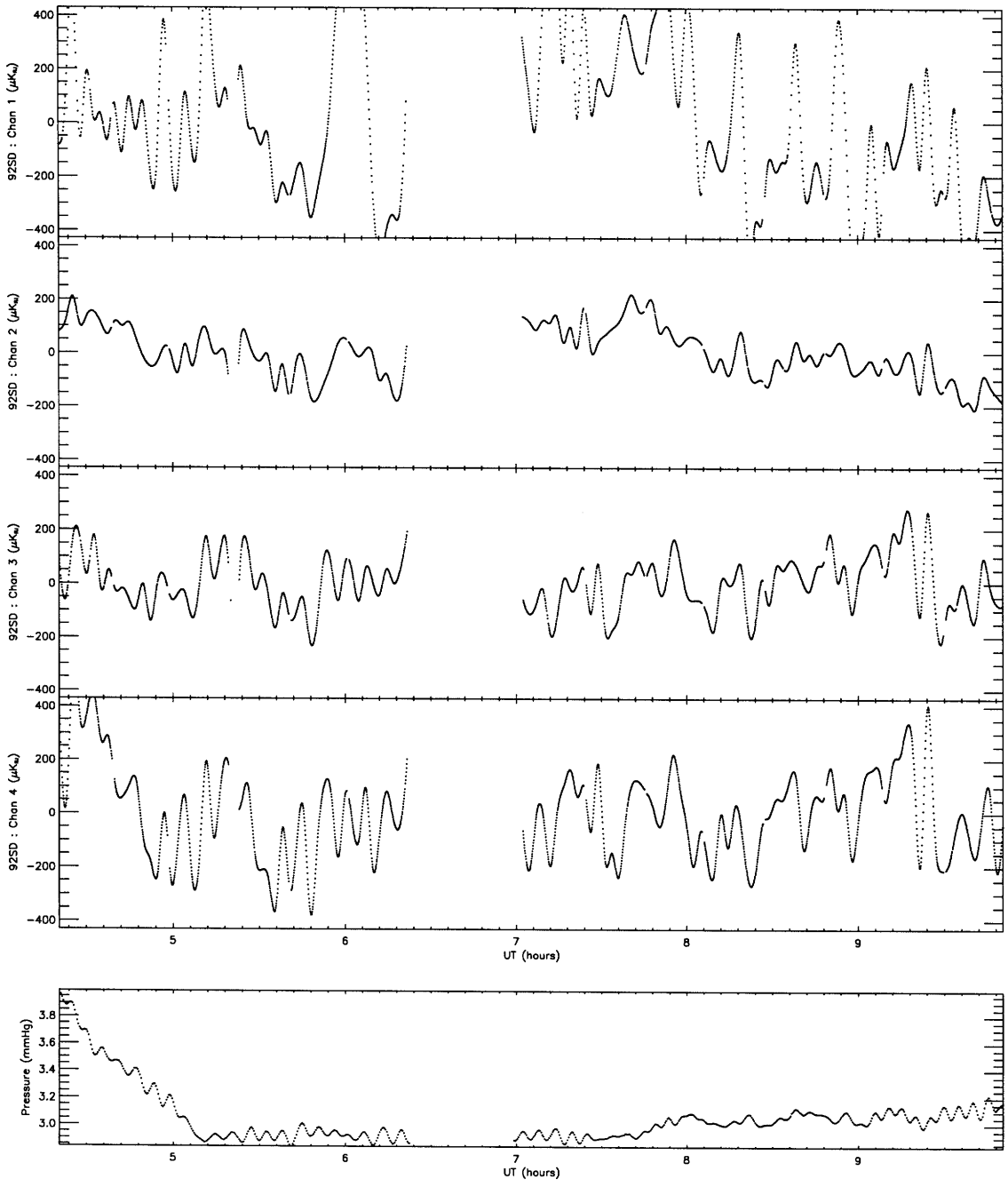

Figure F-3: Single difference offset drift versus time for all channels in μK_{RJ} for the 1992 flight. The atmospheric pressure at the balloon is also plotted. A separate drift is fit for each half flight, from which an average offset is subtracted for this plot.

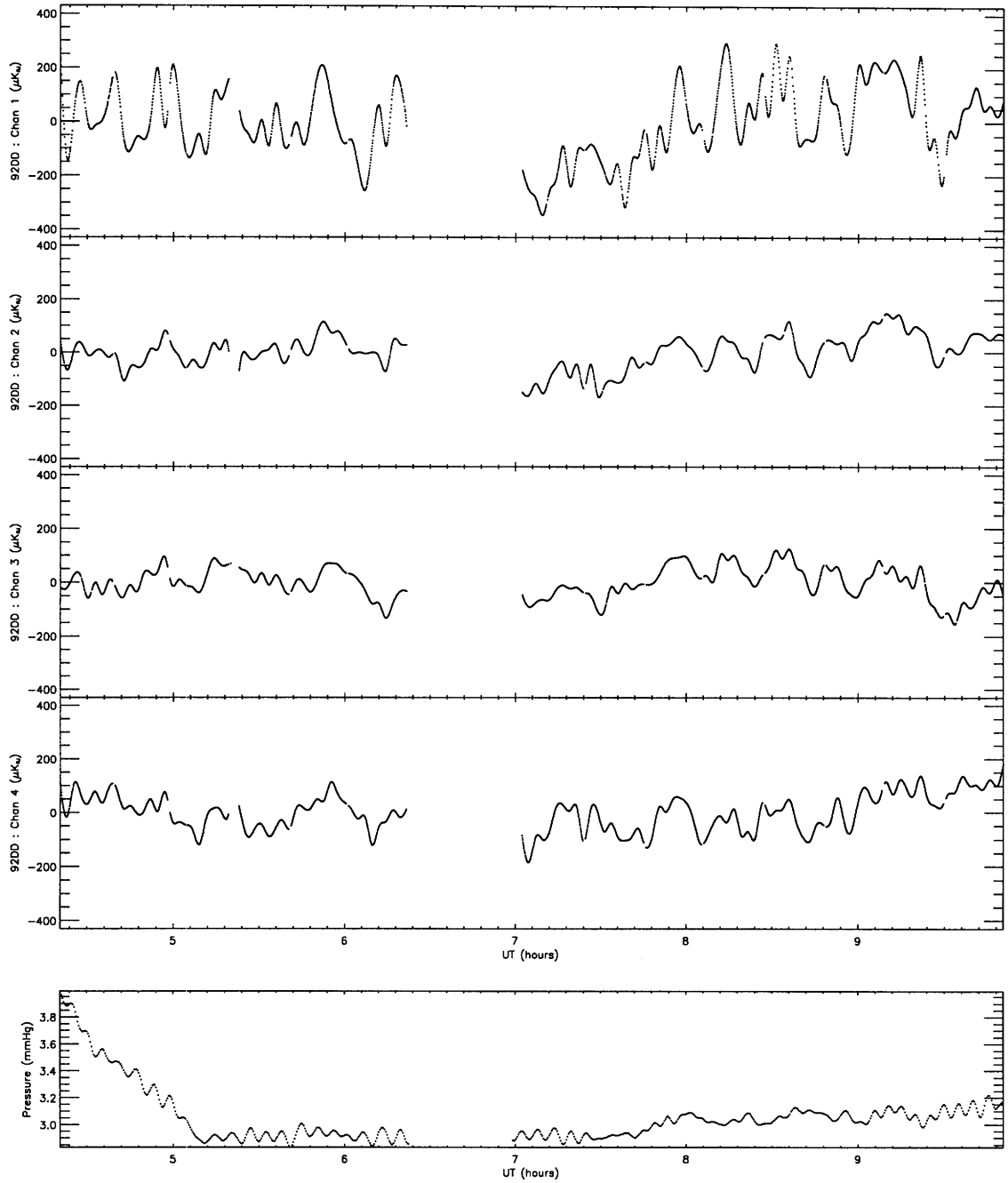

Figure F-4: Double difference offset drift versus time for all channels in μK_{RJ} for the 1992 flight. The atmospheric pressure at the balloon is also plotted. A separate drift is fit for each half flight, from which an average offset is subtracted for this plot.

Appendix G

Plotting Correlated Data

The reduced data have correlated variance. While this is straight-forward to deal with in an analytical sense, it makes simply plotting the data unrepresentative. To demonstrate the problem, I have plotted the dust signal using the square root of the diagonal elements of the covariance matrix as error bars (see Fig. G-1). The on-diagonal errors are much larger than the signal. Another way to look at the signal is to rotate it to the basis in which the errors are diagonal. To do this, start with the covariance of the binned data, V_{ij}, where $i = 1, \ldots, N_{\rm bins}$ and $j = 1, \ldots, N_{\rm bins}$. Because V_{ij} is a symmetric matrix, there exists an orthogonal matrix, $R_{\alpha i}$, which diagonalizes it,

$$\sum_{ij} R_{i\alpha} V_{ij} R_{j\beta} = V_{\alpha\beta} = \sigma_\alpha^2 \delta_{\alpha\beta}$$

The data, D_i, is rotated into this space by multiplying by the rotation matrix, $R_{\alpha i}$, to give

$$D_\alpha = \sum_i R_{\alpha i} D_i.$$

the data in the rotated space. Again $\alpha = 1, \ldots, N_{\rm bins}$, however, while i corresponds to a position on the sky, α does not. D_α are linear combinations of binned sky data and σ_α^2 are the variances on a points D_α. The σ_α^2 are not uniform. In fact, there may be one or two which are a factor of 10 or more larger than the others. This can be understood as the linear combination of sky bins which is known least well.

For the purpose of making representative plots, the highest variance mode is found, ie. where $\sigma^2_{\alpha_{\rm bad}}$ = maximum of σ_α^2. A new data set, $D'_\alpha = D_\alpha$, and associated covariance, $\sigma'^2_\alpha = \sigma_\alpha^2$, are formed. Then the data point corresponding to $\alpha_{\rm bad}$ and its associated variance are both set to zero, ie.

$$\sigma'^2_{\alpha_{\rm bad}} \equiv 0$$

and

$$D'_{\alpha_{\rm bad}} \equiv 0.$$

This edited data is rotated back into the sky bin space.

$$D'_i = \sum_\alpha R_{i\alpha} D'_\alpha$$

The variance on D'_i is given by V'_{ij},

$$V'_{ij} = \sum_{\alpha\beta} R_{\alpha i} {\sigma'_\alpha}^2 \delta_{\alpha\beta} R_{\beta j} \sim \sigma'^2_i \delta_{ij}$$

If this process is to be helpful at all, the V'_{ij} must be approximately diagonal. Plots can now be made of D'_i with errors bars of $\sqrt{V'_{ii}}$.

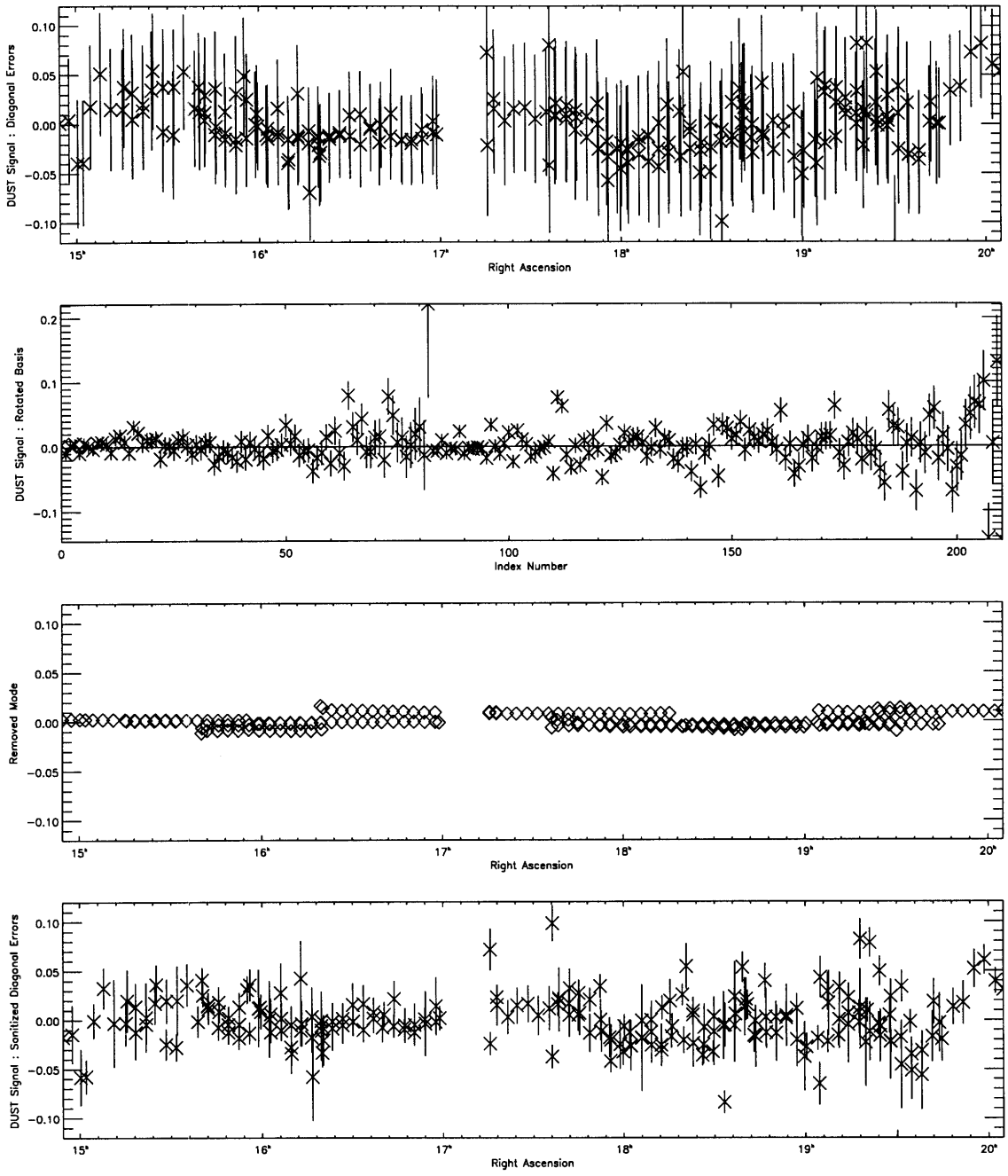

Figure G-1: Plotting correlated data. First the dust signal is plotted using the square root of the diagonal elements of the covariance matrix as error bars. Next the signals are plotted in the rotated space where all errors are diagonal. Next the zeroed mode is shown. Finally the dust signal is plotted after cutting the least well known eigenmode, using the square root of the diagonal elements of new covariance matrix as error bars. This dust signal differs from that in Chapter 4 in that it has not been rebinned in right ascension and declination. The data from the fine bins used in the main analysis is shown here.

Appendix H

Instrument Sensors

MSAM1 has a number of sensors to measure temperatures, pressures, etc. The following table gives a list of those sensors, along with in-flight average, rms, minimum, and maximum values, from a typical period of the flight, between 5:40 and 6:42 hours UT. The "Name" is the telemetry system reference name, and is used to extract the data from the flight archive. In general, temperature signals with names that start with the letter "T" are from Analog Devices AD590 temperature sensors, and those starting with "D" are from temperature sensitive diodes. The letter "V" indicates a voltage monitor, and "I" a current monitor. The letter "G" usually (but not always) starts the name of sensors which are originally in the gondola telemetry stream, and augment the radiometer telemetry stream to create the complete archive.

The sensors signals are divided into 2 broad categories: those associated with the gondola, and those associated with the radiometer. The quantities that are calculated from other sensors, not directly measured, are marked with "*". "Rising" or "falling" in the notes means that the change in the signal over this period of time has a roughly uniform positive or negative slope. "Porp" is short for "porposing," the altitude oscillations that many balloons undergo and a ubiquitous perturbation to the system. Signals dominated by the same characteristic $\sim$ 5 minute time scale oscillations as those seen in pressure sensor, regardless of whether they maintain actual phase coherence with the pressure sensor, are marked with "porp." Some sensors have higher signal-to-noise on the porposing than others. The inclinometer signal, INCLIN, has better than a factor of 10 signal/noise on the porposing, as does the pressure sensor. Other signals which show the porposing, such as the primary mirror thermometers, show it at a low level, and the effect could be caused by electrical pickup, i.e. due to motor currents, rather than directly by the altitude oscillations.

Name	Description	Mean	RMS	Min	Max		notes
Gondola Sensors							
	Position						
RA *	Right Ascension	16.25	.29	15.65	17.0	hr	rising
DEC *	Declination	81.8	.04	81.69	82.07	°	
XLRATE	Gyro cross-el rate	-.007	.04	-.110	.952	°/s	square wave
XLPOS	Gyro cross-el pos	-.742	.7	-2.23	.662	°	3 scans 1°.446 throw
ELRATE	Gyro elev rate	.0298	.003	.0070	.033	°/s	flat
ELPOS	Gyro elev pos	.246	.033	.0395	.308	°	
GAZ*	main magnetometer corrected azimuth	-.48	.6	-2.6	6.75	°	some dropouts
GAZRAW	main magnetometer raw azimuth	352.8	.6	350.9	354.2	°	
ELENC	Elevation encoder	39.74	.06	39.49	39.89	°	like −INCLIN
ELPOT	Elevation pot	39.57	.03	39.35	39.41	°	
GPSLAT	latitude (GPS)	31.70	.015	31.69	31.73	°	1 big jump
GPSLONG	longitude (GPS)	97.9	.19	97.7	98.15	°	updated at camera break
GPSALT	altitude (LORAN)	39.65	.14	39.53	39.82	km	updated at camera break
M1AZ *	sec. magnetometer Az.	-2.67	0.62	-4.82	-1.11	°	like GAZ w/o drops
M1EL *	sec. magnetometer El.	39.2	0.063	38.9	39.5	°	like INCLIN
M1X	sec. magnetometer X	-.26	0.02	-.335	-.206	V	like M1AZ
M1Y	sec. magnetometer Y	-1.02	0.003	-1.04	-1.01	V	like M1AZ
M1Z	sec. magnetometer Z	-4.19	0.002	-4.20	-4.19	V	?
INCLIN	inclinometer output	39.78	.06	39.53	39.94	°	porp

Table H

Name	Description	Mean	RMS	Min	Max	notes
Gondola Sensors (cont.)						
Mirror Temperatures						
TM0	primary mirror 0	-.983	.002	-1.02	-.96	K wandering
TM1	primary mirror 1	-.771	.016	-.793	-.742	K porp
TM2	primary mirror 2	.345	.02	.298	.413	K porp
TM3	primary mirror 3	-.458	.02	-.480	-.421	K porp
TM4	primary mirror 4	-1.11	.02	-1.14	-1.06	K porp
TM5	primary mirror 5	-.845	.066	-.953	-.75	K rising
TM6	primary mirror 6	-1.15	.08	-1.27	-1.02	K rising
TM7	primary mirror 7	-.865	.06	-.963	-.778	K rising
TM8	primary mirror 8	.188	.03	.130	.236	K rising
TM9	primary mirror 9	.373	.03	.323	.418	K rising
TMAVG	Average mirror temp	251.19	.57	250.2	252.1	K falling
TSTRONG	strongback	251.69	.5	250.8	252.59	K tracks TMAVG
TSECMR	secondary mirror right	.299	.02	.244	.335	K broken
TSECAMP	chopper amplifier	290.0	.45	289.1	290.7	K rising
TSECML	secondary mirror left	234.5	.2	234.2	234.8	K wandering
Ground Shield Temperatures						
DRSHLDL	gr. shield rear (left)	230.0	1.0	227.8	231.4	K
TRSHLDR	gr. shield rear (right)	232.4	.99	231.1	233.7	K
TSHLDL	gr. shield (left)	236.2	.2	235.8	236.5	K
TSHLDR	gr. shield (right)	236.2	.17	235.8	236.4	K
Other Temperature Sensors						
GTLELEV	left elev motor	259.66	.94	257.8	261.6	K falling
GTRELEV	right elev motor	260.12	.89	258.4	262.1	K falling
GTMOMW	mom. wheel motor	259.6	.84	257.8	261.3	K falling
GTJITTER	jitter motor	235.4	.83	233.6	236.9	K falling
GTB#1	gondola battery #1	283.6	.68	282.0	285	K rising
GTB#2	gondola battery #2	288.1	1.0	285.8	290	K rising
GTCAMAC	gondola electronics	285.4	.53	284.4	286.5	K rising
TCIDCOMP	CID Computer	499.5	0			K broken
GTGYELEC	gyro electronics	.639	.002	.632	.644	rising

Table H (con't)

Name	Description	Mean	RMS	Min	Max		notes
Gondola Sensors (cont.)							
Temperature Sensors (cont.)							
GTCAMERA	camera	262.2	.62	261.0	263.3	K	rising
GTGYRO	gyro	2.79	.002	2.788	2.796	K	flat
TMAGN	sec. magnetometer	308.3	.38	307.6	308.9	K	falling
Motor Sensors							
VRELMOT	right elev motor V	-.705	.3	-1.79	.348	V	like -INCLIN
IRELMOT	right elev motor I	-.565	.27	-1.30	.386	A	like -INCLIN
VLELMOT	left elev motor V	-.643	.29	-1.42	.247	V	like -INCLIN
ILELMOT	left elev motor I	-.453	.23	-.970	.249	A	like -INCLIN
VMWMOT	azimuth wheel motor V	-.829	.25	-1.75	.46	V	spikes at turnaround
IMWMOT	azimuth wheel motor I	-.717	.2	-1.5	.23	A	spikes at turnaround
VDITHMOT	dither (jitter) motor V	0.337	0.78	-1.85	1.19	V	
IDITHMOT	dither (jitter) motor I	0.057	0.10	-0.24	0.18	A	
Other Sensors							
MWPOS	azimuth wheel position	359.59	0				broken
MWVEL	azimuth wheel velocity	.284	.02	-.055	.85	rpm	looks like az
DITHERR	dither (jitter) error	-.045	.02	-.105	.033		
DITHTACH	dither (jitter) tach.	-.045	.02	-.138	.053		
PHI	high range pressure	1.698	.04	1.641	1.775	mmHg	porp
PLO	low range pressure	2.293	.04	2.228	2.371	mmHg	porp
SPLO	super low pressure	2.287	.05	2.22	2.37	mmHg	porp
SECAMP	sec. mirror chop amplitude	.6072	.0001	.6069	.6076	°	flat
SECOFF	sec. mirror chop offset	.001	.0001	.0008	.0013	°	flat
SECPOS	sec. mirror position	-.0012	.0001	-.0017	-.0009	°	
CMDAMP	commanded sec. amp.	.6108	.000	.6105	.6109	°	flat
CMDOFF	commanded sec. offset	-.0003	.000	-.0004	-.0001	°	flat
TCF1	CFRP sample 1	225.3	.53	224.2	226.5	K	porp
TCF2	CFRP sample 2	219.55	.35	218.7	220.3	K	porp
TCF3	CFRP sample 3	223.35	.50	222.2	224.4	K	porp
TCF4	CFRP sample 4	221.9	.56	220.7	222.9	K	porp

Table H (con't)

Name	Description	Mean	RMS	Min	Max	notes
Gondola Sensors (cont.)						
Other Sensors (cont.)						
GGYXTRIM	GSFC Gyro X trim	-2.274	.01	-2.297	-2.26	changed once middle of scan
GGYYTRIM	GSFC Gyro Y trim	1.525	.01	1.507	1.535	changed once middle of scan
Gondola Electronics Sensors						
Voltage and Current Monitors						
GB#1	gondola battery #1 V	31.13	.02	31.07	31.19 V	
GB#2	gondola battery #2 V	21.51	.05	21.39	21.63 V	
G+5#1	gondola +5 #1 V	4.91	.006	4.90	4.92 V	
G+5#2	gondola +5 #2 V	4.925	.006	4.910	4.937 V	
G+15	gondola +15 V	14.66	.01	14.63	14.68 V	
G-15	gondola -15 V	-15.18	.01	-15.21	-15.16 V	
GIB#1	gondola batt #1 I	7.46	.04	7.36	7.55 A	
GIB#2	gondola batt #2 I	1.095	.14	.867	1.44 A	
GIHEAT	gondola electronics heater I	4.156	.02	4.08	4.21 A	
GI+5#1	gondola +5 #1 I	4.93	.07	4.73	5.11 A	
GI+5#2	gondola +5 #2 I	5.03	.08	4.84	5.19 A	
GI+15	gondola +15 I	1.30	.003	1.297	1.31 A	
GI-15	gondola -15 I	-1.17	.004	-1.178	-1.16 A	
GGY+/-15	gondola Gyro +/-15 V	2.479	.002	2.474	2.482	
GGY+/-25	gondola Gyro +/-25 V	2.604	.002	2.599	2.610	
GGY+28	gondola Gyro +28 V	31.45	.02	31.40	31.51 V	
GIGY+28	gondola Gyro +28 I	.42	.5	.331	.513	
GIGYHEAT	gondola Gyro heater I	2.672	.1	2.459	2.824	

Table H (con't)

Name	Description	Mean	RMS	Min	Max		notes
Radiometer Sensors							
Temperature Sensors							
DZEOL	zeolite diode	4.62	.006	4.60	4.63	K	flat
DINTPRE	internal preamp diode	80.39	0.25	79.7	81.15	K	flat
DMD	main LHe dewar diode	4.11	.008	4.09	4.13	K	flat
DHORN	internal horn diode	6.05	0.02	6.00	6.10	K	
DTHROAT	horn throat diode	4.74	0.02	4.69	4.79	K	
DSHUT	external shutter diode	128.8	0.6	126.9	130.3	K	
GID	internal dewar GRT	.2505	.000	.2503	.2509	K	slow falling
Signal Sensors							
C1DC	Channel 1 DC Level	.334	.000	329.2	334.8	V	rising
C2DC	Channel 2 DC Level	.575	.000	.5753	.5761	V	rising
C3DC	Channel 3 DC Level	.2764	.0001	.2762	.2766	V	rising
C4DC	Channel 4 DC Level	.09946	.000	.09936	.09952	V	rising
C1GAIN	channel 1 signal gain	512	0	512	512		flat
C1PHASE	channel 1 phase delay	0					
C2GAIN	channel 2 signal gain	512					
C2PHASE	channel 2 phase delay	0					
C3GAIN	channel 3 signal gain	128					
C3PHASE	channel 3 phase delay	0					
C4GAIN	channel 4 signal gain	1024					
C4PHASE	channel 4 phase delay	0					
Other Sensors							
HELEVEL	Helium level sensor	37				%	end of flight value
Radiometer Electronics Sensors							
Voltage Sensors							
B+30	+30 Volt battery	32.43	.03	32.37	32.48	V	falling
V+15	+15 Volt supply	15.17	.003	15.16	15.17	V	flat
V-15	-15 Volt supply	-14.96	.004	-14.97	-14.95	V	flat
V+12A	+12 Volt A-side supply	12.08	.002	12.08	12.09	V	flat
V-12A	-12 Volt A-side supply	-12.13	.003	-12.13	-12.12	V	flat
V+12B	+12 Volt B-side supply	12.00	.002	11.99	12.00	V	flat
V-12B	-12 Volt B-side supply	-11.87	.002	-11.87	-11.87	V	flat
V+12D	+12 Volt digital supply	11.83	.002	11.82	11.83	V	flat

Table H (con't)

Name	Description	Mean	RMS	Min	Max	notes
Radiometer Electronics (cont.)						
Voltage Sensors (cont.)						
VHINTPRE	internal preamp heater	3.747	.002	3.74	3.756 V	flat
VHEXTPRE	external preamp heater	9.76	.02	9.72	9.81 V	wandering
BHEATER	heater battery voltage	13.25	.002	13.24	13.26 V	flat
BMOTOR	motor battery voltage	13.27	.003	12.26	13.27 V	flat
VHMEB	MEB heater	.0061	.0006	.0004	.0007 V	flat
VHMAGN	sec. magnetometer heater	.009	.0006	.007	.01 V	flat
VSHUT	external shutter motor control	.0104	.0005	.0085	.012 V	flat
VSHUTDIR	external shutter setting	13.25	.0009	13.21	13.27 V	flat
Temperature Sensors						
TPOWER	Powercube temperature	320.31	.4	319.7	321.0 K	falling
TCAGEA	MEB A-side cage	306.3	.4	305.6	307.0 K	falling
TCAGEB	MEB B-side cage	310.25	.003	309.6	310.8 K	falling
TBATT	battery box	283.6	.14	283.4	283.9 K	falling
TEXTPRE	external preamp	298.7	.00	298.6	298.7 K	flat

Table H (con't)

Appendix I

GSE

There is a flight sequence table composed of a series of addresses, or "slots," to operate the gondola. These contain instructions on what operation the gondola should be executing. Once the gondola is finished executing the instruction in one slot, it continues by executing the function in the following slot. The software can also be instructed to abort its current instruction, and go to a specified slot. The gondola primitives are not well suited to this experiment and the command up-link is unreliable, so great care was taken in making up the following flight table.

The following table give the layout of the flight slot table, which is burned into a programmable read-only memory (PROM) device. The flight computer reads the PROM each time it is rebooted. The gondola is pointed in absolute coordinates. Some slots contain parameters, typically azimuth (AZ) and elevation (EL), which must be updated in-flight. All the words of a given slot prior to the parameter must be reloaded. The principal functions of the gondola are grouped together in command sets, usually separated with an idle, and are listed in bold in the Table I. Typing the name shown in bold at the gondola control computer will reload all the slots associated with that name. "Ty" is a command type. Times are specified in 0.1 second units. Locations are specified in bits, where 1 bit = 0.′3296. Rates are specified in bits, 1 bit = 0.′3296 per second.

The following are the main command sets for the gondola.

FLINIT The command set to start taking control of the gondola. It has the gondola "origin" (Command Ty 14), that is use the current values of the azimuth and elevation sensors as the commanded azimuth and elevation. The elevation control is started. The telescope is commanded to move (Command Ty 06) to elevation of 30°. The azimuth control is started, and then the telescope "idles", sits still (Command Ty 07).

TMMV The set to make a move to a position AZ,EL in 1 second, and then idle. This is useful for making very small moves. Because of rounding errors in the flight software, making very small moves at a finite rate causes unpredictable behavior in the gondola.

MOVE This is the normal movement command set. The telescope moves to AZ,EL @ 2.8 °/s and then idles.

RAST This command set performs a "raster," a series of NS horizontal scans, RA in width, uniformly spaced in elevation, covering RE in elevation. There is a built in raster (Command Tp 05), but it starts this raster from where it is currently located. This RAST command set moves half the width of the raster to the left, and then half the height of the raster up, begins the raster, and once finished, moves back to the starting point, finally ending with an idle.

ELEV This set scans the telescope in elevation, from 5°.5 to 39°.9 at 0°.76/s repeatedly, by moving down to 5°.5, moving up to 39°.9 and then "jumping" (Command Tp 10) back to the original slot (move to 5°.5).

SCNA or SCNB This set is used to execute the scan, the principal element of the observing strategy. It has the telescope moving to the right most side of the scan, then moving to the left most side of the scan, then jumping back to the first move to the right. As discussed in Chapter 3 the scan must be stopped roughly every 20 minutes to take a camera picture. To stop, a command is sent overwriting the jump back at the beginning of the scan, with a jump to the next slot. Already in place in this slot is an idle for PO (typically 60) seconds, long enough to get a good camera picture. After this, the telescope jumps to the beginning of the next scan, the coordinates of which have been previously loaded into the other set of scan slots (A or B).

SPIN This set spins the gondola in azimuth. This is done by commanding the gondola to move in a series of three consecutive steps, each of 120°. This is repeated indefinitely.

Command	kdB#	TpSl	Word3	Word4	Word5	Word6	Word7
FLINIT - load stuff to flight table							
origin in acq. mode; turn on el servo	0408	1402	0C01	FAF3			
move to el=30°, @ 1°/s	040C	0603	4000	1555	00B6	FAF3	
idle	040C	0704	0000	0000	0400	FAF3	
origin in acq. mode, both servo on	0408	1405	0F01	FAF3			
idle	040C	0706	0000	0000	0400	FAF3	
origin in acq mode, no change serv	040C	1407	0001	FAF3			
idle	040C	0708	0000	0000	0400	FAF3	
FLTMMV - full load move in 1s							
origin in acq mode	0408	1409	OF01	FAF3			
move to AZ,EL in 1 sec	040E	060A	AZ	EL	0000	000A	FAF3
idle	040C	070B	0000	0000	0400	FAF3	
FLMOVE - full load move @ 2.8 sec							
origin in acq. mode; servos on	0408	140C	OF01	FAF3			
move to a AZ,EL @ 2.8 °/s	040C	060D	AZ	EL	00B6	FAF3	
idle	040C	070E	0000	0000	0400	FAF3	
FLRAST - full load paramaterized raster							
move to A0,EL @ RR rate	040C	060F	A0	EL	RR	FAF3	
move to A0,E0 @ RR rate	040C	0610	A0	E0	RR	FAF3	
raster w/ RR rate & NS scans	040E	0511	RA	RE	RN	0000	FAF3
move to A1,EL @ RR rate	040C	0612	A1	EL	RR	FAF3	
move to AZ,EL @ RR rate	040C	0613	AZ	EL	RR	FAF3	
idle	040C	0714	0000	0000	0400	FAF3	
FLELEV - full load of elevation scan							
move to AZ,5.5 @.76°/s	040C	0615	AZ	03E9	008A	FAF3	
move to AZ,39.9 @.76°/s	040C	0616	AZ	1C5E	008A	FAF3	
jump to slot 15	0408	1017	0015	FAF3			
FLFSMV - full load of fast move							
origin in acq. mode; both serv. on	0408	1418	OF01	FAF3			
move to a AZ,EL @ 2°8/s	040C	0619	AZ	EL	016C	FAF3	
idle	040C	071A	0000	0000	0400	FAF3	
UNUSED		1B					
UNUSED		1C					
UNUSED		1D					
UNUSED		1E					
UNUSED		1F					

Table I

Command	kdB#	TpSl	Word3	Word4	Word5	Word6	Word7
FLNODA - full load 4s noda							
move to AZ,EL in 4s	040E	0620	AZ,EL	0000	0028	FAF3	
idle for 26 sec	040C	0721	0230	0000	0400	FAF3	
move to AL,EL in 4sec	040E	0622	AL	EL	0000	0028	FAF3
idle for 26 sec	040C	0723	0230	0000	0400	FAF3	
move to AZ,EL in 4sec	040E	0624	AZ	EL	0000	0028	FAF3
idle for 26 sec	040C	0725	0230	0000	0400	FAF3	
move to AR,EL in 4sec	040E	0626	AR	EL	0000	0028	FAF3
idle for 26 sec	040C	0727	0230	0000	0400	FAF3	
goto slot 20	0408	1028	0020	FAF3			
FLNODB - full load 4s nodb							
move to AZ,EL in 4sec	040E	0629	AZ	EL	0000	0028	FAF3
idle for 26 sec	040C	072A	0230	0000	0400	FAF3	
move to AL,EL in 4sec	040E	062B	AL	EL	0000	0028	FAF3
idle for 26 sec	040C	072C	0230	0000	0400	FAF3	
move to AZ,EL in 4sec	040E	062D	AZ	EL	0000	0028	FAF3
idle for 26 sec	040C	072E	0230	0000	0400	FAF3	
move to AR,EL in 4sec	040E	062F	AR	EL	0000	0028	FAF3
idle for 26 sec	040C	0730	0230	0000	0400	FAF3	
goto slot 29	0408	1031	0029	FAF3			
UNUSED		32					
FLSCNA - full load of scan A							
move to AL,EL in 60s	040C	0633	AL	EL	0008	FAF3	
move to AR,EL @ 1.'32/s	040C	0634	AR	EL	0008	FAF3	
jump to slot 33	0408	1035	0033	FAF3			
idle for 60s	040C	0736	PO	0000	0400	FAF3	
jump to slot 38	0408	1037	0038	FAF3			
FLSCNB - full load of scan B							
move to AL,EL in 60s	040C	0638	AL	EL	0008	FAF3	
move to AR,EL @ 1.'32/s	040C	0639	AR	EL	0008	FAF3	
jump to slot 38	0408	103A	0038	FAF3			
idle for 60s	040C	073B	PO	0000	0400	FAF3	
jump to slot 33	0408	103C	0033	FAF3			
UNUSED		3D					
UNUSED		3E					
UNUSED		3F					

Table I (con't)

Command	kdB#	TpSl	Word3	Word4	Word5	Word6	Word7
UNUSED		40					
UNUSED		41					
UNUSED		42					
FLSPIN - full load							
origin in acq. mode	0408	1443	0001	FAF3			
move to 0,EL @ 1°/s	040C	0644	0000	EL	00B6	FAF3	
move to 135,EL @ 1°/s	040C	0645	6000	EL	00B6	FAF3	
move to 270,EL @ 1°/s	040C	0646	C000	EL	00B6	FAF3	
jump to slot 44	0408	1047	0044	FAF3			
UNUSED		48					
UNUSED		49					
UNUSED		4A					

Table I (con't)

Bibliography

[Bennett et al., 1994] Bennett, C. L., Kogut, A., Hinshaw, G., Banday, A. J., Wright, E. L., Górski, K. M., Wilkinson, D. T., Weiss, R., Smoot, G. F., Meyer, S. S., Mather, J. C., Lubin, P., Loewenstein, K., Lineweaver, C., Keegstra, P., Kaita, E., Jackson, P. D., and Cheng, E. S. (1994). Cosmic temperature fluctuations from two years of *cobe* differential microwave radiometers observations. ApJ, 436:423.

[Bennett et al., 1992] Bennett, C. L., Smoot, G. F., Hinshaw, G., Wright, E. L., Kogut, A., Amici, G. D., Meyer, S. S., Weiss, R., Wilkinson, D. T., Gulkis, S., Janssen, M., Boggess, N. W., Cheng, E. S., Hauser, M. G., Kelsall, T., Mather, J. C., Moseley, S. H., Murdock, T. L., and Silverberg, R. F. (1992). Preliminary separation of galactic and cosmic microwave emission for the *cobe* differential microwave radiometers. ApJ, 396:L7.

[Charakhch'yan et al., 1978] Charakhch'yan, A. N., Bazilevskaya, G. A., Stozhkov, Y. I., and Charakhch'yan, T. N. (1978). Cosmic rays in the stratosphere and in near space during solar activity cycles 19 and 20. In Basov, N. G., editor, *Cosmic Rays in the Stratosphere and in Near Space*, volume 88 of *Proceedings of the P. N. Lebedev Physics Institute*, page 1, New York. Consultants Bureau.

[Cheng, 1994] Cheng, E. S. (1994). The msam/tophat program for measuring the cmbr anisotropy. In Sanz, J. L. et al., editors, *Present and Future of the Cosmic Microwave Background*, volume 429 of *Lecture Notes in Physics*, page 76, New York. Springer-Verlag.

[Cheng et al., 1996] Cheng, E. S., Cottingham, D. A., Fixsen, D. J., Inman, C. A., Kowitt, M. S., Meyer, S. S., Page, L. A., Puchalla, J. L., Ruhl, J. E., and Silverberg, R. F. (1996). Msam1-94: Repeated measurement of medium-scale anisotropy in the cosmic microwave background radiation. ApJ, 456:L71.

[Cheng et al., 1994] Cheng, E. S., Cottingham, D. A., Fixsen, D. J., Inman, C. A., Kowitt, M. S., Meyer, S. S., Page, L. A., Puchalla, J. L., and Silverberg, R. F.

(1994). A measurement of the medium-scale anisotropy in the cosmic microwave background radiation. ApJ, 422:L37.

[Downey et al., 1984] Downey, P. M., Jeffries, A. D., Meyer, S. S., Weiss, R., Bachner, F. J., Donnelly, J. P., Lindley, W. T., Mountain, R. W., and Silversmith, D. J. (1984). Monolithic silicon bolometers. Appl. Opt., 23:910.

[Fixsen et al., 1996a] Fixsen, D. J., Cheng, E. S., Cottingham, D. A., Folz, W. C., Inman, C. A., Kowitt, M. S., Meyer, S. S., Page, L. A., Puchalla, J. L., Ruhl, J. E., and Silverberg, R. F. (1996a). A balloon-borne millimeter-wave telescope for cosmic microwave backround anisotropy measurements. ApJ. submitted, preprint `astro-ph/9512006`.

[Fixsen et al., 1996b] Fixsen, D. J., Cheng, E. S., Gales, J. M., Mather, J. C., Shafer, R. A., and Wright, E. L. (1996b). The cosmic microwave background spectrum form the full *cobe firas* data set. ApJ. submitted.

[Franceschini et al., 1989] Franceschini, A., Toffolatti, L., Danese, L., and De Zotti, G. (1989). Discrete source contributions to small-scale anisotropies of the microwave background. ApJ, 344:35.

[Ganga et al., 1993] Ganga, K., Cheng, E., Meyer, S., and Page, L. (1993). Cross-correlation between the 170 ghz survey map and the cobe differential microwave radiometer first-year maps. ApJ, 410:L57.

[Ganga et al., 1994] Ganga, K., Page, L., Cheng, E., and Meyer, S. (1994). The amplitude and spectral index of the large angular scale anisotropy in the cosmic microwave background. ApJ, 432:L15.

[Gaustad et al., 1995] Gaustad, J. E., Oh, E. S., McCullough, P. M., and van Buren, D. (1995). An upper limit on galactic free-free emission near the north celestial pole. BAAS, 27:823.

[Griffin et al., 1986] Griffin, M. J., Ade, P. A. R., Orton, G. S., Robson, E. I., Gear, W. K., Nolt, I. G., and Radostitz, J. V. (1986). Submillimeter and millimeter observations of jupiter. *Icarus*, 65:244.

[Hauser et al., 1984] Hauser, M. G., Silverberg, R. F., Stier, M. T., Kelsall, T., Gezari, D. Y., Dwek, E., Walser, D., Mather, J. C., and Cheung, L. H. (1984). Submillimeter wavelength survey of the galactic plane from $l = -5°$ to $l = +62°$: Structure and energetics of the inner disk. ApJ, 285:74.

[Hinshaw et al., 1996] Hinshaw, G., Banday, A. J., Bennett, C. L., Górski, K. M., Kogut, A., Smoot, G. F., and Wright, E. L. (1996). Band power spectra in the *cobe* dmr 4-year anisotropy maps. ApJ. submitted, preprint `astro-ph/9601058`.

[Hu and White, 1996] Hu, W. and White, M. (1996). Acoustic signatures in the cosmic microwave background. ApJ. submitted, preprint `astro-ph/9602019`.

[Hu, 1995] Hu, W. T. (1995). *Wandering in the Background: A Cosmic Microwave Background Explorer.* PhD thesis, University of California, Berkeley.

[Kamionkowski et al., 1994] Kamionkowski, M., Spergel, D., and Sugiyama, N. (1994). Small-scale cosmic microwave background anisotropies as probe of the geometry of the universe. ApJ, 426:L57.

[Kowitt et al., 1996] Kowitt, M. S. et al. (1996). A detection of bright features in the microwave background. ApJ. in preparation.

[Kuehr et al., 1981] Kuehr et al. (1981). S5 polar cap survey (tbd). AJ, 86:854.

[Martin, 1971] Martin, B. R. (1971). *Statistics for Physicists.* Academic, London.

[Mather, 1982] Mather, J. C. (1982). Bolometer noise: nonequilibrium theory. Appl. Opt., 21:1125.

[Mather, 1984a] Mather, J. C. (1984a). Bolometers: ultimate sensitivity, optimization, and amplifier coupling. Appl. Opt., 23:584.

[Mather, 1984b] Mather, J. C. (1984b). Electrical self-calibration of nonideal bolometers. Appl. Opt., 23:3181.

[Meyer et al., 1991] Meyer, S. S., Cheng, E. S., and Page, L. A. (1991). A measurement of the large-scale cosmic microwave background anisotropy at 1.8 millimeter wavelength. ApJ, 371:L7.

[National Scientific Balloon Facility, 1996] National Scientific Balloon Facility (1996). *NSBF User's Manual.* Available from NSBF, Palestine, TX.

[Netterfield et al., 1996] Netterfield, C. B., Devlin, M. J., Jarosik, N., Page, L., and Wollack, E. J. (1996). A measurement of the angular power spectrum of the anisotropy in the cosmic microwave background. ApJ. submitted, preprint `astro-ph/9601197`.

[Page, 1989] Page, L. A. (1989). *A Measurement of the Cosmic Microwave Background Radiation Anisotropy.* PhD thesis, MIT.

[Page et al., 1994] Page, L. A., Cheng, E. S., Golubovic, B., Gundersen, J., and Meyer, S. S. (1994). Millimeter-submillimeter wavelength filter system. Appl. Opt., 33:11.

[Page et al., 1990] Page, L. A., Cheng, E. S., and Meyer, S. S. (1990). A large-scale cosmic microwave background anisotropy measurement at millimeter and submillimeter wavelengths. ApJ, 355:L1.

[Penzias and Wilson, 1965] Penzias, A. A. and Wilson, R. W. (1965). A measurement of excess antenna temperature at 4080 mc/s. ApJ, 142:419.

[Press et al., 1992] Press, W. H., Teukolsky, S. A., Vetterling, W. T., and Flannery, B. P. (1992). *Numerical Recipes in FORTRAN: The Art of Scientific Computing.* Cambridge University Press, Cambridge, 2nd edition.

[Puchalla, 1995] Puchalla, J. L. (1995). *Measuring Cosmic Microwave Background Radiation Anisotropy on Medium Angular Scales.* PhD thesis, MIT.

[Reich and Reich, 1986] Reich, P. and Reich, W. (1986). A&AS, 63:205.

[Scott et al., 1995] Scott, D., Silk, J., and White, M. (1995). From microwave anisotropies to cosmology. *Science*, 268:829.

[Simonetti et al., 1996] Simonetti, J. H., Dennison, B., and Topasna, G. A. (1996). ApJ, 458:L1.

[Sugiyama, 1995] Sugiyama, N. (1995). Cosmic background anisotropies in cdm cosmology. ApJS, 100:281.

[Turok, 1996] Turok, N. (1996). Private communication.

[Welford and Winston, 1978] Welford, W. T. and Winston, R. (1978). *The Optics of Nonimaging Concentrators.* Academic Press, New York.

[Wheelock et al., 1994] Wheelock, S. L. et al. (1994). *IRAS Sky Survey Atlas Explanatory Supplement.* JPL Publication 94-11. JPL, Pasadena.